UNIVERSITÀ DEGLI STUDI DI ROMA "LA SAPIENZA"

Dottorato di Ricerca in Fisica - XIII ciclo

Analysis of the $\nu_\mu \rightarrow \nu_\tau$ oscillation search in the CHORUS experiment

Alessia Satta

Advisors:

Professor
Ubaldo Dore

Doctor
Roberta Santacesaria

PhD coordinator:

Professor
Guido Martinelli

Contents

Introduction

The neutrinos were introduced in 1932 by W. Pauli to explain the continuous energy spectrum of the electrons emitted in β decay. Since then by means of a large amount of theoretical and experimental work many properties of neutrinos have been determined. They culminated in the neutrino representation inside the Standard Model frame which has been very successful in describing all known neutrino interactions.

Despite of the very positive results many questions remain still unsolved about neutrinos nature. In fact the neutrinos are so weakly interacting particles that it is difficult to obtain measurements with large statistics and high precision. Among all the unsolved question the more fundamental one is whether or not neutrinos are massive particles. The Standard Model was constructed to give massless neutrinos in accordance to the failure of observing experimentally the right-handed neutrinos. Anyhow it is generally believed that, despite of its spectacular success, the Standard Model is incomplete. Many of it generalizations predict massive neutrino. Also the cosmology strengthens the hypothesis of massive neutrinos. In fact the problem of the nature of the dark matter has, as a possible partial solution, neutrinos with mass value of the order of the electronvolt.

An indirect but very sensitive method to search for non-zero neutrino masses is to look at the occurrence of neutrino oscillation, which can happen if neutrinos are massive The essence of neutrino oscillation is very simple. If neutrinos are massive it is possible that the mass eigenstates are different from the weak-eigenstates ν_e, ν_μ, ν_τ, i.e. the neutrino mass matrix in the flavor basis is not diagonal. If this condition is satisfied the weak-eigenstate neutrino produced by the charged-current weak interactions is a linear superposition of different mass eigenstates. During its propagation the different mass states evolve differently so the composition of the initial state in terms of weak states changes with time. This means that the detection of the neutrino through the weak interactions, has non zero probability to reveal a weak state different from the one in which the neutrino has been produced.

In the last 30 years some unexpected experimental observations of the solar and atmospheric neutrinos were interpreted as hints in favor of neutrino oscillation. Moreover in the last few years two collaborations, LSND and SuperKamiokande, claimed evidences of neutrino oscillation but it is fair to say that the problem is still open.

In this context of study of neutrino oscillation the CHORUS experiment is inserted. It has been designed to search for $\nu_\mu \to \nu_\tau$ oscillation with the aim to reach high sensitivity in the mixing angle for large value of Δm^2, the difference of the squared masses. According to the proposal if no oscillation signal is detected it will be possible to exclude at 90% of C.L. the value of $\sin^2 2\theta_{\mu\tau}$ up to $\simeq 2 \cdot 10^{-4}$ for $\Delta m^2 \geq 50 - 100\ eV^2$.

CHORUS is an appearance experiment, it searches for ν_τ neutrinos in the almost pure ν_μ CERN neutrino beam. The ν_τ presence is searched through the charged current reaction ν_τ N $\to$ τ^- X. Thus the ν_τ detection essentially consists in the τ detection. The τ short lifetime has suggested to use an hybrid detector to distinguish the occurrence of ν_τ CC interactions from the much more frequent ν_μ CC or NC interactions: an emulsion target for neutrino interactions and τ decays, plus an electronic detector.

The CHORUS analysis is composed by three steps. In the first the electronic detector is used to select the event more likely to contain a τ in order to reduce the load for the second step, the emulsion scanning, the heaviest one. In the third step the information coming from the electronic detector and the emulsion is combined to reduce the background and to identify the ν_τ candidates.

My PhD thesis is completely devoted to the $\nu_\mu \to \nu_\tau$ analysis. I have simulated all the analysis chain to evaluate its efficiency for the relevant physical channels. A study of the main systematic sources of this efficiency evaluation has been carried on and, whenever it was possible, corrected for. After the efficiency evaluation I worked on the estimation of the background. The background sources in CHORUS are essentially of two types. One comes from the decay of short lived particles as charm hadrons, the other one comes from the hadrons interaction without visible signs of the nucleus recoil or break-up in emulsion. The estimation of the second source required also a simulation of the emulsion response to estimate when nucleus recoil or break-up are visible or not. The small signal CHORUS is searching for imposes to keep very low the background level. Therefore I also studied some background reduction criteria. Combining the efficiency and the background evaluation I have performed with the result of the scanning I could obtain a determination of P$(\nu_\mu \to \nu_\tau)$.

The content of the different chapters is reported in the following:

Chapter 1: a general introduction to the neutrino mass and oscillation from the theoretical and experimental points of view

Chapter 2: a brief description of the CHORUS experimental lay-out

Chapter 3: the CHORUS analysis strategy

Chapter 4: the analysis efficiencies evaluation. Also the main systematic sources are discussed and corrected for

Chapter 5: the background sources evaluation

Chapter 6: the results

Appendix: statistical correction of a mistake done during part of the CHORUS data processing

Chapter 1

Neutrino mass and oscillation

Since Pauli's proposal in 1930 that a neutrino might be one of the final particles in a nuclear beta decay process, a tremendous amount of experimental and theoretical work has been done to understand neutrino nature, properties and interactions. As a result of this work all known neutrino interactions can be derived inside the Standard Model frame. Although this important result there are some fundamental questions still unsolved.

The major question is for sure if neutrinos are massless particles, as assumed in the Standard Model, or massive as predicted by many extensions of the Standard Model. Revealing a non vanishing mass would provide not only a window on physics beyond the Standard Model but it would also have important consequences in cosmology for the fundamental contribution that neutrinos can have in explaining the dark matter.

Possible effects resulting from massive neutrinos are mixing and oscillations, the evidence of which would indirectly but unambiguously proves the massiveness of neutrino. After 30 years from the first hints of oscillations in solar neutrinos flux deficit, a lot of other measurements support and strengthen this possibility: but the question is not definitively settled making oscillations search still a challenging subject for particle physicists. CHORUS is one of the experiments trying to obtain unambiguous evidence for ν oscillations.

The aim of this chapter is to give a brief introduction to neutrino mass and oscillations from the theoretical and the experimental point of view. A complete description of this phenomena can be found in [1, 2, 3, 4].

This chapter is organized as follows:

- Standard Model description of neutrino interactions and fermion mass generation
- Neutrino mass generation in Standard Model extensions
- Consequences of a massive neutrino: oscillations and mixing

- Experimental situation in oscillations searches
- The CHORUS experiment in oscillations search context

1.1 Neutrino in the standard model

1.1.1 Introduction to the standard model

The standard model describes all electroweak interactions. It is a renormalizable gauge theory based on $SU(2)_L \times U(1)_Y$ local symmetry group. Imposing the invariance of the Lagrangian on a gauge transformation the interactions between gauge fields and matter are derived. The three gauge bosons of $SU(2)_L$ are denoted by $W^{\pm}$ and W^0, whereas the $U(1)_Y$ gauge boson is denoted by B^0. The 12 matter fields, six quarks and six leptons, are grouped in three families: (u,d',e,ν_e), (c,s',μ,ν_μ), (t,b',τ,ν_τ). The left handed components of each family are grouped in two weak isospin doublets whereas the right handed are singlets. For example for the first family

$$\begin{pmatrix} \nu_e \\ e^- \end{pmatrix}_L \quad \begin{pmatrix} u \\ d' \end{pmatrix}_L \quad u_R \quad d'_R \quad e_R$$

The prime on quarks implies that they are not mass eigenstates but linear combinations of them: i.e.

$$\begin{pmatrix} d' \\ s' \\ b' \end{pmatrix} = V \begin{pmatrix} d \\ s \\ b \end{pmatrix} \tag{1.1}$$

where V is a 3x3 complex matrix known as the Cabibbo-Kobayashi-Maskawa matrix.

Through the so-called Higgs mechanism, a non vanishing vacuum expectation value of the Higgs field, the gauge symmetry is spontaneously broken down to $U(1)_{em}$. This mechanism gives mass to the charged gauge bosons $W^{\pm}$; in the neutral gauge boson sector the combination $Z = cos\theta_W W^0 + sin\theta_W B$, where θ_W is the Weinberg angle, acquires a mass. The combination orthogonal to Z, the photon field A, remains massless corresponding to the unbroken $U(1)_{em}$ symmetry.

After the symmetry breaking the interaction terms between the gauge bosons and the matter fields can be written as

$$\mathcal{L}_I = \frac{g}{\sqrt{2}}(J^\mu W_\mu^+ + J^{\mu +} W_\mu^-) + \frac{g}{\sqrt{cos\theta_W}} K^\mu Z_\mu + e\sum_f \overline{f}\gamma^\mu Q f A_\mu \tag{1.2}$$

where for the first family, and similarly for the other two,

$$\mathrm{J}^\mu = \overline{u}\gamma^\mu \frac{(1-\gamma^5)}{2} d' + \overline{\nu_e}\gamma^\mu u \frac{(1-\gamma^5)}{2} e \tag{1.3}$$

The neutral current K^μ is given by

$$\mathrm{K}^\mu = \sum_f \overline{f}\gamma^\mu (I_{3L}\frac{(1-\gamma^5)}{2} - sin^2\theta_W Q) f \tag{1.4}$$

where f runs over all the fermionic fields, Q is the electric charge and I_{3L} is the value of the neutral generator of $SU(2)_L$ for the left components of fermion fields (tab 1.1). In particular for neutrino, since it is electrically neutral, only two basic

	I	I_{3L}	Q
$\begin{pmatrix} \nu_e \\ e^- \end{pmatrix}_L$	1/2	$1/2$ $-1/2$	0 -1
$\begin{pmatrix} u \\ d' \end{pmatrix}_L$	1/2	$1/2$ $-1/2$	$2/3$ $-1/3$
e_R^-	0	0	-1
u_R	0	0	2/3
d'_R	0	0	-1/3

Table 1.1: Generators eigenvalues for the first family

interactions survive: charged and neutral weak current interactions (figure 1.1).

1.1.2 Dirac fermions masses generation

As the gauge bosons masses also the fermions masses arise from the non vanishing of the vacuum expectation value of the Higgs boson. In fact the gauge invariance prevents adding fermions bare masses in the Lagrangian. They arise from the following Yukawa interaction allowed by the gauge symmetry:

$$\mathcal{L}_Y = -G_e(\overline{\nu}_e, \overline{e})_L \phi e_R - G_u(\overline{u}, \overline{d})_L \phi u_R - G_d(\overline{u}, \overline{d})_L \phi^+ d_R + h.c. \tag{1.5}$$

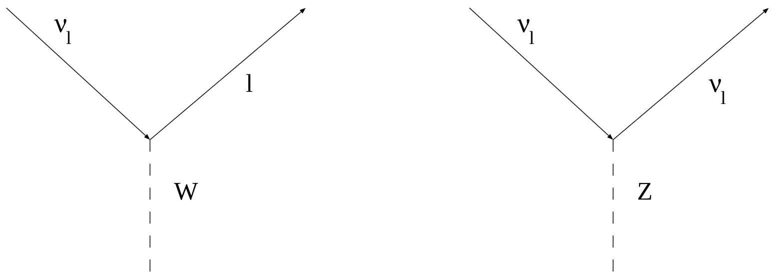

Figure 1.1: Basic Feynman diagrams that describe neutrino interactions. **Right** charged current interaction. **Left** neutral current.

where ϕ indicates the Higgs doublets. After the symmetry breaking

$$\phi(x) \to \frac{1}{\sqrt{2}} \begin{pmatrix} 0 \\ v + h(x) \end{pmatrix} \tag{1.6}$$

and omitting the terms proportional to h(x)

$$L_Y = -\frac{G_e}{\sqrt{2}} v(\overline{e}_L e_R + \overline{e}_R e_L) - \frac{G_u}{\sqrt{2}} v(\overline{u}_L u_R + \overline{u}_R u_L) - \frac{G_d}{\sqrt{2}} v(\overline{d}_L d_R + \overline{d}_R d_L) \tag{1.7}$$

Renaming

$$\frac{G_i}{\sqrt{2}} v = m_i \tag{1.8}$$

$$e = e_R + e_L \quad u = u_R + u_L \quad d = d_R + d_L \tag{1.9}$$

finally we obtain

$$\mathcal{L}_Y = -m_e(\overline{e}e) - m_u(\overline{u}u) - m_d(\overline{d}d) \tag{1.10}$$

which is the standard mass term for Dirac particles. No Dirac mass arises from Higgs mechanism for neutrino, as for charged fermion fields, since in the standard model the ν_R field is absent.

1.1.3 Majorana neutrinos and mass term

In the standard model no mass can be generated if neutrinos are, as all other fermions, Dirac particles. Before concluding that it is impossible to have massive neutrinos in the standard model we have to explore the possibility that neutrinos are Majorana particles.

To understand what are Majorana particles let's start considering an electron field. To describe the electron field we need four degrees of freedom: two helicity states for electron $\mathrm{e_R}$, $\mathrm{e_L}$ and two for its antiparticle the positron $\mathrm{\hat{e}_R}$ $\mathrm{\hat{e}_L}$. To comprehend it let's assume to have an electron in the z-direction, with z-spin component equal to -1/2. Momentum and spin are antiparallel so we have a left-handed electron (also known as negative chirality electron) $\mathrm{e_L}$. Let's suppose now that the same particle is observed by an other reference frame moving in z direction faster than the electron. In this reference the electron momentum appears as negative and the helicity results positive. We have two possible positive helicity states $\mathrm{e_R}$, $\mathrm{\hat{e}_R}$. We are sure that the second observer will see the $\mathrm{e_R}$ and not $\mathrm{\hat{e}_R}$ state since the electric charge is a Lorentz invariant: by boosting to a different Lorentz frame one cannot see a different charge on a particle. Thus to have a Lorentz invariant description of the electron field we need $\mathrm{e_R}$, $\mathrm{e_L}$ and $\mathrm{\hat{e}_R}$ $\mathrm{\hat{e}_L}$ for the positron: four degrees of freedom in total.

If we repeat the same argument for neutrino the counting of degrees of freedom is not so obvious. In fact in the standard model the neutrino is massless so only two states are needed, $\nu_\mathrm{L}, \hat{\nu}_\mathrm{R}$. What happens for massive neutrinos? Suppose that an observer sees a ν_L. If neutrino is massive then a reference frame moving faster than the neutrino exists, in this frame, as for the electron case, a positive helicity state is observed. If we assume, analogously to the electron case, that this state is ν_R, we are forced to introduce ν_R and $\hat{\nu}_\mathrm{L}$ states in the standard model to ensure Lorentz invariance. The neutrino will be, as all other fermions, a Dirac particle with four degrees of freedom. The question is *could the positive helicity state be something different from ν_R, something for which we do not have to modify the standard model content?*. Remember that we have a positive helicity particle in the standard model, the $\hat{\nu}_\mathrm{R}$. Could the boosted observer see this state or are we sure that it is ν_R? Unlike the electron case, the ν_L and $\hat{\nu}_\mathrm{R}$ have the same electric charge (i.e. zero) so nothing goes wrong here in assuming that the boosted counterpart of ν_L is $\hat{\nu}_\mathrm{R}$. The only quantum number defined in the context of standard model which is different for $\hat{\nu}_\mathrm{R}$ and ν_L is the lepton number. But unlikely the electromagnetic U(1) symmetry, that governs the dynamics, the lepton symmetry is global and accidental in the standard model, so there is nothing "sacred" about lepton number conservation: it could be broken. If the lepton number is not conserved, it is not a good quantum number then there is no reason why ν_L and $\hat{\nu}_\mathrm{R}$ cannot be the boosted counterparts of one another: essentially there is not any conserved quantum number that distinguishes the particle and the antiparticle state or, in other words, the particle is identical to the antiparticle. In this case to have a Lorentz invariant description of the neutrino field we only need two degrees of freedom. This kind of massive fermion field with only two states is known as a Majorana field. Let's note that, since the neutrino is the only electrical neutral fermion field, it is the only one that can be a Majorana particle.

Before describing the Majorana mass terms let's introduce some useful notations. Obviously massive fermion fields have both chiral states to ensure Lorentz invariance. Now there are essentially two possibilities. First the right handed components of a massive field can be completely independent of the left handed one, in this case we have a Dirac field.

$$\psi = \psi_L + \psi_R \tag{1.11}$$

Second, the right handed field can be just a $\tilde{\mathrm{C}}$-conjugate of the left-handed one, in this case we have a Majorana field. The action of $\tilde{\mathrm{C}}$, the particle-antiparticle conjugation operator, on a fermion field ψ is defined through

$$\tilde{\mathrm{C}} : \psi \to \psi^c = C\overline{\psi}^T \tag{1.12}$$

C is a matrix that acts on the spinor indices. When $\tilde{\mathrm{C}}$ acts on chiral field it flips its chirality

$$\tilde{\mathrm{C}} : \psi_L \to (\psi_L)^c = (\psi^c)_R \ ; \qquad \psi_R \to (\psi_R)^c = (\psi^c)_L \tag{1.13}$$

i.e. the antiparticle of a left handed fermion field is right handed. With this definition of $\tilde{\mathrm{C}}$ the Majorana field can be written as

$$\psi = \psi_L + (\psi_L)^c \text{ or } \quad \psi = \psi_R + (\psi_R)^c \tag{1.14}$$

From this definition immediately comes

$$(\psi)^c = \psi \tag{1.15}$$

therefore a Majorana field is an eigenstate of $\tilde{\mathrm{C}}$ operator, another way to say that Majorana neutrinos coincide with their antiparticles.

For a massive fermion, Dirac or Majorana, field the mass term in the Lagrangian has the form

$$-\mathcal{L}_m = m\overline{\psi}\psi = m\overline{(\psi_L + \psi_R)}(\psi_L + \psi_R) = m(\overline{\psi}_L\psi_R + \overline{\psi}_R\psi_L) \tag{1.16}$$

In the Majorana case using eq. 1.14 and the relation $\overline{\psi}^c = \psi^T C$ the mass term can be written in a simplified form

$$-\mathcal{L}_m = \frac{1}{2}[\psi_L^T C m \psi_L + h.c.] \tag{1.17}$$

Kinematically Dirac and Majorana mass terms are indistinguishable: they lead to the same relation between energy, momentum and mass of a particle, $E = \sqrt{P^2 + m^2}$. Instead they are different with respect to global U(1) group transformation

$$\psi \to e^{i\alpha}\psi \qquad \overline{\psi} \to e^{-i\alpha}\overline{\psi} \tag{1.18}$$

in fact the Dirac mass term is invariant, thus electric charge, lepton and baryon number are exactly conserved, while the Majorana mass term breaks all the charge of the field ψ by two units. So if neutrinos are Majorana massive particles the total lepton number is not conserved, while it is conserved if they are Dirac particles.

We will now explore the possibility to have a Majorana mass term in the standard model. Since $\psi_L^T C M \psi_L$ is a component of a triplet of weak isospin, in order to introduce the Majorana mass in a gauge invariant way so to not spoil the renormalizability of the theory, we should write a term as $\phi^+\phi \times \psi_L^T C M \psi_L$. This term has dimension equal to five so it cannot enter in a Lagrangian at the fundamental level without breaking the renormalizability of the standard model. A similar term cannot also appear at some higher loop level since it violates the leptonic number and this is in contradiction with the exact conservation of B-L number in the standard model[1]. Concluding no Majorana mass term can appear in the standard model, since also no Dirac term can be generated we must conclude that neutrinos are massless in this model.

[1]In fact in the standard model L and B are exactly conserved at perturbative level due to accidental symmetries of the Lagrangian. These symmetries are called accidental because they are not imposed on the Lagrangian but just a consequences of the particle content of the standard model, its gauge invariance, renormalizability and Lorentz invariance. In fact one can consider all possible L- and B- violating operators that can be constructed with the standard model fields and make sure that all of them either violate gauge or Lorentz invariance, or are not renormalizable. Nonperturbatively, both L and B are violated since these symmetries are anomalous. But the triangle anomalies of the baryon and lepton number current are equal to each other in the standard model, so that B-L is anomaly free and exactly conserved.

1.2 Neutrino mass generation in standard model extensions

1.2.1 Upper limit on neutrinos masses

Firstly let's recall the values and the techniques used to obtained the neutrinos masses upper limits values.

Electron neutrino mass The present best upper limit on ν_e mass has been determined studying the β decays. The most useful quantity is

$$K(E) = \sqrt{\frac{d\Gamma/dE}{pEF(Z,E)}} \sim [(E_0 - E)\sqrt{(E_0 - E) - m_\nu^2}]^{1/2} \tag{1.19}$$

where $d\Gamma/dE$ is the differential decay rate, E is the total electron energy, p is its momentum, F(Z,E), known as the Coulomb function, is calculable with good approximation and E_0 is the total energy released equal to $M_i - M_f - m_\nu$. The plot of the K(E) function is called the Kurie plot. For $\mathrm{m}_{\nu_e} = 0$ the Kurie plot becomes a straight line proportional to $E_o - E$, intercepting the energy axis at $E = E_0$. If $\mathrm{m}_{\nu_e} \neq 0$ the spectrum shape near the end point will curve. This deviation is most sensitive to m_ν when the value of E_0 is small. Among all known β-decay, the process $^3H \rightarrow\ ^4He\ e^- \overline{\nu}_e$ has the smallest E_0 value, so this β-decay is widely used to search for ν_e mass: such experiments give the upper limit of 3 eV/c^2 [5].

Muon neutrino mass The best upper limit on ν_μ mass value is achieved studying the decay $\pi \rightarrow \mu\overline{\nu}_\mu$. The experiment is designed to stop the pions in a target to let them decay at rest. Energy-momentum conservation leads to

$$\mathrm{m}_\nu^2 = m_\pi^2 + m_\mu^2 - 2m_\pi\sqrt{p^2 + m_\mu^2} \tag{1.20}$$

therefore an accurate measurement of muon momentum together with precise value of m_π and m_μ yields the value of m_ν. The upper limit using this technique is 190 KeV/c^2 [5]. Because of the experimental complexities and uncertainties in the value of m_π and m_μ it is fair to say that it will be hard to significantly improve the upper limit.

Tau neutrino mass First experimental evidence of the tau neutrino existence is very recent [6], thus its properties have not been still tested directly. Anyhow it was assumed, as predicted by the standard model, to exist and to be one of the particles produced in the τ decay. This assumption has permitted to try to measure ν_τ mass studying the τ decay even before the evidence of ν_τ existence.

The very heavy τ mass allows such a large phase space as to make the determination of m_{ν_τ} hopelessly difficult. In order to reduce the available phase space for ν_τ the $\tau \to 5\pi$ decay has been studied. Using the τ of fixed momentum produced in electron-positron collider and measuring all the charged pions momenta, an upper limit of 18.2 MeV/c^2 has been obtained [5].

1.2.2 Why massive neutrinos ?

The standard model predicts massless neutrinos as we have seen in the previous section and in the meantime it has so far been very successful in explaining and predicting all the various weak processes involving neutrinos. So why are we interested in considering neutrinos masses, thus going beyond the standard model?

Indeed there are a lot of motivations to open up a discussion on massive neutrinos. First of course the upper bounds are not so tight to appear natural assuming that all neutrinos are massless. For instance the ν_μ can be about half as heavy as the electron and the ν_τ can be even 40 times heavier than electron. This lack of convincing experimental evidence of massless neutrinos is by itself a good reason to try to pin down the neutrino mass values with better accuracy, but there are other motivations that, supporting the hypothesis of massive neutrinos, render neutrinos mass searches more appealing. There are essentially two kinds of motivations: theoretical and cosmological.

Theoretical motivations for massive neutrinos

We have seen at the end of section 1.1.1 that neutrinos are massless in the standard model just because the model doesn't contain the ν_R field. Otherwise this field could pair with ν_L and through the Higgs mechanism produce a neutrino Dirac mass term. But there is no fundamental reason to not include ν_R and to have massive neutrinos. Just to give an idea why the masslessness of neutrinos is not fundamental, let's compare neutrinos with photon. Both are predicted massless but the masslessness of photon derives from conserved gauge symmetry which governs the dynamics of electromagnetic interactions. For the masslessness of neutrinos we see no such symmetry principle so it is unsatisfactory from a theoretical point of view.

Of course it is possible to modify slightly the field content of the standard model and to obtain a massive neutrino but also this is unsatisfactory. In fact giving neutrino mass through the Higgs mechanism doesn't explain the reason why the mass values are so small compared with the charged fermions masses. It would be just an accident, just because the Yukawa coupling constants for neutrinos are smaller than for the other fermions. Of course also the mass values for the charged fermions are arbitrary, but within each generation the mass spread is not large, less than two order of magnitude (tab. 1.2). If we include also neutrino, since their masses are supposed by cosmological arguments to be not larger than $\sim$ eV, we will end up with a spread of masses of at least five order for the first family and eight for the third. Instead of this enormous spread of Yukawa coupling constants, more appealing explanation for light neutrinos masses comes from most standard model extensions. In these models neutrinos are so light just because they are the only neutral fermions and they can be Majorana particle, thus they can have a different mass generation mechanism.

u $\sim$ 5 MeV	c $\sim$ 1 GeV	t $\sim$ 175 GeV
d $\sim$ 8 MeV	s $\sim$ 0.1 GeV	b $\sim$ 5 GeV
e $\sim$ 0.5 MeV	$\mu \sim$ 0.1 GeV	$\tau \sim$ 2 GeV

Table 1.2: Mass values for charged fermions of each generation

Summarizing the masslessness of neutrinos seems, from theoretical point of view, not well motivated and it appears natural to look beyond the standard model for a theory that explains in the meantime how neutrino masses are generated and why they are so small.

Cosmological motivation for massive neutrinos

During the last years due to the rapid improvement in astrophysics measurements on dark matter, density distribution and structures formation at different scales, the cosmological suggestion of neutrinos masses was moved from large towards small values, nevertheless the cosmological motivation remains a strong one [7, 8].

The cosmological suggestion for massive neutrinos depends on the dark matter existence. In fact although our knowledge of the mass and energy content of the universe is not poor any longer, we can confidently say that most of the matter in the universe is of unknown form and dark. Stars and closely related material (Ω_{lum}) contribute to a tiny fraction of the critical density (the energy-matter density predicted by the inflation model, denoted by Ω_0). In fact Ω_{lum}/Ω_0 is measured to be $\simeq 0.004$, while the amount of matter known to be present from its gravitational effects (Ω_M) contributes around hundred times this amount.

All the variety of methods used for determining the amount of matter converge on $\Omega_M/\Omega_0 \sim 1/3$. They include measurements of galaxies clusters masses and the peculiar motion of galaxies. The average of all measurements gives

$\Omega_M/\Omega_0 = (0.35 \pm 0.07)$. The theory of big-bang nucleosynthesis and the recent measured primeval abundance of deuterium pin down the baryon density very precisely, $\Omega_B/\Omega_0 \simeq 0.05$. The discrepancy between this value and the dynamical measurements of the matter density is an evidence for non baryonic dark matter. At least three different candidates have been suggested: axions, WIMP and neutrinos.

The neutrinos density is very large ($\simeq 100\ cm^{-3}$) so they could be an important component of mass density even if only one species has a tiny mass. The ratio of matter due to neutrinos with respect to the baryonic component is

$$\Omega_\nu/\Omega_B \simeq \sum_i (m_{\nu_i}/2eV) \tag{1.21}$$

Since the neutrinos were relativistic when, during the first phases after the Big Bang, they went out of thermal equilibrium, they contribute to the hot part of the dark matter. The hot component of the dark matter should be not too large otherwise it would have washed out the small density fluctuations from which the present structure (stars and galaxies) originated for gravitational attraction. In the mean time the presence of hot dark matter is important to fit the small scale universe structure: it solves the main problem of cold dark matter only model, namely production of much more structures on small scales than observed. The estimated hot dark matter contribution to Ω_0 that fits the observed structures on all scales is $\simeq \Omega_B$. Assuming the main contribution to the hot dark matter coming from neutrinos, we expect neutrinos masses, dependent on the degeneracy in mass of neutrinos, to be of the order of $\simeq$ eV.

1.2.3 Mass generation: see-saw mechanism

Since there are good reasons in favor of massive neutrinos it is worth to describe and analyse which is the general neutrinos mass term predicted by most standard model extensions.

There are two minimal modifications of the field content of the standard model that can lead to massive neutrinos. First it is possible to add a Higgs triplet, Δ, to the usual doublet to get a term of the form ${\nu_{\rm L}}^T C M \nu_{\rm L} \Delta$. The non-vanishing vacuum expectation value of Δ gives a Majorana mass and breaks L-conservation. The spontaneously breaking of L introduces in the theory a massless Goldstone boson J, the Majoron. The existence of a Majoron is excluded by experimental results, in fact its massive counterpart, ρ, should be very light and could be produced in the decay Z $\rightarrow J\rho$. This decay would add to the invisible Z width a contribution equals to extra two neutrinos species, in contradictions to the LEP observation of only three neutrinos species.

Another possible modification is to assume the existence of ν_{R}: it would lead to Dirac mass term from the usual Higgs mechanism. Once we have introduced ν_{R}, since it is a singlet of the $\mathrm{SU}(2)_L \times U(1)_Y$ gauge group, nothing prevents from adding the Majorana term ${\nu_{\mathrm{R}}}^T CM\nu_{\mathrm{R}}$ without violating the renormalizability of the theory. Thus L number violation is naturally induced by the presence of ν_{R} unless we enforce it by hand. So if we try to extend the standard model in order to have massive neutrinos it is quite natural to search for a theory that predicts Lepton number violation and ν_{R} fields. GUT's are good candidates since L and B violations are their general properties and the all GUT groups larger than $SU(5)$ require the existence of ν_{R}[2]. Moreover they offer a natural explanation for the smallness of neutrinos masses that turns out to be inversely proportional to the large scale where lepton number is violated: the see-saw mechanism.

The see-saw mechanism in its simplest form arises as follows. Suppose that we have only one neutrino species. The mass term in the Lagrangian can be written as

$$-\mathcal{L} = m_D \overline{\nu}_R \nu_L + \frac{1}{2} m_R {\nu_{\mathrm{R}}}^T C \nu_{\mathrm{R}} + h.c. \tag{1.22}$$

Introducing $n_L = (\nu_{\mathrm{L}}, (\nu_{\mathrm{R}})^c)$, vector of 2 left handed fields, and using the relations

$$({\nu_{\mathrm{R}}}^T C m^* \nu_{\mathrm{R}})^+ = (\nu^c)_L^T C m (\nu^c)_L, \qquad \overline{\nu}_R m \nu_{\mathrm{L}} = (\nu^c)_l^T C m \nu_{\mathrm{L}} = \nu_L^T C m (\nu^c)_L \tag{1.23}$$

the 1.22 can be simplified as

$$-\mathcal{L} = \frac{1}{2} n_L^T C \mathcal{M} n_L + h.c. \tag{1.24}$$

where $\mathcal{M}$ has the form

$$\mathcal{M} = \begin{pmatrix} 0 & m_D \\ m_D & m_R \end{pmatrix} \tag{1.25}$$

The matrix $\mathcal{M}$ can be diagonalized by the transformation $U^T \mathcal{M} U = \mathcal{M}_d$ where U is an orthogonal matrix. The left handed components of neutrino mass eigenstates χ_L are

$$n_L = \begin{pmatrix} \nu_{\mathrm{L}} \\ (\nu_R)^c \end{pmatrix} = U\chi_L = \begin{pmatrix} cos\theta & sin\theta \\ -sin\theta & cos\theta \end{pmatrix} \cdot \begin{pmatrix} \chi_{1L} \\ \chi_{2L} \end{pmatrix} \tag{1.26}$$

[2]Actually also if ν_{R} is non present, the GUT L-violation can lead to massive neutrinos through the term $\frac{\lambda}{M} {\nu_{\mathrm{L}}}^T C \nu_{\mathrm{L}} \phi^+ \phi$ where M is a large scale mass of the order of $\mathrm{M_{GUT}}$

while the mass eigenvalues are

$$m_{1,2} = \frac{m_R}{2} \pm \sqrt{\left(\frac{m_R}{2}\right)^2 + m_D^2} \tag{1.27}$$

and the mixing angle θ is given by

$$\tan 2\theta = \frac{2m_D}{m_R}. \tag{1.28}$$

Defining

$$\chi_1 = \chi_{1L} + (\chi_{1L})^c \qquad \chi_2 = \chi_{2L} - (\chi_{2L})^c \tag{1.29}$$

the mass term can now be rewritten as

$$-\mathcal{L} = \frac{1}{2}(m_1\overline{\chi}_1\chi_1 + m_2\overline{\chi}_2\chi_2) \tag{1.30}$$

It follows immediately from 1.29 and 1.30 that the mass eigenstates χ_1 and χ_2 are Majorana neutrinos. This is not surprising, in fact we have four neutrino degrees of freedom, ν_{L} ν_{R} and their $\tilde{\mathrm{C}}$-conjugates, and two different mass eigenvalues, so two degrees of freedom for eigenstate which therefore has to be Majorana particle.

The right-handed neutrino ν_{R} is an electroweak singlet so its mass is not protected by the electroweak symmetry. In absence of a protective symmetry we expect that ν_{R} mass is of the order of the cut-off of the low energy theory which, in the assumption that the Standard model extension is an effective theory valid up to GUT energy, is identified with $\mathrm{M_{GUT}}$. So it is natural to consider the case of $m_D << m_R$. In this limit we have

$$\begin{gathered}\theta \simeq \frac{m_D}{m_R} << 1, \qquad m_1 \simeq -\frac{m_D^2}{m_R} \qquad m_2 \simeq m_R \\ \chi_1 \simeq \nu_{\mathrm{L}} + (\nu_{\mathrm{L}})^c \quad \chi_2 \simeq \nu_{\mathrm{R}} + (\nu_{\mathrm{L}})^c.\end{gathered} \tag{1.31}$$

Thus we have a very light Majorana mass eigenstate χ_1 predominantly composed of ν_{L} and a heavy eigenstate χ_2 mainly composed of ν_{R}: it is the ν_{R} being heavy that makes ν_{L} very light. This is the see-saw mechanism.

The extension of this mechanism to the general case of n generation families is straight-forward. In fact n_L becomes a $2 \times n$ left-handed field vector, m_D and m_R two complex $n \times n$ matrices. Through a unitary matrix U it is possible to block-diagonalize $\mathcal{M}$ so to decouple light and heavy neutrinos.

$$U^T\mathcal{M}U = U^T \begin{pmatrix} 0 & m_D \\ m_D^T & m_R \end{pmatrix} U = \begin{pmatrix} \hat{M}_l & 0 \\ 0 & \hat{M}_R \end{pmatrix} \tag{1.32}$$

where

$$\hat{M}_L \simeq m_D m_R^{-1} m_D^T \quad \text{and} \qquad \hat{M}_R \simeq m_R \tag{1.33}$$

The diagonalization of the effective mass matrix $\hat{M}_L$ yields n light Majorana neutrinos which are predominantly composed of the usual ("active") neutrinos $\nu_{\rm L}$ with a small admixture of "sterile" neutrinos $\nu_{\rm R}$, while the diagonalization of $\hat{M}_R$ gives n heavy Majorana neutrinos which are mainly composed by $\nu_{\rm R}$.

Since m_D is generated by the same mechanism of the other charged fermions masses we are led to the natural hypothesis that it is related to the quarks or leptons mass values. If we accept that m_D for each generation is $\propto m_{f_i}$ (where m_{f_i} is the up quark mass or the charged lepton mass for the i-generation) and the m_R is independent of generation index, we have for active neutrinos masses the quadratic see-saw prediction

$$m_1 : m_2 : m_3 = m_u^2 : m_c^2 : m_t^2 \quad \text{or} \qquad m_1 : m_2 : m_3 = m_e^2 : m_\mu^2 : m_\tau^2. \tag{1.34}$$

If m_R turns out to have a hierarchy similar to the charged fermion that leads to the linear see-saw prediction

$$m_1 : m_2 : m_3 = m_u : m_c : m_t \quad \text{or} \qquad m_1 : m_2 : m_3 = m_e : m_\mu : m_\tau. \tag{1.35}$$

1.3 Consequences of massive neutrinos: oscillation

In case of massive neutrinos some processes, which are otherwise forbidden, happen. For instance massive neutrinos would have electromagnetic properties as magnetic moment or electric dipole different from zero. An impressive phenomena that would happen in case of massive Majorana neutrinos is the neutrinoless double β decay. This process consists essentially in a conversion of two neutrons in a nucleus in two protons with the emission of two electrons (fig 1.2). It violates the lepton number so it requires Majorana neutrinos but it also needs that the left-handed component couples to the right-handed one leading to the request of a massive neutrino.

There are others impressive processes that happen if neutrinos, apart from being massive, are also mixed. By mixed we intend that the rotation matrix between flavor and mass states is not trivially a diagonal matrix. In this case for instance both the radiative decay of a neutrino in a lighter one, $\nu_\alpha \to \nu_\beta \gamma$, and the radiative decay of muon, $\mu \to$ eγ are possible. However most studied and

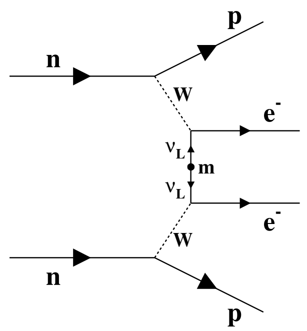

Figure 1.2: Basic Feynman diagram that describes neutrinoless double β-decay

searched effect of mixed massive neutrinos is neutrino oscillation: in fact it is a very sensitive method to search for small neutrinos masses.

The essence of neutrino oscillation is very simple. Neutrinos are produced by the charged-current weak interactions and therefore are weak-eigenstate neutrinos ν_e, ν_μ, ν_τ. However, since the neutrinos masses matrix in the flavor basis is not diagonal, the produced neutrino is a linear superposition of different mass eigenstates. During neutrino propagation the different mass states evolve differently so the composition of the initial state in terms of weak states changes with time. As time goes by the detection of neutrino, carried out by weak interaction, has non zero probability to reveal a weak state different from the one in which the neutrino has been produced.

1.3.1 Vacuum oscillation

Let's now obtain the oscillation formulas in the case neutrino propagates in vacuum. Consider a neutrino beam of flavour α created at time t=0 in a charged current interaction. In general it is not a physical particle, but rather a superposition of physical fields ν_k with different masses $\mathrm{m_k}$[3]

$$|\nu_\alpha\rangle = \sum_{k=1}^{n} U^*_{\alpha k} |\nu_\mathrm{k}\rangle \tag{1.36}$$

Let's make two approximations:

- the initial neutrino is described by a plane wave with well defined energy and momentum
- neutrinos are assumed to be relativistic, i.e. $|p| >> m$, so that

$$E = \sqrt{|p|^2 + m^2} \simeq p + \frac{m^2}{2p}$$

According to the Schrödinger equation the mass eigenstate $|\nu_\mathrm{k}\rangle$ evolves in time with the phase factor $exp(-iE_k t)$ and, at time t, we get

$$|\nu_\alpha(t)\rangle = \sum_{k=1}^{n} U^*_{\alpha k} \mathrm{e}^{-\mathrm{iE_k t}} |\nu_\mathrm{k}\rangle$$

If the masses values are different $|\nu_\alpha(t)\rangle$ represents a different superposition of the physical eigenstates with respect to the initial one. In general this state has not only the property of α but also of other flavours. For instance the amplitude to find ν_β at the time t is given by

$$\langle \nu_\beta | \nu_\alpha(t)\rangle = \sum_{k=1}^{n} U_{\beta k} \mathrm{e}^{-\mathrm{iE_k t}} U^*_{\alpha k}$$

consequently the probability of this transition is

$$P_{\nu_\alpha \to \nu_\beta}(t) = |\langle \nu_\beta | \nu_\alpha(t)\rangle|^2 = \left| \sum_{k=1}^{n} U_{\beta k} \mathrm{e}^{-\mathrm{iE_k t}} U^*_{\alpha k} \right|^2 \tag{1.37}$$

Using the unitary relation

$$\sum_{k=1}^{n} U_{\beta k} U^*_{\alpha k} = \delta_{\alpha\beta}$$

[3]In the following we assume that we have n light mass neutrinos with $m_1 << m_2 << ... << m_n$ active or sterile. If there are also neutrinos so heavy that they are not produced in the standard weak process, we neglect them (This for instance occurs in the see-saw model described in). In this case strictly speaking the mixing matrix is not unitary, since it is only a submatrix of a unitary matrix, but it is unitary to a good approximation.

the probability 1.37 can be written as

$$P_{\nu_\alpha \to \nu_\beta}(t) = \left| \delta_{\alpha\beta} + \sum_{k=2}^{n} U_{\beta k} U^*_{\alpha k} \left[exp\left(-i\frac{\Delta m_{k1} L}{2E} \right) - 1 \right] \right|^2 \tag{1.38}$$

where $\Delta m_{k1} \equiv m_k^2 - m_1^2$, and $L = ct$ is the distance between the production and the detection points. Hence the probability of $\nu_\alpha \to \nu_\beta$ transition depends on the elements of the mixing matrix, on $n-1$ mass-squared and on the parameter L/E which is fixed by the experimental setup.

Two neutrino oscillation and exclusion plot

Let's now derive the oscillation formula in the particular case when only two neutrino types are involved in oscillation because this is the usual assumption under which the results of oscillation experiments are analysed. The U matrix in this case is given by

$$U = U^* = \begin{pmatrix} \cos\theta & \sin\theta \\ -\sin\theta & \cos\theta \end{pmatrix}$$

and the 1.38 becomes

$$P_{\nu_\alpha \to \nu_\beta}(t) = \sin^2 2\theta \sin^2 \left(1.267 \frac{\Delta m^2 (eV^2) L(Km)}{E(GeV)} \right) \tag{1.39}$$

thus the transition probability is a periodic function of L/E. The amplitude of the oscillation is $\sin^2 2\theta$ while the oscillation length is

$$L_{osc} = \frac{\pi E}{1.267 \Delta m^2} \tag{1.40}$$

Figure 1.3 shows the behavior of the oscillation probability with $\sin^2 2\theta = 1$. It is clear that neutrino oscillation can be observed only if the condition $L_{osc} \lesssim L$ is satisfied, the maximum sensitivity is for $L = L_{osc}$: therefore in a particular experimental set-up, where E and L are roughly fixed, the Δm^2 maximum sensitivity is reached for $\Delta m^2 \simeq E/L$. Thus the larger the value of the parameter L/E, the smaller are the values of Δm^2 investigated; the estimate of Δm^2 that can be probed by a series of typical neutrino oscillation experiments are presented in tab 1.3. With the help of the figure 1.3 it is also easy to understand qualitatively the general features of the exclusion plots in the plane $\Delta m^2, \sin^2 2\theta$ presented by experiments that didn't get indication in favour of neutrino oscillation. Since all neutrino beams have a particular energy spectrum and the neutrino source and the

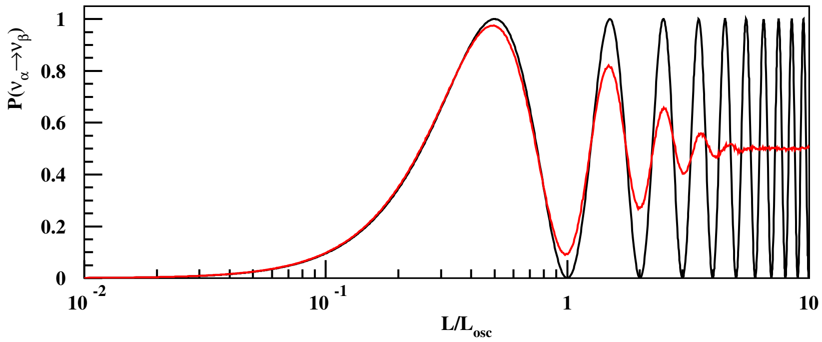

Figure 1.3: Oscillation probability for $\sin^2 2\theta = 1$ as a function of L/L_{osc}. The red line represents the same probability averaged over a neutrino energy of guassian behavior with $\sigma = E/10$.

Experiment	L(m)	E(MeV)	$\Delta m^2 (eV^2)$
Reactor SBL	10^2	1	10^{-2}
Reactor LBL	10^3	1	10^{-3}
Accelerator SBL	10^3	10^3	1
Accelerator LBL	10^6	10^3	10^{-3}
Atmospheric	10^7	10^3	10^{-4}
Solar	10^{11}	1	10^{-11}

Table 1.3: Order of magnitude estimates of the values of Δm^2 which can be probed by the different types of experiment: reactor short-baseline (SBL), reactor long-baseline (LBL), accelerator SBL, accelerator LBL atmospheric and solar.

detector are extended in space what is measured experimentally is an upper limit of the probability averaged over E and L. The behavior of this averaged quantity is reported (the red line) in the figure: for large Δm^2 the oscillation probability is independent from Δm^2 giving the usual vertical-line part of the exclusion curve (fig 1.4). The minimal value for the $\sin^2 2\theta$ is obtained at the first maximum of

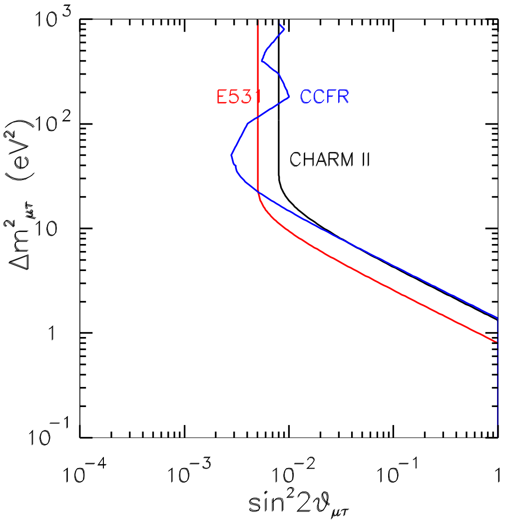

Figure 1.4: Exclusion plot for the $\nu_\mu \to \nu_\tau$ search obtained by E531, CCFR and CHARM II experiments.

the probability, i.e. for

$$\Delta m^2 \simeq \frac{\pi}{2} \frac{E}{1.267L}$$

Moreover typically the upper limit on the probability is much less than one. Then, in the region of small Δm^2, where $\sin^2 2\theta$ is large, the oscillation probability can be approximated by

$$P = \sin^2 2\theta \left(1.267 \frac{\Delta m^2 L}{E}\right)^2$$

which is a straight line in $\log \sin^2 2\theta - \log \Delta m^2$ plane.

1.3.2 Matter oscillation

The description of matter neutrino oscillation is a difficult and long argument. In this paragraph only the general idea is described in order to understand the solar and atmospheric neutrino experiments results, for a complete treatment see [1].

If neutrino propagates in matter, as it happens for solar neutrinos and atmospheric neutrinos inside earth, the oscillation may differ from oscillation in vacuum in a very significant way. Matter can enhance neutrino mixing, and the oscillation probability in matter can be large even if the mixing angle in vacuum is very small: this effect is known as the Mikheyev-Smirnov-Wolfenstein(MSW) effect.

This effect is due to the different interactions that the three neutrino flavours have in matter. All flavours interact with the electrons, protons and neutrons through neutral current interactions while ν_e has in addition charged current interactions with the electrons of the medium. The charged current interaction of ν_e with electrons creates a potential that must be added to the free Hamiltonian. This potential term can be evaluated by means of the Fermi Hamiltonian integrating over all the electron variables

$$\langle H_{Fermi} \rangle_{electron} \equiv V = \sqrt{2} G_F N_e \tag{1.41}$$

where G_F is the Fermi constant and N_e is the electron density of the medium. The equation of motion of neutrino in matter is easier written in terms of flavour eigenstates base where the Hamiltonian is the sum of the free one plus the term describing the ν_e CC interaction with the medium. For instance considering only two neutrino species, ν_e and ν_μ, we have

$$i\frac{d}{dt}\begin{pmatrix} \nu_e \\ \nu_\mu \end{pmatrix} = \begin{pmatrix} -\frac{\Delta m^2}{4E}\cos 2\theta_0 + \sqrt{2} G_P N_e & \frac{\Delta m^2}{4E}\sin 2\theta_0 \\ \frac{\Delta m^2}{4E}\sin 2\theta_0 & \frac{\Delta m^2}{4}\cos 2\theta_0 \end{pmatrix} \begin{pmatrix} \nu_e \\ \nu_\mu \end{pmatrix} \tag{1.42}$$

where θ_0 is the vacuum mixing angle. The solution of 1.42 in case of constant density gives a mixing angle in matter

$$\sin\theta = \frac{\left(\frac{\Delta m^2}{2E}\right)^2 \sin^2 2\theta_0}{\left(\frac{\Delta m^2}{2E}\cos\theta_0 - \sqrt{2} G_F N_e\right)^2 + \left(\frac{\Delta m^2}{2E}\right)^2 \sin^2\theta_0} \tag{1.43}$$

It has a typical resonance form and, if the condition

$$\sqrt{2} G_F N_e = \frac{\Delta m^2}{2E}\cos\theta_0 \tag{1.44}$$

is satisfied, the mixing angle is maximum independently from the vacuum value.

Let's now describe in a semi-quantitative way a more realistic case: the case of slowly (adiabatically) decreasing matter density. Let's consider an electron born in the sun core and assume that there the electron density is far above the resonance value (1.44). The mixing angle is $\sim 90^\circ$ thus the produced ν_e almost coincides with ν_2, the heaviest mass eigenstate. Since the matter density changes slowly along the neutrino propagation, the neutrino system has enough time to adjust itself and the transition between ν_2 and ν_1 is exponentially suppressed: thus the system remains in ν_2 state. However the flavour composition of this mass state changes during the propagation because the mixing angle is a function of density. When ν_2 reaches the sun surface, where the electron density is very small, $\theta \simeq \theta_0$ and its composition in term of flavour eigenstate is $\simeq \cos\theta_0 \nu_\mu + \sin\theta_0 \nu_e$. Therefore an electron produced in the solar core exits from the sun with a probability equals to $\cos^2\theta_0$ to be revealed as a ν_μ: in case of small mixing angle ν_e has been almost completely converted in a ν_μ.

1.4 Indications of neutrino oscillation

The first experiment that obtained some hints in favor of neutrino oscillation was a solar neutrino search carried out in the Homestake mine in the early '70. During the last 30 years a large number of experiments strengthened this hypothesis measuring neutrino fluxes from different sources: solar, atmospheric and accelerator. We will now briefly discuss the existing experimental data.

Prior to discuss the results let's recall some general characteristic of neutrino oscillation experiment. They fall roughly in two categories: disappearance and appearance experiments. In a disappearance experiment, using a beam of flavour l, the absence of some of the ν_l flux respect to the expected quantity is searched for. In an appearance experiment the presence of $\nu_{l' \neq l}$ is sought. Generally the appearance of a flavor non present on the original beam is considered a more convincing signal of oscillation than the disappearance of some fraction of neutrino beam whose total flux may be uncertain. However the disappearance experiments are the only one that could find signal of oscillation in sterile neutrinos. Anyhow to establish the occurrence of neutrino oscillation without doubt it is desirable to observe not only a disappearance or an appearance of neutrinos, but also a modulation of this phenomena with L/E. Usually all kind of experiments use to tag the flavor of the observed neutrino through the observation of the charged current interactions. Of course it is possible only if neutrino energy is high enough to produce the charged lepton. Otherwise it is possible to use the neutral current interactions which help at least to discriminate between oscillation in active or sterile neutrinos.

1.4.1 Solar neutrinos

The major part of the energy of the sun (98%) is produced in the reaction of the thermonuclear pp cycles shown in fig. 1.5. Neutrinos are emitted in six reactions

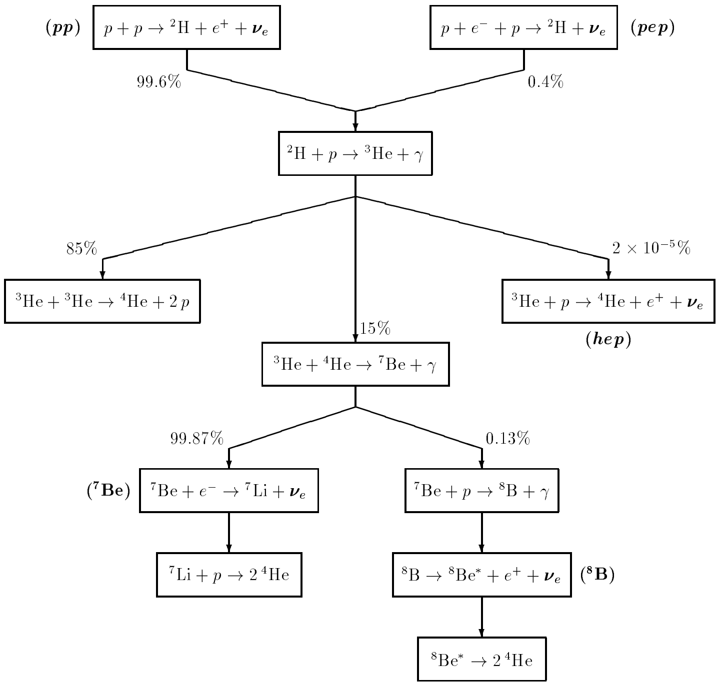

Figure 1.5: Energy generation in the sun through pp cycle

of the solar pp cycle: three of these give monochromatic energy lines, the others produce neutrino with continuum spectra (fig 1.6) The flux of solar ν_e has been calculated by about 20 different groups of authors in the framework of standard solar models. All these calculations agree well with each other. Moreover the standard solar models are robust and recently they received further credibility from their very high accuracy in reproducing the solar sound velocities inferred from the helioseismological measurements. It has been estimated that the pp neutrinos flux prediction has a very small uncertainty (of the order of 1%), while the ^{8}B flux is uncertain of $\sim 20\%$. Anyhow what is uncertain is the relative flux while the energy spectra of each component is well predicted by standard nuclear physics.

Five different experiments have measured the solar neutrino flux using three

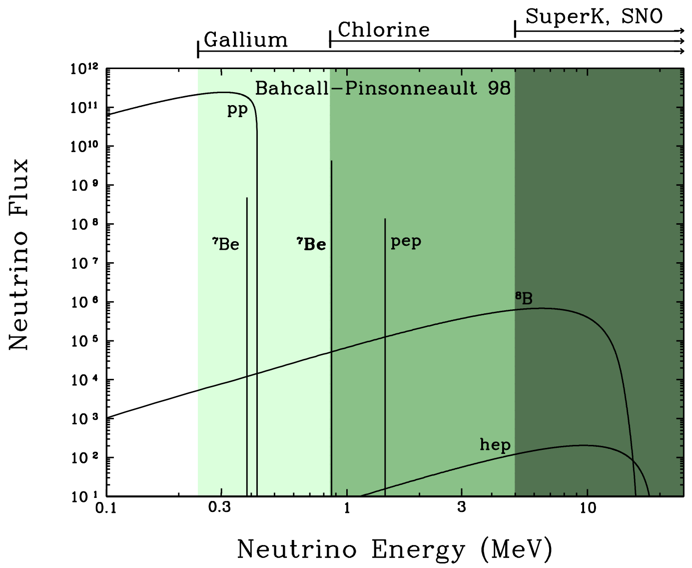

Figure 1.6: Energy spectrum of solar neutrinos from [9], with the thresholds of solar neutrino experiments.

techniques with different energy thresholds thus sampling three different admixtures of solar neutrino flux. Historically the first one was Homestake, to detect ν_e used the reaction

$$\nu_e +^{37} Cl \rightarrow e^- +^{37} Ar \tag{1.45}$$

as shown in figure 1.6 it is sensitive only to ^7Be, pep and ^8B, that is the largest contribution (fig 1.7). Other two experiments also used radiochemical techniques: SAGE and GALLEX. The used reaction is

$$\nu_e +^{71} Ga \rightarrow e^- +^{71} Ge \tag{1.46}$$

Due to their lower energy threshold they can detect also the pp neutrinos. Finally two experiments, Kamiokande and SuperKamiokande, detected solar neutrinos observing the Cerenkov light emitted by the electron scattered in the process

$$\nu_e + e^- \rightarrow \nu_e + e^- \tag{1.47}$$

They use real-time detector and are able to obtain information on the neutrino incident direction giving the first evidence that neutrinos are actually coming from sun direction.

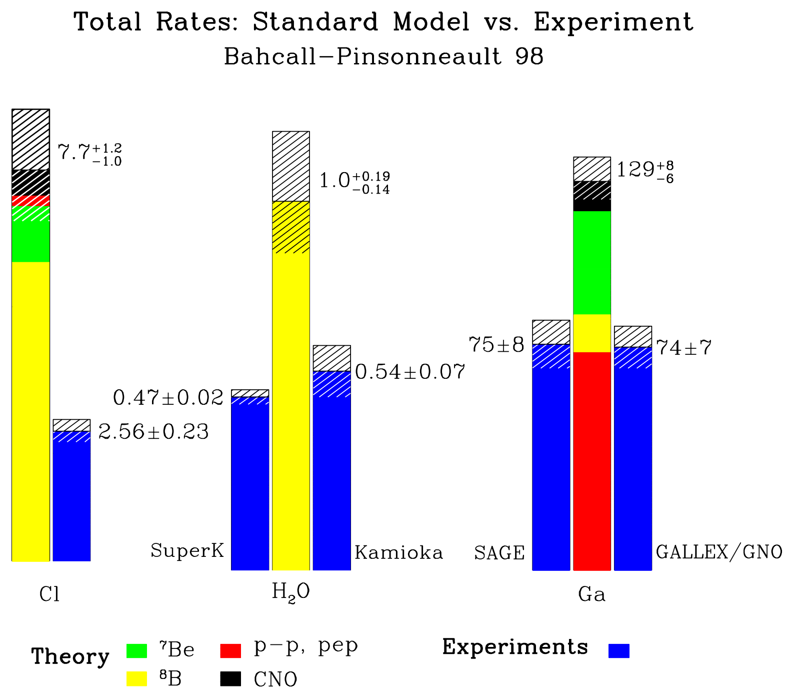

Figure 1.7: The plot compares the predictions of the standard solar model with the total observed rates in the five solar neutrino experiments. For both the experimental values and the predictions, the 1 sigma uncertainties are indicated by cross hatching

The results from these solar neutrino experiments are shown in figure 1.7. Strong deficits from the predicted flux, ranging from 30% to 60%, are observed. This is the essence of so-called *solar neutrino problem.* Different explanations to this problem have been proposed. Of course it could be due to some experiment-related errors but four out of five experiments have been carefully calibrated and results appear to be in good agreement with the expectations. The solar problem could also be due to an insufficient knowledge of solar physics, but the recent helioseysmological observations seems to exclude it. Moreover there are some checks independent from the SSM that strengthen the hypothesis of the need of a different solution of the solar problem One of these checks uses the luminosity constraint. Using the basic solar reaction

$$4p + 2e^- \rightarrow {}^4He + 2\nu_e + Q \tag{1.48}$$

where Q is the energy release, it is possible to have an approximate value of the total solar neutrino flux from the measurement of the solar luminosity. Employing this total flux estimation is possible to obtain model independent lower bound on the event rate measured in Gallium experiments. The lower bound is just compatible with SAGE and GALLEX results. A more convincing check comes comparing results from different experiments. Kamiokande and SuperKamiokande measure the ^8B neutrino flux, extrapolating this value to the chlorine experiments it turns out that all the event rate of Homestake is due to ^8B neutrinos. This result implies that there is a strong suppression of the expected SSM ^7Be neutrino flux, but this is incompatible with the fact that both ^8B and ^7Be originate from the ^7Be nuclei. Repeating the same extrapolation to the gallium experiment and combining with the luminosity constraint, the measured gallium event rate results smaller that the model independent lower bound with a probability larger than 94%.

Since it seems not so probable that the explanation of the solar problem comes from an improvement of the description of the solar model, it is natural to look for a solution linked to neutrino physics. There are several possible particle physics solutions but the most natural is the neutrino oscillation. In this hypothesis part of the ν_e produced in the solar pp chain before reaching the earth oscillates in some other flavor or in a sterile neutrino not detectable in the experiments: so a deficit of ν_e is measured. Under the oscillation hypothesis the solar experiments fall in the disappearance category since they measure the $P(\nu_e \to \nu_e)$. The energy dependent reduction of solar neutrino data with respect to the SSM prediction can be analyzed in two mixing scheme either through vacuum oscillation or through MSW enhanced oscillation. Considering the MSW there are three allowed regions in $\Delta m^2, \sin^2 2\theta$ plane:

1. Small Mixing Angle solution with $\Delta m^2 \simeq 5 \times 10^{-4}\mathrm{eV}^2$ and $\sin^2 2\theta \simeq 6 \times 10^{-3}$
2. Large Mixing Angle solution with $\Delta m^2 \simeq 2 \times 10^{-3}\mathrm{eV}^2$ and $\sin^2 2\theta \simeq 0.76$
3. LOW mass region with $\Delta m^2 \simeq 8 \times 10^{-8}\mathrm{eV}^2$ and $\sin^2 2\theta \simeq 0.96$

For the vacuum oscillation hypothesis there are regions extended over large range of Δm^2, $\sin^2 2\theta$ values, the best fit values are $\Delta m^2 \simeq 8 \times 10^{-11}\mathrm{eV}^2$ and $\sin^2 2\theta \simeq 0.75$. If the oscillation is $\nu_e \to \nu_s$ there exists only one possible solution: the SMA. The 90% C.L. regions around the best solutions are shown in figure 1.8.

SuperKamiokande has performed other measurements that should be useful to discriminate between the different solutions. They measured the variation of the solar neutrino flux in nighttime with respect to daytime. During the night the

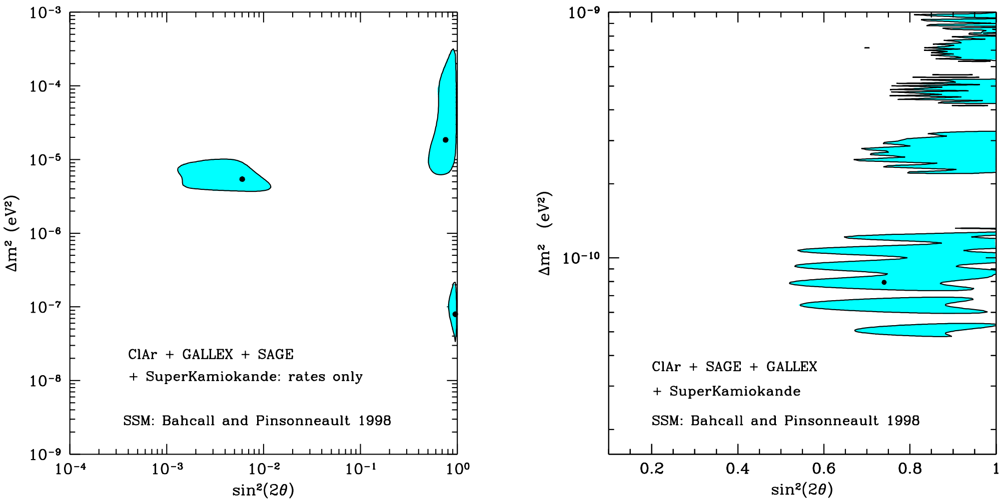

Figure 1.8: **Left panel:** the solutions for the allowed MSW oscillation regions known, respectively, as the SMA, LMA, and LOW solution. **Right panel:** the solution for the allowed vacuum oscillation region. The contours correspond to 99% CL

neutrinos pass through the earth and the matter effect can reconvert in ν_e part of the oscillated flux. The measured value of the asymmetry

$$\frac{D-N}{(D+N)/2} = -0.034 \pm 0.022 \pm 0.013 \tag{1.49}$$

favors the LMA solution for the solar problem. SuperKamiokande also measured the energy distribution of the recoil electron, which gives information about the spectrum of the incoming neutrinos. The ratio of this spectrum with the one predicted by SSM in the hypothesis of vacuum solution is consistent with a flat distribution but the statistics is low. A SK preliminary combined analysis of all solar neutrino data favored at 95% CL the LMA solution and excludes the oscillation in sterile neutrino.

The experimental situation is far from being clear. To improve the understanding of the solar neutrino problem new experiments are under construction or have already started data taking: their results should verify whether the oscillation hypothesis is the correct one. The BOREXINO experiment will measure the ^{7}Be neutrino flux. If the MSW effect is operative the event-rate will be reduced with respect to the one expected by SSM and its value may discriminate between SMA and LMA solutions. In addition the high statistics of BOREXINO will allow to measure seasonal variation which is expected to be large if the vacuum solution is correct. To clarify whether the ν_e oscillates in active or sterile neutrino the contribution of the SNO experiment will be very relevant. It will detect both CC and NC cross section measuring the total solar neutrino flux of the active neutrinos. Comparing the measured total flux with the ν_e flux SNO will be able to distinguish between solar neutrino oscillation in active or sterile neutrino. So it is probable that the combined data of the currently operating experiments with the new ones will allow to finally resolve the solar problem.

1.4.2 Atmospheric neutrinos

Electron and muon neutrinos and antineutrinos are produced in the hadronic showers induced by cosmic rays in the atmosphere: they are called atmospheric neutrinos. They are produced mainly by the following processes

$$\begin{array}{rcl} p(\alpha,...)+Air & \rightarrow & \pi^{\pm}(K^{\pm}) \quad + \quad X \\ & & \pi^{\pm}(K^{\pm}) \quad \rightarrow \quad \mu^{\pm}+\nu_{\mu}(\bar{\nu}_{\mu}) \\ & & \qquad\qquad \mu^{\pm}\rightarrow e^{\pm}+\nu_e(\bar{\nu}_e)+\bar{\nu}_{\mu}(\nu_{\mu}) \end{array} \tag{1.50}$$

From the chain reaction above we expect naively that the ratio of the two flavors $(\nu_\mu+\overline{\nu}_\mu/\nu_e+\overline{\nu}_e)$ is equal to 2:1. Actually accurate calculation of atmospheric neutrinos fluxes is a difficult task that depends on the knowledge of many ingredients as spectra and composition of cosmic rays, π and K cross section production, geomagnetic effects. Thus the systematic uncertainty in the flux calculation is rather large, of the order of 20-30%. Instead the ratio of the two flavors, which is less sensitive to the above listed uncertainties, is estimated to have an error of about 5%. This ratio has been measured by different experiments. The first generation detectors, which actually were originally designed to search for proton decay, NUSEX, Soudan, IMB, Frejus and Kamiokande reported the ratio between the measured value and its predicted value based on Monte Carlo simulation:

$$R=\frac{[N(\nu_\mu+\overline{\nu}_\mu)/N(\nu_e+\overline{\nu}_e)]_{Data}}{[N(\nu_\mu+\overline{\nu}_\mu)/N(\nu_e+\overline{\nu}_e)]_{MC}}. \tag{1.51}$$

As shown in figure 1.9 some of them measured for R a value smaller than the expected one. The discrepancy between the observed and predicted neutrino flavor ratio is referred to as the atmospheric anomaly. A second generation experiments, Superkamiokande, IMB-3, Soudan-2 and Macro, were used to carefully study the atmospheric neutrinos. All these experiments used the charged current interaction

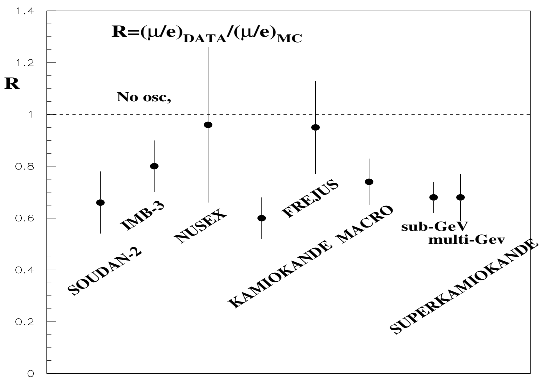

Figure 1.9: Measurements of the atmospheric neutrino flavor ratios

to tag the neutrino flavor. MACRO and Soudan-2 are tracking calorimeter detectors: distinguishing between shower or tracks permits to separate events with μ or e lepton final state. Superkamiokande and IMB-3 are water Cerenkov detectors, they identify the lepton flavor using the Cerenkov ring which is sharp for μ and diffuse for e. All these detectors, except MACRO, are sensitive to the track direction, thus they can distinguish between up-going and down-going neutrino. All these experiments confirmed the atmospheric neutrinos anomaly.

The discrepancy between R measured value with respect to the expected value was considered as an hint in favor of neutrino oscillation. To test this hypothesis more studies have been done from the SuperKamiokande collaboration. They ended up with signal which has been interpreted as an evidence for neutrino oscillation.

Before discussing the SuperKamiokande evidence let's describe briefly some details useful to understand the analysis. The atmospheric events are subdivided in several groups. Fully contained events (FC) are those for which both the interaction vertex and the point where the produced lepton stops are locate inside the detector. FC events are classified as sub-GeV or multi-GeV if the visible energy is below or above the 1.33 GeV value. Partially contained events (PC) are those for which the neutrino interacts inside the detector but the lepton gets out of it.

Using the fully contained events the atmospheric neutrino events zenith angle distribution has been derived. Actually what is measured is the angle distribution of the charged lepton produced in the neutrino CC interaction: the average angle between neutrino and charged lepton directions is about 17° for multi-GeV events and about 60° for sub-GeV. The zenith angle distribution is at first order a pathlength distribution. When $\cos\theta > 0$ the neutrino comes from the upper hemisphere so it has a pathlength of 15 up to 500 Km, whereas the up-going neutrinos ($\cos\theta < 0$) cross the earth so their pathlength is larger, up to 13,000 Km: thus as $\cos\theta$ increases the distance traveled by neutrinos decreases.

Figure 1.10 shows the zenith angle distribution separately for sub-GeV and multi-GeV ν_μ and ν_e events. Clearly for ν_e events, the measured distribution agrees very well with the predicted one for both sub-GeV and multi-GeV samples. Instead the ν_μ events distributions for both sample show zenith-angle dependent deficit compared to the expectations. These plots are perfectly consistent with an oscillation hypothesis. For multi-GeV muon events when $\cos\theta < 0$ the pathlength is comparable with the oscillation length thus the oscillation probability is large and the deficit is sizeable. As $\cos\theta$ increases the pathlength decreases consequently also the oscillation probability decreases: till for down-going neutrinos it becomes too short that they experience practically no oscillation. For the sub-GeV sample neutrinos the average energy is smaller thus they have a smaller oscillation length. Due to the smaller L_{osc} even down-going neutrinos are depleted by oscillation while up-going neutrino experience averaged oscillations.

An informative parameter that shows the ν_μ depletion is the zenith angle asymmetry as a function of momentum (fig: 1.11). The asymmetry is defined as A=(U-D)/(U+D) where U and D are respectively the number of upgoing ($\cos\theta < -0.2$) and downgoing ($\cos\theta > 0.2$) events. Since the neutrino flux is expected to be nearly up-down symmetric, in case of no oscillation the asymmetry should vanish. The ν_e events have an asymmetry compatible with the expectation while ν_μ events show for large momentum a negative asymmetry that differs from zero by almost 8σ (A=-0.32±0.04±0.01). The A distribution for ν_μ events can be understood in terms of oscillation. In fact for small momentum the oscillation length is small and up and down neutrino experience about the same oscillation probability and reduction. For higher momentum the oscillation length increases so only up-going neutrinos are depleted, therefore an asymmetry appears.

SuperKamiokande data are a very strong evidence in favor of the interpretation of the ν_μ deficit as an effect of neutrino oscillation. Which kind of oscillation are they? $\nu_\mu \to \nu_e$, $\nu_\mu \to \nu_\tau$ or $\nu_\mu \to \nu_s$? The $\nu_\mu \to \nu_e$ oscillation seems to be ruled out from the agreement of the ν_e zenith angle and asymmetry distributions with the expectation in case of no oscillation. Moreover since the ν_μ in the 2-flavor model oscillates with nearly maximal mixing and with Δm^2 in the range 10^{-2} to 10^{-3} eV^2

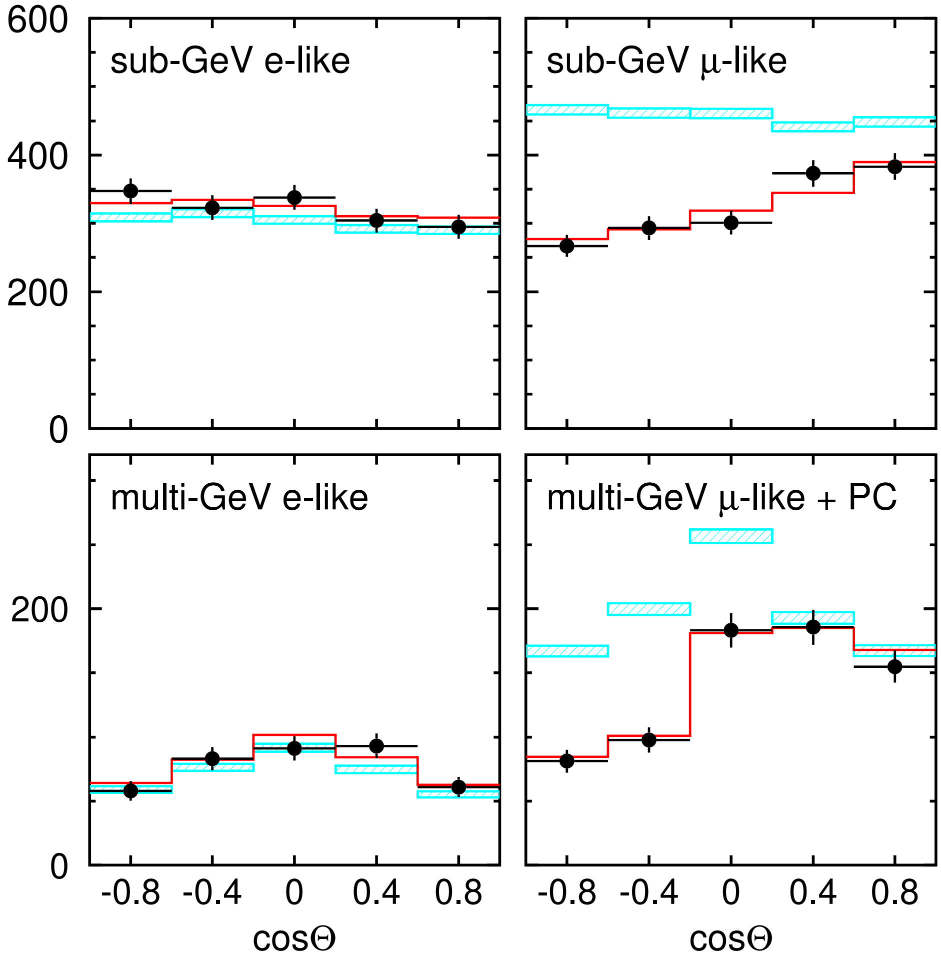

Figure 1.10: Zenith angle distribution for sub-GeV and multi-GeV ν_μ (μ-like) and ν_e (e-like) events in SuperKamiokande. The bars represent the Monte Carlo distribution expected in case of no oscillation. The line is the prediction if $\nu_\mu \to \nu_\tau$ oscillation occurs with the best fit-parameters.

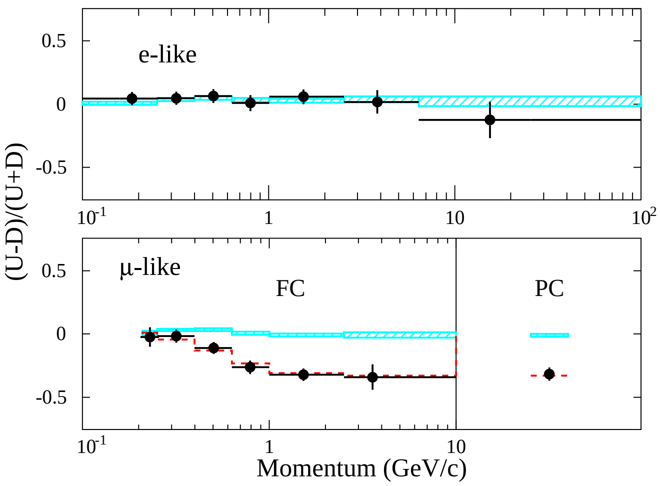

Figure 1.11: Zenith angle asymmetry distribution as function of momentum.

the CHOOZ experiment result ruled out the $\nu_\mu \to \nu_e$ occurrence. In fact CHOOZ reported a limit on $\overline{\nu}_e$ disappearance probability that at 99% CL excludes this region of Δm^2-$sin^2 2\theta$ plane. Of course $\nu_\mu \to \nu_e$ is excluded only as the dominant channel of the atmospheric neutrino oscillation, it is possible that it contributes as a sub-dominant mode in the 3-flavor model. Discriminating between $\nu_\mu \to \nu_\tau$ and $\nu_\mu \to \nu_s$ is more subtle: two different tests have been performed. $\nu_\mu \to \nu_\tau$ and $\nu_\mu \to \nu_s$ differ for the matter effect: ν_μ and ν_τ interact in the same way with the matter whereas ν_s does not interact at all. Therefore $\nu_\mu \to \nu_\tau$ oscillation is not affected by matter effect while $\nu_\mu \to \nu_s$ one is. The contribution of matter becomes important at high energy (see 1.44 where N_e must be replaced by $N_n/2$) when $\Delta m^2/2E \ll G_F N_n$, in this regime matter strongly suppresses oscillations. Using high energy up-going events the effect of matter has been searched for and it has been excluded at the 2σ level. Another test used to discriminate between the active or sterile neutrino is the measurement of the ratio of total single π NC interaction rate to the ν_e induced CC events. It is expected to be lower for oscillation in sterile neutrinos since they do not contribute to the single π productions. Due to the large uncertainty for the single pion NC production cross section the discrimination power of the test is still poor, nevertheless it prefers the $\nu_\mu \to \nu_\tau$ oscillations. The best fit for 2-flavor neutrino oscillations $\nu_\mu \to \nu_\tau$ gives the value $\Delta m^2 = 3.5 \times 10^{-3}\text{eV}^2$ and $\sin^2 2\theta = 1.0$ with $\chi^2/d.o.f. = 67.5/82$, the allowed region is shown in figure 1.12.

Although the SuperKamiokande evidence in very impressive further checks

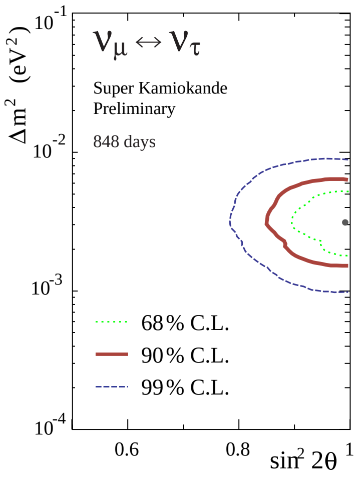

Figure 1.12: SuperKamiokande allowed region in $\Delta m^2, \sin\theta$ plane.

are searched for. Two other atmospheric neutrino experiments, Soudan-2 and MACRO, reported similar zenith dependent deficits, that, although less stringent, are in general agreement with the neutrino oscillation effects observed by SuperKamiokande.

A number of long baseline experiments have been proposed to test the SuperKamiokande oscillation claim. One of them, K2K, is already taking data and will be described in the next paragraph. Other two long baseline projects, NuMI (Fermilab to SOUDAN mine) and CNGS (CERN to Gran Sasso) are scheduled to start data taking in the next years (2002 2005 respectively). Both have a baseline of about 730 Km and will be able to test the whole allowed region of the SK results using different techniques. The MINOS experiment is planned to look for ν_μ disappearance and spectrum distortion due to $\nu_\mu \to \nu_x$ oscillation using the NuMI neutrino beam. Instead two experiments, OPERA and ICARUS, are planned to search for $\nu_\mu \to \nu_\tau$ in the appearance mode employing the CNGS neutrino beam.

1.4.3 Accelerator neutrinos

LSND LSND (Liquid Scintillator Neutrino Detector) claimed observation of neutrino oscillation. It is the only one coming from a human-made neutrino beam, thus from a controlled source. Let's briefly describe the observation. LSND used the neutrino beam of the LAMPF accelerator. It is produced by the interaction of 800 MeV kinetic energy protons with water. Most of the π^+ generated in this interaction are stopped in the water target and decay into muons that stop in the target and decay just as well. The detector is a cylindrical tank filled with scintillating mean, mainly mineral oil (CH_2).

In the π decay chain

$$\begin{array}{lll} \pi^+ & \rightarrow \mu^+ & +\nu_\mu \\ & \quad\downarrow & \\ & \quad e^+ & +\nu_e + \bar{\nu}_\mu \end{array} \tag{1.52}$$

no $\bar{\nu}_e$ is originated and when the μ decays at rest the electron antineutrino has an energy below $m_\mu/2 = 52.8MeV$. A small component of $\bar{\nu}_e$ prompt is present and it is originated from the same chain initiated by π^-. It is suppressed by a factor about 8×10^{-4}. This very high suppression factor makes the $\bar{\nu}_\mu \rightarrow \bar{\nu}_e$ appearance search possible. The $\bar{\nu}_e$ is detected through the chain reaction

$$\begin{aligned} \bar{\nu}_e + p &\rightarrow e^+ + n \\ n + p &\rightarrow d + \gamma \end{aligned} \tag{1.53}$$

i.e. the signature is a delayed coincidence between a positron and a γ of 2.2 MeV. A background for this search comes from the reaction $\nu_e +^{12}\mathrm{C} \rightarrow e^- +^{12}\mathrm{N}$, but it can produce electron with maximum energy of 20 MeV.

Analyzing the events with a positron of energy in the range 20-60 MeV an excess of about 51 events was found. The value of the corresponding oscillation probability is $(3.3 \pm 0.9 \pm 0.5) \times 10^{-3}$. The region of $\sin^2 2\theta, \Delta m^2$ corresponding to the LSND evidence is visible in figure 1.13.

A confirmation of the result comes from the analysis of the charge conjugate oscillation. The $\pi^+ \rightarrow \mu^+ + \nu_\mu$ decay in flight produces a ν_μ beam. The ν_e are detected using the reaction $\nu_e +^{12}\mathrm{C} \rightarrow e^- + \mathrm{X}$ for electron energy above 60 MeV and below 200 MeV. The lower bound assures to reject the ν_e from μ decay at rest, whereas the μ decay in flight is strongly suppressed by the lifetime. The ν_e detection has only one signature but the higher energy helps in the electron identification and direction measurement. They measured for the oscillation probability the value $(2.6 \pm 1.0 \pm 0.5) \times 10^{-3}$

The LSND claim has till now received no further and independent confirmation. The KARMEN experiment exploring the same region has excluded part of the LSND-allowed region. KARMEN is still improving its sensitivity to explore as much as possible all LSND region, but as visible in figure 1.14 it is expected that a narrow part will be not covered. Therefore other experiments with high sensitivity is needed to unambiguously confirm or refute the LSND evidence.

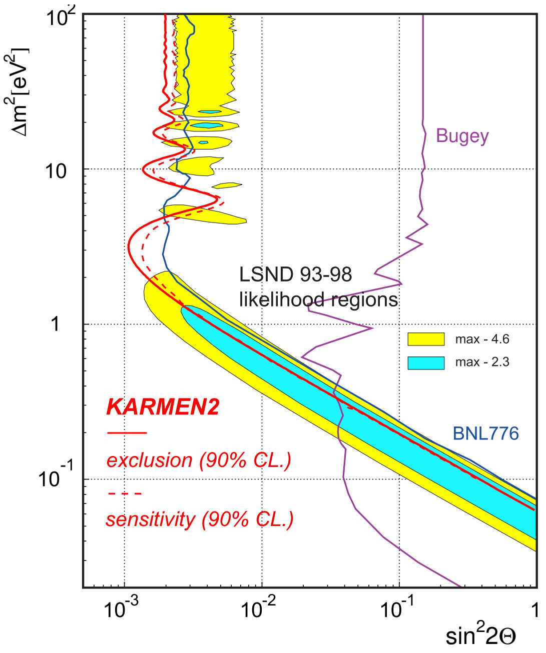

Figure 1.13: The region allowed by LSND evidence of $\bar{\nu}_\mu \to \bar{\nu}_e$ oscillation. The karmen updated result is superimposed.

An experiment that should shed light on the LSND result is Mini-BOONE. It has been approved and will start taking data in the year 2002. The coverage of the LSND region in case of observation of no signal is reported in figure 1.14.

K2K Prior to conclude this section of the description of hint in favor of neutrino oscillation let's briefly discuss the K2K preliminary result. K2K is a long baseline accelerator experiment designed to test the region of the parameters space allowed by SK. K2K employs the ν_μ wide-band beam produced by the 12 GeV proton synchrotron at KEK. A near station, 1 Kton water Cerenkov detector plus a fine-grained scintillating fiber tracking device, is located 300 m away the proton target. The far station is the SK detector placed at distance of 250 Km from the ν_μ source. Comparing the flux and spectrum of neutrino at the near and far station it is possible to measure to oscillation probability for the disappearance of ν_μ. K2K started data taking in 1999. The results presented till now excludes the non oscillation hypothesis at 2 σ. This result, although very preliminary, is very important since it is the first "preliminary" confirmation to the SK evidence using a human-made, thus better controlled, neutrino beam [10].

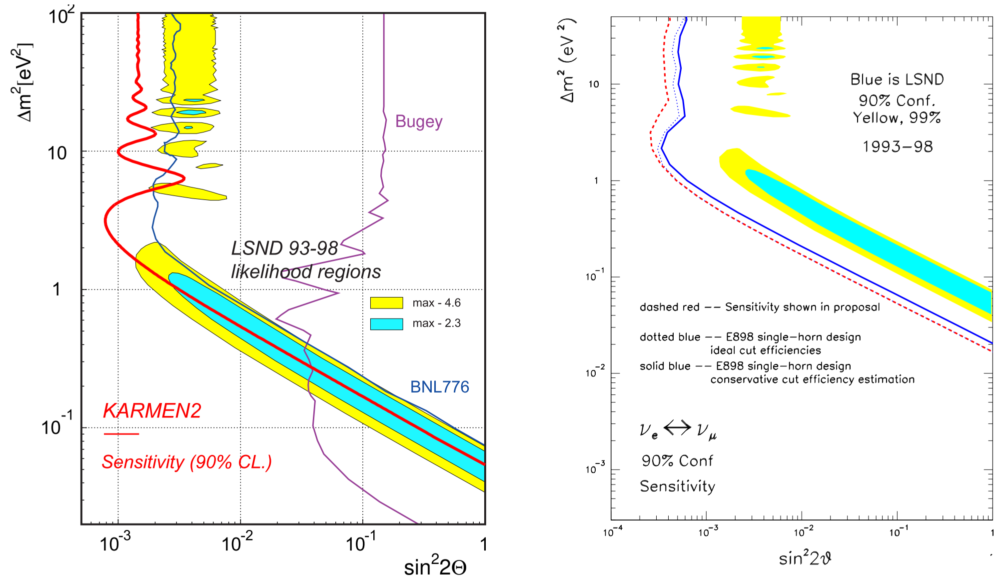

Figure 1.14: **Left panel:** The expected sensitivity of KARMEN experiment in case of no signal. **Right panel:** The expected sensitivity of mini-BOONE experiment in case of no signal.

1.4.4 Possible mass scenarios

Let's now briefly describe how the different hint of neutrino oscillation can be accommodated in a coherent scenario for the neutrinos mass. For further details see [11].

We know from the measurement of the Z^0 width that only three families of light neutrinos couple with the weak interaction. Assuming that they are the only existent light neutrinos it is possible to write the equation for the sum of the three mass splitting:

$$\sum_{\mathrm{i,j=1,3}} \Delta m_{i,j} = (m_3^2 - m_2^2) + (m_2^2 - m_1^2) + (m_1^2 - m_3^2) = 0. \qquad (1.54)$$

This condition is not satisfied by the Δm^2 determined or suggested by the experimental observations described in the previous sections (tab. 1.4).

There are two main way-outs at this problem. The first one is to reject the LSND evidence. With this assumption it is possible to explain the atmospheric and solar neutrino observations using only the three standard families of neutrino. If the mass scale obeys to the normal mass hierarchy, $m_1 << m_2 << m_3$, the

Experiment	Favored Channel	Δm^2 [eV^2]	$\sin^2 2\theta$
LSND	$\bar{\nu}_\mu \to \bar{\nu}_e$	0.2–2.0	$(1.5–40) \cdot 10^{-3}$
Atmospheric	$\nu_\mu \to \nu_\tau$	$3.5 \cdot 10^{-3}$	1
	$\nu_\mu \to \nu_s$	Disfavored at $\sim 2\sigma$	
Solar			
MSW (LMA)	$\nu_e \to \nu_\mu$ or ν_τ	$(1.3–18) \cdot 10^{-5}$	0.6–0.95
MSW (SMA)	$\nu_e \to$ anything	$(0.4–1) \cdot 10^{-5}$	$(0.7–10) \cdot 10^{-3}$
Vacuum	$\nu_e \to \nu_\mu$ or ν_τ	$(0.05–5) \cdot 10^{-10}$	0.6–1

Table 1.4: Experimentally favored neutrino mass differences and mixing angles.

three possible solutions, corresponding to the three suggested explanations for the solar problem, are represented in figure 1.15. The normal mass hierarchy is not the only possible scheme, another one is the so-called inverted mass hierarchy, where the mass eigenstates satisfies the condition $m_3 << m_1 \simeq m_2$. Within the assumption of the inverted mass hierarchy the position of ν_3 and the pair ν_1, ν_2 are interchanged. Since the oscillation experiments measure only the difference of mass, it is possible that the neutrinos mass are quasi degenerate and that only their differences are in the normal or inverted hierarchy. This case is very interesting for cosmology since three neutrinos species with masses $\sim eV$ would contribute significantly to the dark matter.

There exists an explanation that can fit all the observations without rejecting the LSND result. If the LSND result is correct we need at least four light neutrino species: i.e. the usual three neutrinos plus a sterile one. A solution, but not the only one, that can accommodate all the data is shown in figure 1.15.

1.5 The CHORUS role

The CHORUS (CERN Hybrid Oscillation Research ApparatUS) experiment together with NOMAD, another CERN experiment which looks for the same phenomena with different techniques on the same neutrino beam line, has been designed to search for $\nu_\mu \to \nu_\tau$ oscillations with the aim to reach high sensitivity for small mixing angle in the region of large value of Δm^2: up to $\sin^2 2\theta_{\mu\tau} \simeq 2 \cdot 10^{-4}$ for $\Delta m^2 \geq 50 - 100\ eV^2$ according to the proposal.

The choice to explore with high sensitivity that region of the parameters space was suggested by the following argument [12]. Let's make the hypothesis that

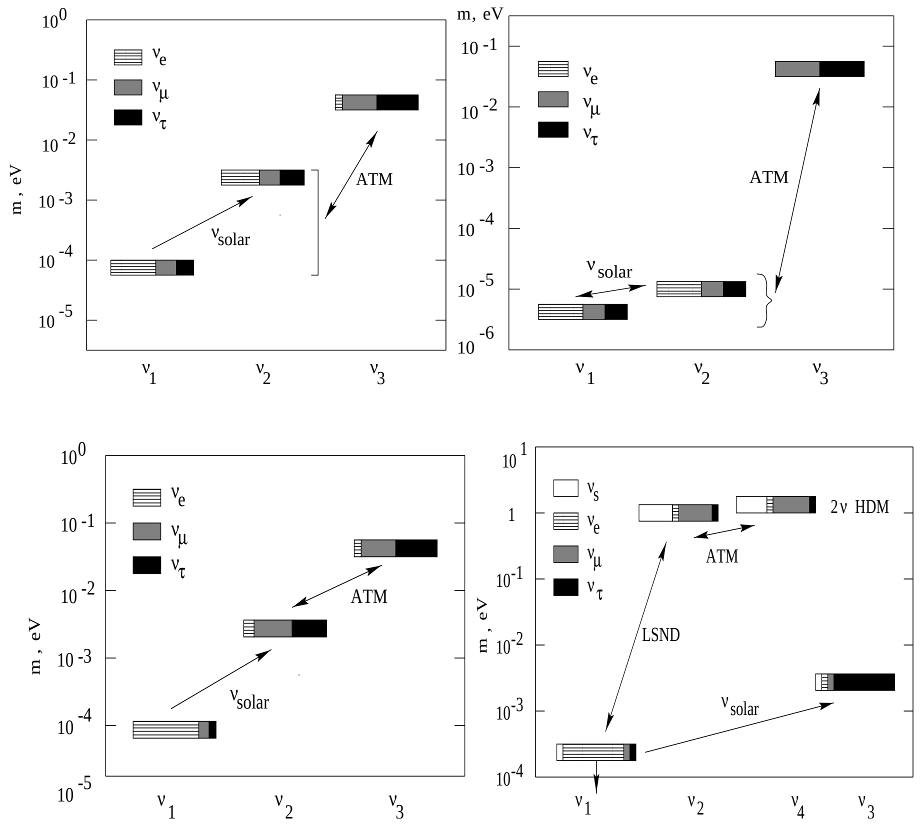

Figure 1.15: The boxes correspond to mass eigenstates, the sizes of different regions in the boxes show admixtures of different flavors. Weakly hatched regions correspond to the electron flavor, strongly hatched regions depict the muon flavor, black regions present the tau flavor. The top panels and the bottom left one are the solution assuming only three neutrino flavours and the normal mass hierarchy. The three panels correspond to the different solar problem solutions. Top-left panel SMA solution, top-right panel LMA solution, bottom-left panel VO solution. The bottom right panel represents the mass scheme with the sterile neutrino assumption for the SMA solution of the solar problem.

the neutrinos mass is the answer to the dark matter, then the sum of the mass of neutrino species should be of $\sim 15 - 65\ eV$. Let's assume also that the see-saw model for the neutrino mass is correct. It yields to the mass hierarchy in equation 1.34 or 1.35 therefore the largest neutrino mass is at least two order of magnitude greater than the two others. It means that only one neutrino species contributes significantly to the dark matter: the ν_3 with a mass of $\sim 15 - 65\ eV$. In case of small the mixing angle between different weak states then ν_3 is mainly composed by ν_τ and ν_2 by ν_μ, thus $\mathrm{m}_{\nu_\tau} \sim \mathrm{m}_3$. Under these assumptions the squared mass splitting between ν_τ and ν_μ is $\sim m_\tau^2 \geq 100\ eV^2$: therefore the idea to explore with the highest possible sensitivity in $\sin^2 2\theta_{\mu\tau}$ the large Δm^2 region.

As discussed above the most updated cosmological analysis suggests a smaller contribution of neutrino to the universe missing matter. Thus the previous motivation for the CHORUS research become weaker. Fortunately another consideration supports the search. If the solution of solar problem is the $\nu_e \rightarrow \nu_\mu$ oscillation with small mixing angle, then $\Delta m^2_{e,\mu} \sim 5 \cdot 10^{-6}\ eV^2$. If equation 1.34 is correct then

$$m_\tau = \left(\frac{m_t}{m_c}\right)^2 \cdot m_\mu \sim\ 30\ eV \tag{1.55}$$

thus in the region explored by CHORUS.

Unluckily all the previous motivations turn out to be wrong if the we believe to the SK claim for $\nu_\mu \rightarrow \nu_\tau$ oscillation evidence. In fact if the parameter that describes the $\nu_\mu \rightarrow \nu_\tau$ oscillation are inside SK allowed region of the $\Delta m^2, \sin^2 2\theta_{\mu\tau}$ plane, the CHORUS search would be vain: no signal could be detected. Anyhow waiting for further confirmations of the SK result is worth to extract from the CHORUS data as much information as possible on the neutrino oscillation.

Chapter 2

The experimental set-up

In the following only a brief description of the experimental set-up used by CHORUS is given. A detailed description can be found in [13].

2.1 CERN Neutrino beam

The West Area Neutrino facility (WANF) of the CERN SPS provides a beam of ν_μ with energy mostly above threshold for ν_τ CC interactions, thus suitable for $\nu_\mu \to \nu_\tau$ oscillation search in the appearance mode.

2.1.1 The beam line

A schematic view of the beam line is depicted in figure 2.1. Protons are accelerated by the SPS to an energy of 450 GeV with a cycle of 14.4 s. Two protons spills of 6 ms length are extracted separated in time by 2.7 s. The spills are sent onto a beryllium target, assembled with 11 rods of 10 cm length (separated by 9 cm gaps) and of 3 mm diameter. The proton-beryllium interaction produces mainly pions and kaons. Positive (negative) mesons are focused (defocused) by two magnetic lenses, the horn and the reflector. Neutrinos originate by the meson decay in flight, mostly after the two magnetic lenses, in a 290 m long vacuum tunnel. Two helium-filled tubes are placed between the horn and the reflector and between the reflector and the decay tunnel. They allow to reduce the absorption of parent mesons before the entrance of the decay tunnel. Although the presence of the two lenses a few percent contamination of negative mesons is present. In order to reduce this background source a large angle collimator has been placed in front of the reflector to intercept negative mesons before their decay.

The neutrino beam has an upward slope of 42 mrad. The detector parts were centered along this slope, however, every part is placed vertically.

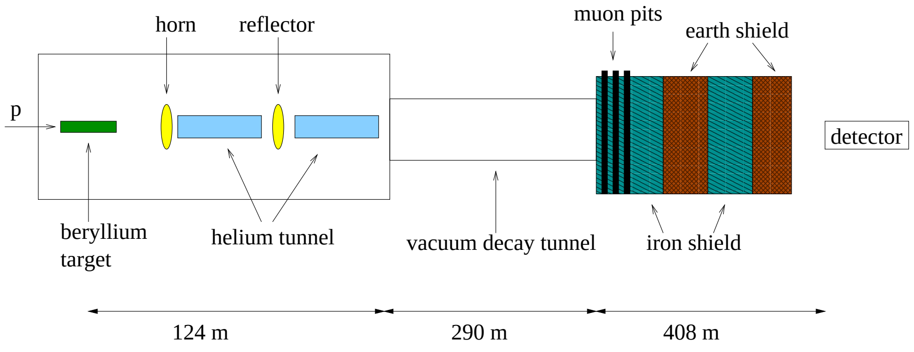

Figure 2.1: Neutrino beamline lay-out

2.1.2 The beam composition

The beam composition and spectra has been obtained by a full Montecarlo simulation of the whole beam line. A check of such results is possible using the fraction of CHORUS neutrino interactions occurred in the Calorimeter. The agreement between the simulated beam and the measured one is at the level of 10%, enough for the purpose of experiment [14]. The spectra obtained by the simulation is shown in figure 2.2.

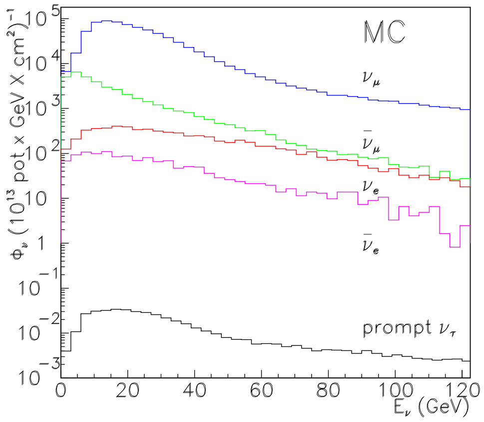

Figure 2.2: Neutrino beam composition

2.2 The CHORUS detector

The CHORUS apparatus consists of an emulsion target, a scintillating fiber tracking, an aircore hexagonal magnet, an electromagnetic and hadronic calorimeter and a muon spectrometer. A schematic picture is shown in figure 2.3.

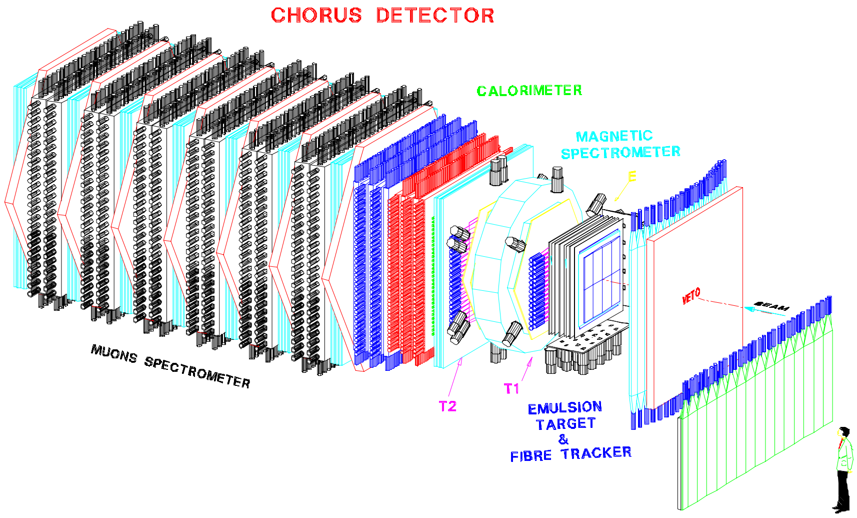

Figure 2.3: CHORUS detector layout

2.2.1 The emulsion target and the interface sheets

The emulsion set-up consists of two components: a massive emulsion target where neutrino interactions are recorded, also called "bulk", and thin emulsion sheets used to interface the tracks reconstructed by the fiber tracker and the emulsion target. An arrangement of half of the emulsion set-up is depicted in figure 2.4.

The volume of emulsion where neutrino interactions are searched is 260 l, corresponding to 770 Kg. It is divided in four stacks of about one radiation length and 0.08 interaction length each. Each stacks has a surface of $1.42 \times 1.44\ m^2$. It is composed piling-up 36 emulsion sheets in direction orthogonal to the neutrino beam. Each sheet, also called plate, is made by two emulsion gel layers of 350 μm thickness poured onto both faces of a 90 μm depth plastic base.

The interface sheets are composed by a 800 μm thick plastic base and two gel

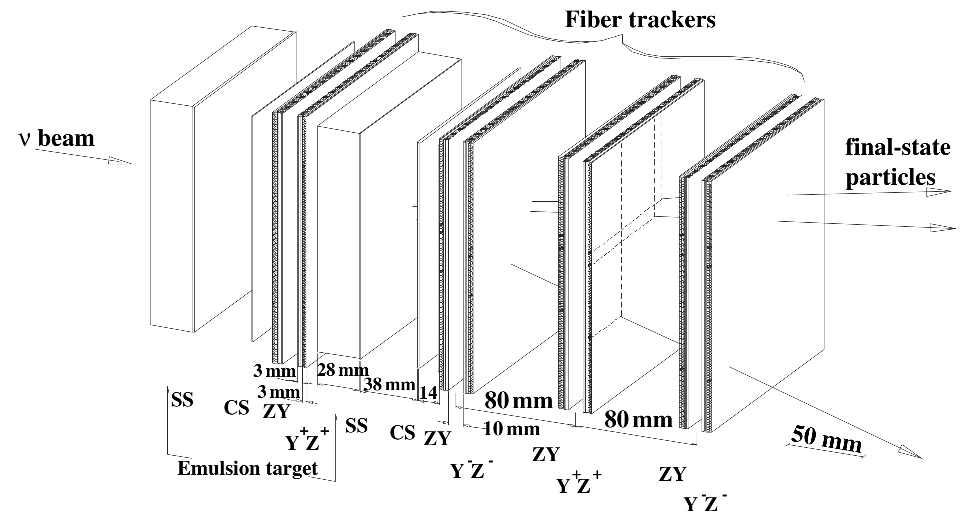

Figure 2.4: The geometry of half of the target region, showing the target emulsion stacks and the interfaces sheets and the target trackers.

layers of 100 μm depth. The different gel and base thicknesses of the emulsion sheets with respect to the bulk plate are due to the necessity to maximize the angular resolution to match the electronic detector event with the emulsion event. In fact the interface sheets have a larger level arm and less distortion due to the shrinkage of the emulsion during the its development.

Each emulsion stack was exposed for two years at the neutrino beam. Instead the interface sheets were changed more frequently to reduce the pile-up of events in order to improve the matching reliability between the electronic detector and the emulsion. The emulsion set-up was kept at a temperature of 5 $^\circ C$ to reduce fading.

2.2.2 The scintillating fiber tracker

The target tracker (TT) was built assembling more than 1 million plastic scintillating fibers of 500 μm in diameter. The fibers are grouped in layers of surface 1.6×1.6 m^2. Seven layers in a staggered geometry were packed together to get a ribbon. A tracker plane consists of four ribbons with different orientations (Y,Z and $\mathrm{Y}^{\pm}, \mathrm{Z}^{\pm}$ rotated by $\pm 8^\circ$ relative to Y and Z). Using the information from the four projective planes three dimensional tracks can be reconstructed without ambiguity. In total eight tracker planes were built, they were interleaved between the four target emulsion stacks.

The fiber tracker major role is to locate the stack were the neutrino interaction occurred and to make accurate track prediction on the interface sheets. Two conflicting requirements, the two-track separation and the accuracy of the prediction extrapolation on the interface sheets, were considered to optimize the position of the fiber tracker with respect to the emulsion stacks. The first plane was placed about 4 cm away from the stack. The first interface sheet was at the distance of 1 mm to the tracker. The position accuracy in the prediction onto this sheet is about 200 μm while the angular resolution achieved by the tracker is about 2 $mrad$.

The read-out is composed by 58 optoelectronic chains, each made up by four image intensifiers and a CCD camera. A maximum number of two events for spill could be recorded.

2.2.3 Air-core spectrometer

An air-core magnet of hexagonal shape is located between the target region and the calorimeter. It is used for the measurement of charge and momentum of particles before they enter the calorimeter. It is also employed to determine the momentum of the muons that don't reach the muon spectrometer.

Severe constraints were imposed during the magnet design. It was necessary to minimize the stray field that would prohibit the use of the electrostatic image intensifiers and would complicate the tracking. The magnet length has to be the minimum possible in order not to reduce the geometrical acceptance for the calorimeter and muon spectrometer. Moreover the material should be minimized to avoid large multiple scattering before and after the magnet that would diminish the momentum resolution.

A toroidal air-core magnet was built to satisfy these requirements. It is made of six equilateral triangles with 1.5 m sides and 0.75 m depth. Windings of thin aluminum sheets cover all the faces of the triangles producing a homogeneous field of 0.12 T, with no radial dependence and parallel to the outer side of the triangle.

Three planes of fibers, similar to those employed in the scintillating fiber tracker, measure the particle position and slope before and after the magnet field. The momentum resolution achieved for single track, where the pattern recognition does not complicate the measurement, is $\sigma(p)/p = 0.23 \oplus 0.037 \cdot p$ Due to the spokes of the magnet the geometrical acceptance is about 85%.

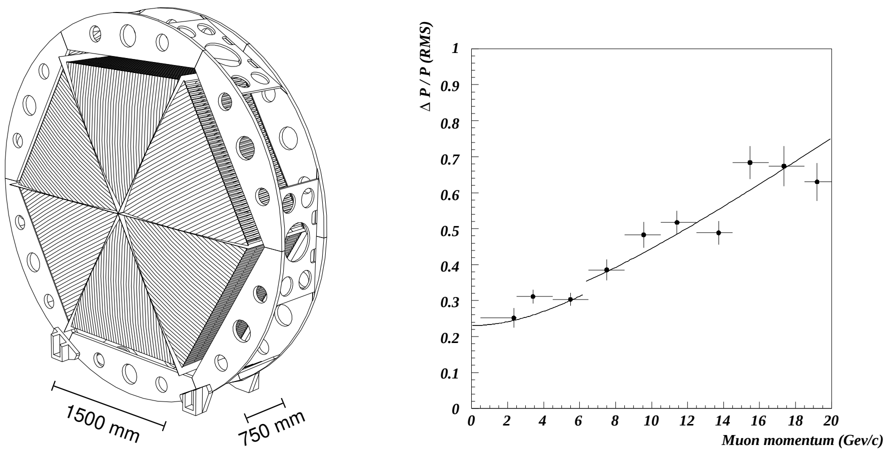

Figure 2.5: **Left panel:** drawing of the hexagonal magnet. **Right panel:** momentum resolution for single track event measured by the magnet trackers.

2.2.4 High resolution calorimeter

The calorimeter was originally designed to provide measurements of kinematic variables crucial to preselect the events in order to reduce the scanning load [15]. Since the scanning speed was improved very much from the start of data taking, the preselection using the calorimeter information was relaxed. Now the calorimeter information is mainly used to suppress the background during the post scanning analysis.

The most important feature is to measure with good angular and energy resolution the hadronic shower in neutral current events. The upstream part of calorimeter consists in scintillating fiber of 1mm diameter embedded into a lead matrix. This assures a good sampling. The lead to scintillator volume ratio is 4:1, ensuring good compensation thus good hadronic energy resolution. The fibers are placed in a direction orthogonal to the beam direction. The most downstream part consists in lead/scintillator-strip sandwich with the same volume ratio of 4:1. The total thickness of the calorimeter corresponds to X_0 and to 5.2 λ_{int}. To improve the muon identification efficiency, fourteen planes of streamer tube chambers were inserted between the modules (fig 2.6).

The measured response of the calorimeter at electron beam of several energies

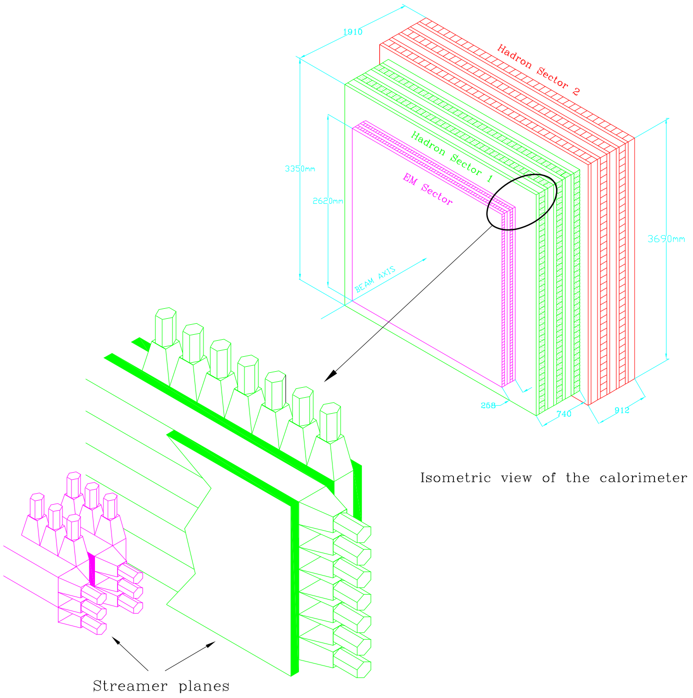

Figure 2.6: Calorimeter layout

has permitted to determine the electromagnetic energy resolution

$$\frac{\sigma(E)}{E} = \frac{(13.8 \pm 0.9)\%}{\sqrt{E(GeV)}} + (-0.2 \pm 0.4)\% \tag{2.1}$$

Similarly the hadronic energy resolution has been obtained

$$\frac{\sigma(E)}{E} = \frac{(32.3 \pm 2.4)\%}{\sqrt{E(GeV)}} + (1.4 \pm 0.7)\% \tag{2.2}$$

2.2.5 Muon spectrometer

The role of the muon spectrometer in CHORUS is to identify muons and determine their trajectory, charge and momentum. Since the spectrometer is located behind the calorimeter only the muons with energy greater than about 1.5 GeV reach it. As displayed in figure 2.7, the spectrometer is constructed by six magnetized iron toroid modules and tracking detectors consisting of drift chambers and streamer tubes. In addition scintillating planes interleaved with the magnet iron provide a measurement of the leakage of hadronic shower from the back of the calorimeter. The fast signal from these scintillator planes are also used for triggering.

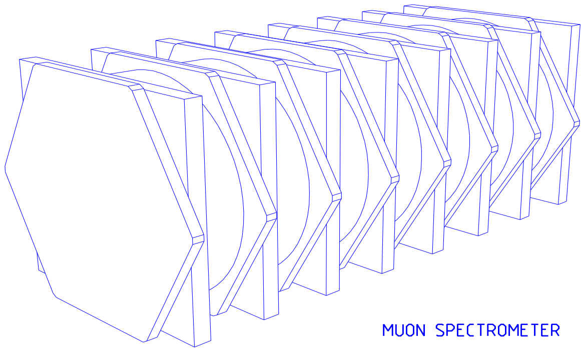

Figure 2.7: Muon spectrometer layout

The momentum resolution of the muon spectrometer is about 19% at 70 GeV, as measured with test beam muons. At lower momentum it is determined with the help of a Montecarlo simulation and the result is shown in figure 2.8

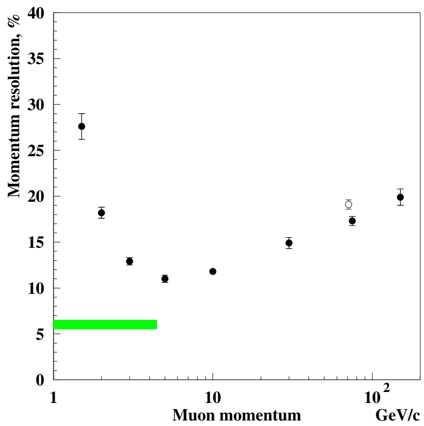

Figure 2.8: The muon spectrometer momentum resolution. Full dots: Montecarlo events. Open dot: test beam. The shaded band corresponds to muon stopping in the spectrometer, with their momentum measured by range

2.2.6 The trigger system

The scintillator trigger-hodoscopes E,T,H,V and A, shown in fig 2.9, are used to select neutrino interactions in the target and to reject background from cosmic rays, beam muons and neutrino interactions outside the target. A neutrino trigger in the target region is defined by a hit coincidence in E,T and H consistent with a particle trajectory with $\tan\theta < 0.25$ with respect to the neutrino beam direction.

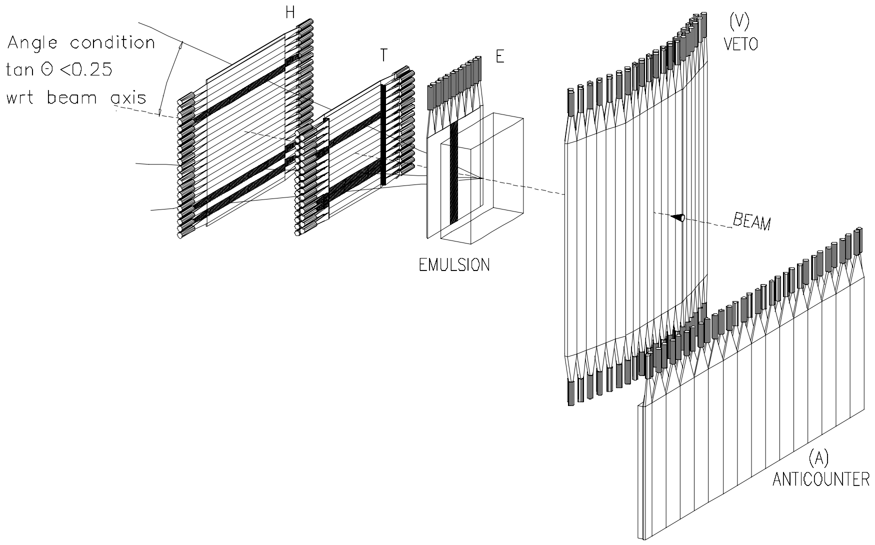

Figure 2.9: Schematic layout of the trigger hodoscopes

A veto is formed by any combination of a counter hit in the veto hodoscopes (V and A) and a hit in T, with precise timing to avoid vetoes due to backscattering.

The measured rate of neutrino interactions is 0.5 events per 10^{13} protons on the SPS target corresponding to an effective neutrino target mass of 1600 Kg. The fraction of those events originated in the emulsion target is 50%. Owing to the high redundancy of the trigger system and to the simplicity of the requirements, a trigger efficiency of 99% (90%) was measured for ν_μ charged (neutral) current events.

2.2.7 Upgrades for the 1996-1997 runs

Two detector upgrades have been installed during the 1996 data taking.

• **The honeycomb tracker** The honeycomb tracker chambers have been installed in the apparatus to complement the existing magnet trackers by providing a module with independent tracking capabilities and a similar spatial resolution. The honeycomb chambers have replaced the six planes of streamer tubes planes located between the calorimeter and the trigger H-hodoscope planes.

The basic structure of the honeycomb chambers is a plane of hexagonal cells, each cell acting as a single-wire drift chamber with a measured relation between space and drift time. Six planes suitably staggered form a chamber. Three chambers are installed at 60°, 0° and 120°

- **The emulsion tracker** In addition to the magnet trackers, the air-core hexagonal magnet region has been equipped with emulsion trackers. The aim is to improve the momentum accuracy. Three emulsion sheets have been installed: one upstream of the hexagonal magnet and two immediately downstream. The idea is to use the emulsion trackers for the post scanning analysis in order to reduce the background especially for the $\tau^- \rightarrow \mathrm{h}^-(n\pi^0)\nu_\tau$ decay. It has been estimated that the momentum resolution σ_p/p should be about 22% at 10 GeV and 37% at 30 GeV.

2.3 The emulsion scanning technique

The emulsion provides three-dimensional images of the trajectories with a grain ("hit") size of 1 μm and an average density of 300-400 hits per millimeter for minimum ionizing particles. Considering that the total volume of the all CHORUS emulsion are about 500 l, the total amount of hits recorded is very high. To analyse those informations in a fast way an "automatic" system has been developed during the course of the experiment [16]. Schematically it works in the following way. The entire emulsion plate is placed on the microscope stage and kept flat by vacuum. Immersion oil is put on the surface of the emulsion plate to optimize the light illumination of the microscope objective lenses. All the predicted tracks in that plate are searched one by one. The scanning system drives the microscope stage to the predicted position and detects the surface of the emulsion plate automatically (autofocus). The emulsion images at sixteen different focal depths are read by a CCD camera (see fig. 2.10). The "Track Selector", a realtime processor, digitizes the CCD video signals and sends the pixels of data into a dynamic frame memory. The predicted track is searched by superimposing the data with different shifts between layers. A track is identified by having an enhancement in the superimposed signals when the shift matches the angle of the track. For each found track the relevant parameters, slope and position are automatically measured and stored. The resolutions with which the parameters are determined depend on the thickness of the emulsion plates due to the shrinkage during the developing.

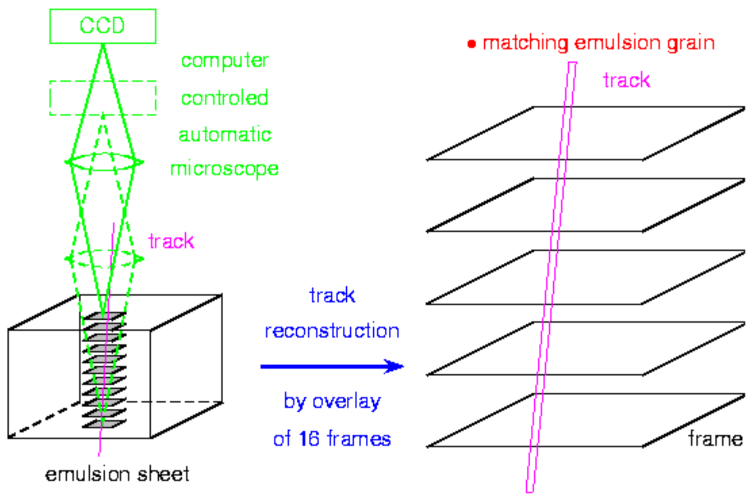

Figure 2.10: Schematic description of the track reconstruction procedure in the automatic scanning system

During these years of emulsion analysis the "Track Selector" performances improved incredibly (see tab. 2.1).

year	1994	1996	1999	2000
views/s	0.008	0.25	3	~30

Table 2.1: Number of views per second analyzed by the automatic system

It allowed to change the scanning procedure during the time. The load of the automatic part is augmented while the manual scanning load is decreased keeping quite constant the efficiency for the signal but saving human time.

Chapter 3

CHORUS neutrino oscillation search strategy

In this chapter the method used by the CHORUS experiment to measure the probability of $\nu_\mu \to \nu_\tau$ oscillation will be briefly discussed. The aim is to give an idea of all the elements needed for the probability evaluation, the objective of my thesis, so to give a coherent introduction to the other chapters where most of these elements will be calculated.

3.1 Conceptual strategy for ν_τ detection

The CHORUS experiment is an appearance experiment, it is designed to search for the presence of ν_τ in a ν_μ beam. The ν_τ is detected through its charged current interaction ν_τ N $\to$ τ^- X. Therefore to detect the $\nu_\mu \to \nu_\tau$ oscillation is mandatory to identify the short-lived τ^- lepton. At the typical energies of the CERN Neutrino Beam, the τ leptons that would be produced by oscillation with large Δm^2 thus with the same energy spectra as the ν_μ beam, would have an average flight path of the order of 2 mm (fig. 3.1). The small value of the τ decay path has suggested an hybrid approach to distinguish the occurrence of ν_τ CC interactions from the much more frequent ν_μ CC or NC interactions: an emulsion target for neutrino interactions and τ decays, plus an electronic detector. In fact the nuclear emulsion with its typical spatial resolution of the order of 1 μm is ideal for an unambiguous detection of short-lived particles. The signature of the ν_τ CC interaction in emulsion is a neutrino interaction vertex and the subsequent τ decay topologies (schematically shown in figure 3.2) . The decay topologies are one-prong decays, so-called “kink”, and multi-prong decays.

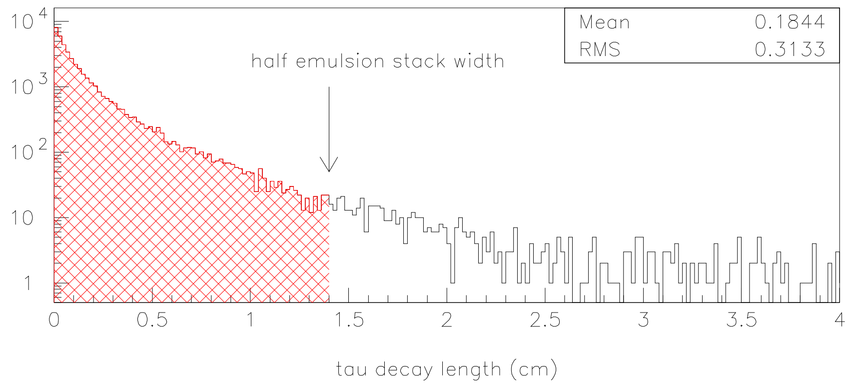

Figure 3.1: τ decay length distribution for CERN neutrino beam typical energies. The hatched zone represents the averaged fraction of τ originated and decayed inside one emulsion stack ($\sim$ 98%).

In the CHORUS current analysis only the one-prong decays are studied:

$$\tau^- \to \mu^- \nu_\tau \bar{\nu}_\mu \qquad BR = 17.4\% \tag{3.1}$$

$$\tau^- \to \mathrm{h}^-(n\pi^0)\nu_\tau \qquad BR = 49.5\% \tag{3.2}$$

$$\tau^- \to e^- \nu_\tau \bar{\nu}_e \qquad BR = 17.8\% \tag{3.3}$$

The requirement to get the highest sensitivity in a reasonable scanning time has led to the exclusion of the multi-prong decays in the first part of the analysis. In fact the detection of the multi-prong topology is more complicated than the kink one due to the smaller angle between the τ and the decay product, moreover it has higher background rate. Some studies have shown that with a dedicated scanning strategy and an accurate background treatment the inclusion of the 3-prong decay could improve $\sim$ 10% the CHORUS sensitivity. The multi prong decay will be added in a new phase of the analysis which is now under testing.

3.2 Analysis strategy for ν_τ detection

CHORUS has recorded in the emulsion target roughly 10^6 events during four years of data taking. According to the best upper limit on $\nu_\mu \to \nu_\tau$ oscillation probability available at the time of the experiment proposal [17], if the oscillation occurred in the region accessible to CHORUS, we would expect less than about

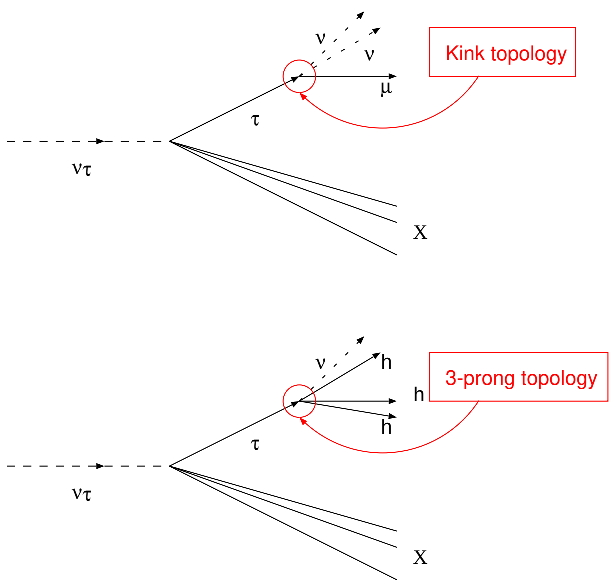

Figure 3.2: τ decay topologies: 1-prong decay, the so-called kink, and 3-prong

one thousand signal events. To detect these events of course a good efficiency is mandatory but at the same time a strict pre-scanning selection is needed to avoid an enormous amount of scanning load. The pre-scanning selection criteria have the aim to collect the events showing a "possible" τ decay product track in the electronic detector. All these τ daughter candidate tracks are scanned backward to the neutrino direction. When, during the scanback, all the τ daughter candidate tracks point to a vertex and no kink signature is detected on any of them, then a ν_μ interaction results located and the event analysis is stopped. Instead if a kink has been found kinematic cuts are applied to reduce the background rate prior to consider the event as a possible ν_τ candidate. Let's now discuss with more details the analysis flow whose schematic view is represented in figure 3.3.

3.2.1 Preselection

The starting sample is composed by all events triggered and recorded in the electronic detector. These events are processed by the CHORUS reconstruction program: the main part of the code, the scintillating fiber tracker algorithm, defines the position of the primary neutrino interaction vertex and the parameters of the tracks exiting from it. The longitudinal position resolution for the primary vertex is a few millimeters (fig 3.4). It is accurate enough to separate ν events originated inside emulsion from events occurred elsewhere (roughly half of the events

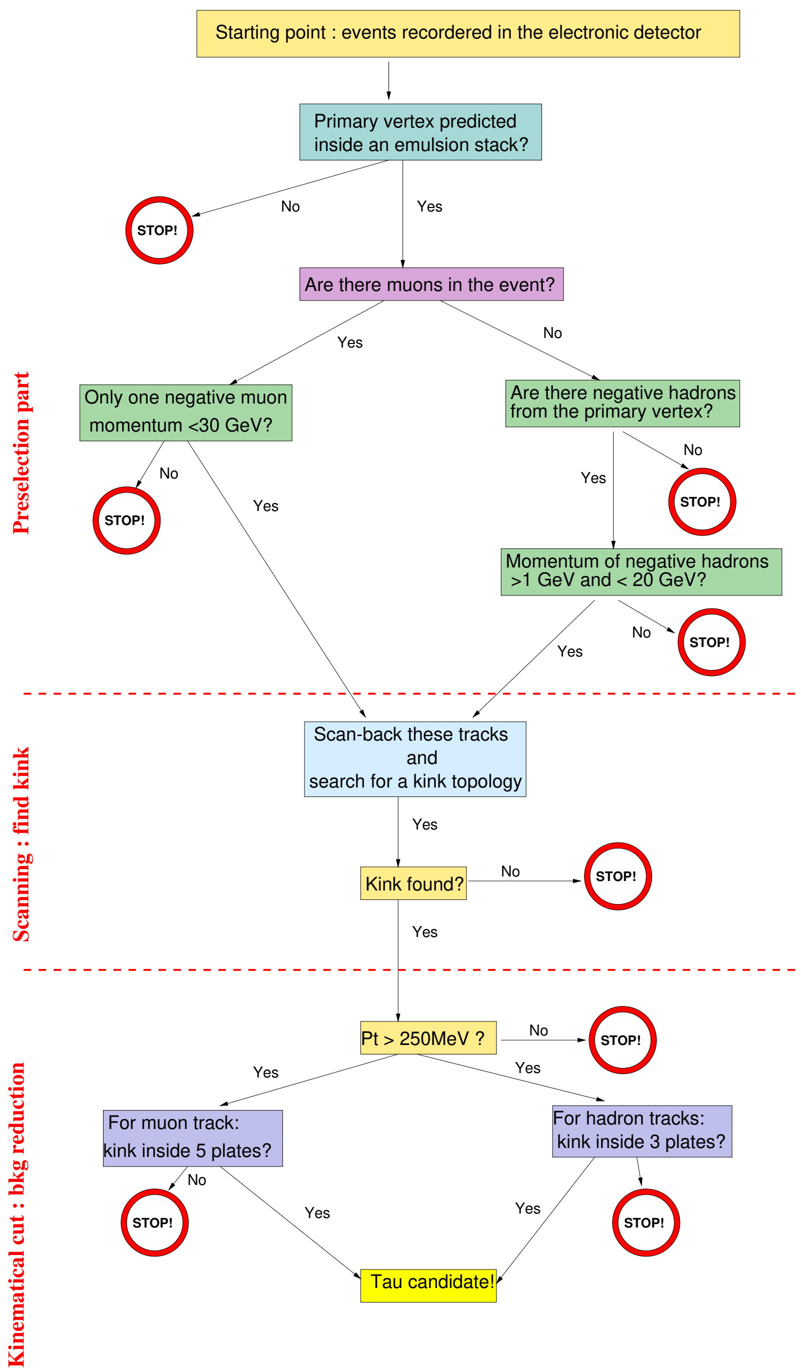

Figure 3.3: Schematic view of the analysis flow

triggered are interactions with the material around the emulsion stack). All the events for which the primary vertex is not reconstructed inside one emulsion stack are rejected.

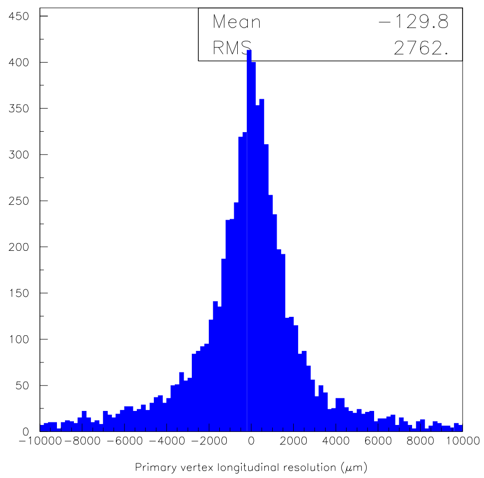

Figure 3.4: Scintillating fiber tracker reconstruction algorithm resolution of longitudinal primary vertex position.

Further cuts are applied to keep only events that contain at least one negative track compatible with being the decay product of a τ. To apply these selections only reconstructed tracks from primary vertex are taken into account. In fact τ decay products appear as outgoing from the primary vertex due to resolution. The vertex resolution is too rough to permit to separate the ν_τ primary vertex from the τ 1-prong decay vertex: the impact parameter of the τ daughter with respect to the primary vertex is more than one order of magnitude smaller than the transverse vertex position resolution (fig 3.5).

The events with a reconstructed negative track from primary vertex are divided in two orthogonal samples according to the different decay modes used to detect the τ. The first sample (1μ) consists of all events with only one negative muon and no positive muon; it is supposed to include the events with a τ muonic decay. The second sample (0μ) contains all events that have no muons and at least one track fitted as negatively charged in the hexagonal spectrometer. This selection was designed mainly to collect possible τ hadronic decay. Actually it selects with a non-negligible efficiency also τ electronic decay whenever the electron doesn't shower before reaching the hexagonal magnet.

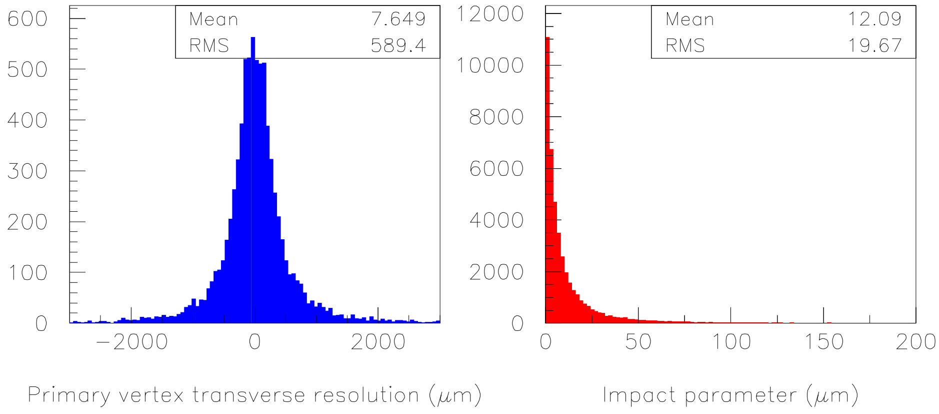

Figure 3.5: **Left:** scintillating fiber tracker reconstruction algorithm resolution of primary vertex position. **Right:** impact parameter between primary vertex and τ decay track

Additional cuts are applied to these samples to reduce the scanning time. For the 1μ sample the momentum of the reconstructed negative muon must lie in the range 0-30 GeV/c. The cut at 30 GeV/c rejects about 30 % of ν_μ CC, while it discards less that 15 % of $\tau^- \to \mu^- \nu_\tau \bar{\nu}_\mu$ decays. In addition at higher energy the *kink* angle is smaller so more difficult to reveal, therefore the effective loss in the detectable number of τ is well below 15 %. For the 0μ sample the momentum of negative tracks must be in the range 1-20 GeV/c. The lower cut reduces the large amount of low energy particles from secondary interactions or γ conversions. The upper cut is dictated by the limited momentum resolution of the air-core magnet at higher energy.

3.2.2 Scanning

All the events survived the preselection chain are analysed in emulsion. The first part of the scanning is fully automated and it is supposed to check whether the predicted event was really originated inside the emulsion (vertex location) and to select τ candidates with higher rejection power than the one achievable by electronic preselection (kink signature search). The second part, the longest one, consists in the manual check of the possible kink. The automatic part uses the TRACK SELECTOR (see previous chapter) to perform track finding: there only a fraction of the emulsion plate depth is analysed. Conversely in the manual part all the emulsion volume is inspected.

Vertex localization

All the selected negative tracks, assumed to be the τ daughter (*scan-back tracks*), are searched in the first emulsion interface-sheet (Changeable Sheet) using the track parameters measured by the scintillating fiber trackers. If they are confirmed, using the new track parameters measured in the CS, they are searched on the second emulsion interface sheet (Special Sheet). A track which is found in both interface emulsion sheets is then followed upstream in the target emulsion stack plate by plate. In each plate only the most upstream side is scanned searching a track using the SS predicted slope. Whenever a track is confirmed in a plate it is searched in the upstream plate. If the track is found in all 36 bulk plates then the event is rejected because the ν vertex position is probably located in the scintillating fiber planes upstream to the emulsion stack. On the contrary when a track disappears in two consecutive plates the vertex plate is defined as the most downstream of the two (fig 3.6). In case of ν_μ events this plate should

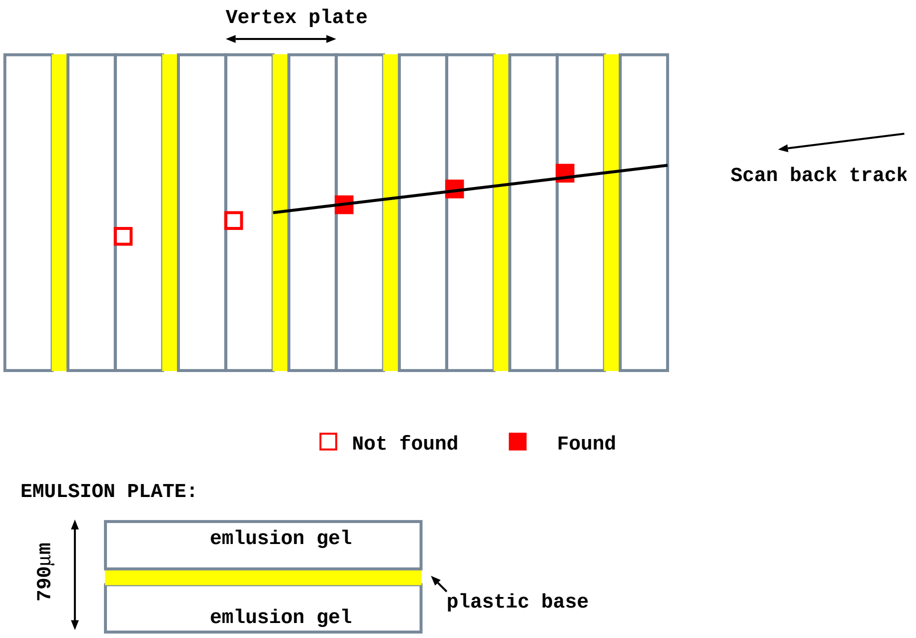

Figure 3.6: Vertex localization procedure. The scan-back track is searched backward to neutrino direction plate by plate. The first plate where it disappear is defined the vertex plate.

contain the interaction vertex, whereas for ν_τ events it could contain the ν_τ vertex or the τ decay vertex respectively if the kink angle is smaller or larger than the plate by plate angular matching tolerance. The three most downstream plates of each stack are used to validate the matching between the fiber prediction and the interface emulsion sheets. Therefore, whenever the vertex plate is one of these three, the localization procedure is not enough reliable and the corresponding event is excluded by the next steps of the analysis.

Kink signature search

Once the vertex plate is defined, automatic microscope measurements are performed to select the events potentially containing a *kink* decay topology. Different algorithms have been applied during the last 6 years as a result of the progress in the scanning procedures.

• A fraction of $\sim$ 10% for the 1μ sample, corresponding to the almost all 1994 data, were analysed with a technique that is able to detect both short and long τ decays; i.e. when the kink point is in the same emulsion plate of the ν_τ vertex or in a downstream one. The technique consists in scanning a region in the plate immediately downstream of the vertex plate searching for all the tracks reconstructed by the fiber tracker as originating from the primary vertex. The width of the region is large enough to contain all the tracks in the assumption that the vertex plate contains the neutrino interaction point. This is true for all ν_μ located events while it is true only for about 30% of the ν_τ events. If during the scanning no tracks, apart from the scan-back one, are confirmed then digital images of the vertex plate are recorded. Subsequently an off-line software processes the images to search for a kink (fig 3.7 b), if it detects a kink signature the event is manually scanned. The signal events that should be selected with this procedure are all long decays with kink angle larger than the plate by plate angular matching tolerance and all quasi-elastic events. In case the search for fiber tracks in emulsion gives positive results two different tests are tried to select events for manual analysis. The first criterion is the change in the scan-back track direction between the vertex plate and the exit from the emulsions: if it corresponds to an apparent transverse momentum, P_t, larger than 250 MeV (fig 3.7 c) the event is selected. A second criterion is the detection of a significant minimum distance between the scan-back track and any other predicted track (fig 3.7 a). In the latter case the event is not directly sent to the eye-scan. In fact to reduce the manual scanning load the video images are taken and only if the image analysis confirms the kink the event is manually analysed. The signal topologies that should be selected by the last two filters are long decays with small kink angle (the vertex plate contains the ν_τ interaction) and short decays.

• The main part of 1μ and all 0μ events have been analysed with the *parent track search* (fig. 3.8). This technique has been developed for the search of τ decay with large angle kinks and long flight path: i.e. the vertex plate contains the τ decay point. The upstream part of the vertex plate is scanned and all the tracks in a cone around the *scan-back track* are collected. The tangent of the opening angle of the cone is 1/P(GeV/c), which guarantees that all decays with the reconstructed value of P_t, transverse momentum with respect to the decay particle direction, less than 1 GeV/c will be detected. The value of the maximum P_t is larger than the maximum τ decay P_t ($M_\tau/2$) to account for the momentum resolution. All tracks collected inside the cone are tested as possible τ candidates using the distance with respect to the *scan-back track*. If the minimal distance between a track and the *scan-back track* is less that 9 μm this track will be considered as the "parent" candidate. Checks are made to ensure that the parent track candidate is not a passing-through track accidentally associated to the *scan-back track*.

A similar algorithm is applied to the search for large *kink* with interaction vertex and decay vertex in the opposite sides of the same emulsion plate. In this case the downstream emulsion layer of the vertex plate is assumed to contain the decay point. The upstream part of this layer is scanned searching for a track that has a minimal distance less than 6 μm with the *scan-back track*.

In addition to the parent track search a revised version of the impact parameter technique used for the short decay search on 94 data 1μ (fig 3.7 a) has been applied to a large fraction of 1μ or 0μ samples. The main difference is that, since in the last years of the automatic scanning the angular resolution has improved, the impact parameter criterion is strong enough to reject a large fraction of ν_μ events without the need of the video image test.

Kink manual check

All the events selected by the previous described algorithms were scanned by eye to confirm the presence of a secondary vertex and to measure accurately its topology. With the oldest algorithms the events selected for manual check were about 20% of the located ones. The manual scanning load was very heavy, thus the search for alternative methods was developed. The result of this work was the *parent track search*, that with a comparable efficiency has a rejection power 10 times stronger: the fraction of the located events selected by *parent track search* is about 3%.

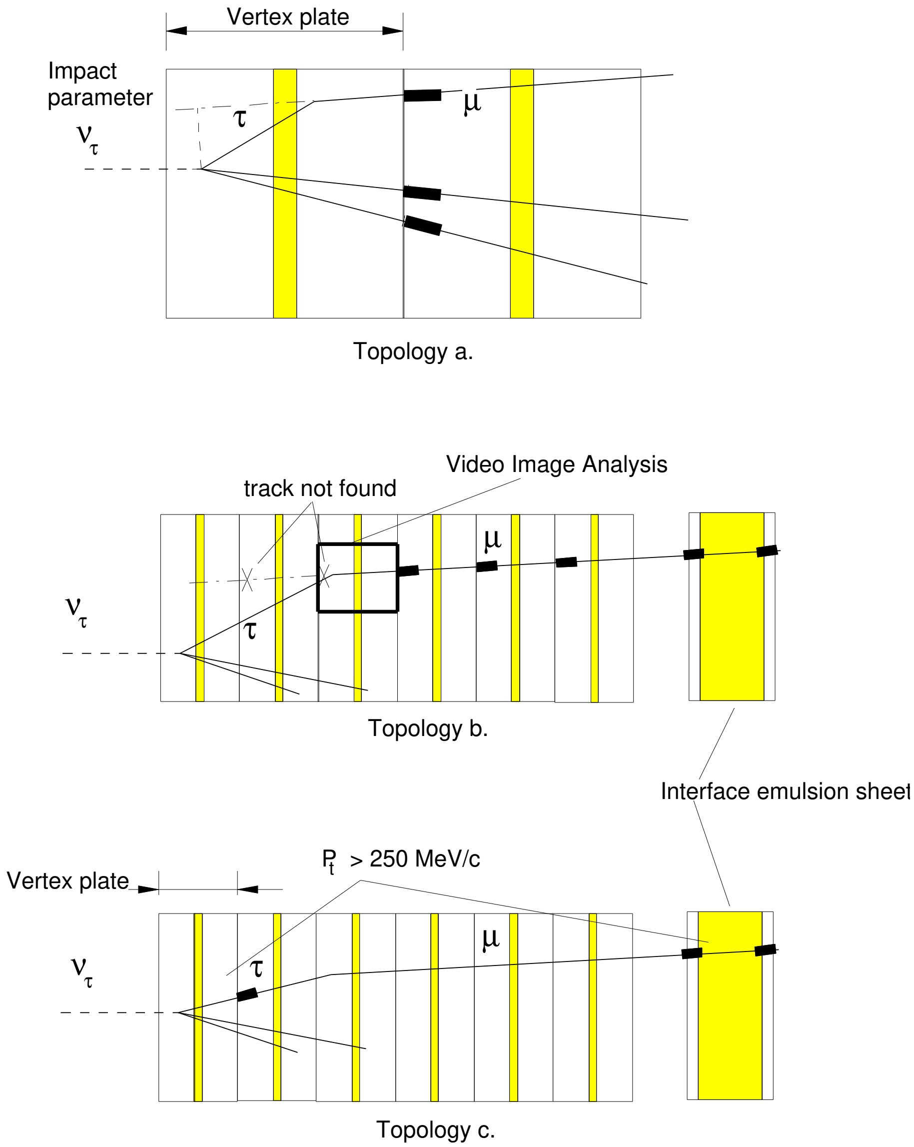

Figure 3.7: Kink search. **Top panel:** impact parameter method. **central panel:** long decay selected for video images analysis **bottom panel:** long decay selected by large deviation of scan back track slope in the vertex plate with respect to the SS measured value.

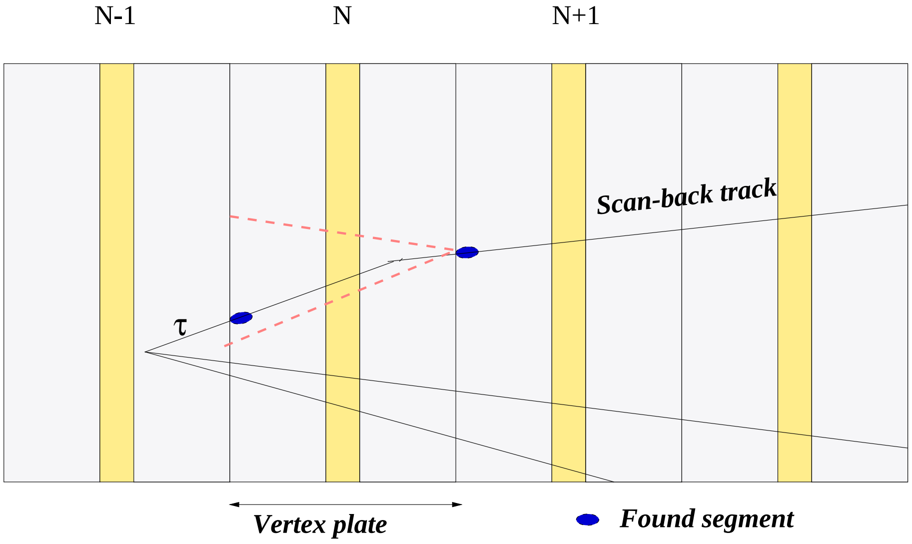

Figure 3.8: Parent track search technique: search of tracks with minimal distance with respect to the scan back track in the most upstream part of the vertex plate.

Even in the high signal to noise *parent track search* selected events the manual scanning confirms the kink in only a few percent of them. The largest part is selected due to an accidental coincidence with a low momentum background track or to the presence of a "backward going" nuclear fragment in the primary interaction vertex. For the events where a kink is really detected, the parent and decay particles, as well as the other tracks coming from the interaction vertex, are accurately measured. The measurements are used for the final topological and kinematic selections designed to reject the residual background.

3.2.3 Post scanning background reduction

The topological signature chosen by CHORUS for ν_τ events is not free from background. The main background sources are decays of short-lived particles other than τ and the elastic interactions of hadrons. The reduction approach used in the CHORUS analysis has been modified during time according to the increased analysed statistics and the expected background events. Let's now just briefly remind the background treatment used in the previous published CHORUS analysis and postpone to a dedicated chapter a careful description of the background evaluation and reduction developed for the analysis described in this thesis.

All the events where the observed kink transverse momentum was less than 250 MeV were discarded to eliminate the pion and kaon decays. Also a cut on the decay length was applied. A maximum value of the distance between the plate containing the neutrino interaction and the plate containing the kink point was set. For hadron scanback tracks it is fixed to 3 plates. The lower background rate for $\tau^- \to \mu^- \nu_\tau \bar{\nu}_\mu$ decay allows longer flight length thus the cut value was moved up from 3 to 5 plates for 1μ events.

Both these background reduction criteria were defined using the 94 scanning technique (fig 3.7). Using that technique both cuts had also the feature to give a powerful reduction of the manual scanning at least for the search of small angle kinks (fig 3.7 c).

3.2.4 Oscillation probability evaluation

At the end of the scanning we will know the number of observed ν_τ candidates. Combining this number with the number of expected background events, it is possible to determine with a certain level of probability the number of ν_τ events observed, N_τ^{obs}.

To determine the oscillation probability or its upper limit in case of no ν_τ candidates evidence we need to know the number of charged current ν_τ events detectable for a given value of the oscillation probability. It is custom in CHORUS to introduce $\mathrm{N}_{\nu_\tau}^{\max}$, the maximum number of charged current ν_τ events detectable in the case where all ν_μ's oscillate in ν_τ's[4].

$$\mathrm{N}_{\nu_\tau}^{\max} = \sum_i BR(\tau \to i) \iint \phi_\mu(E, L)\, \sigma_\tau^{CC}(E)\, A_{\tau\to i}(E)\, \eta_{\tau\to i}(E)\, dE\, dL \qquad (3.4)$$

where:

- E is the neutrino energy and L is the distance between the neutrino production and the detection point
- i runs over all the three one-prong decay channels considered in the analysis
- $BR(\tau \to i)$ are the corresponding branching ratios
- ϕ_μ is the ν_μ flux
- σ_τ^{CC} is the charged current ν_τ cross section

[4] Of course this is a not-physical assumption due to the spread in energy and production point of the neutrino, but $\mathrm{N}_{\nu_\tau}^{\max}$ is a useful parameter

- $A_{\tau\to i}$ is the "location" efficiency. It takes into account all the efficiencies of the first part of the analysis chain from the reconstruction of the event in the electronic detector till the successful vertex plate localization

- $\eta_{\tau\to i}$ is the "kink" efficiency, it represents the efficiency of the second part of the analysis: after vertex localization till the end, including the background reduction cut application

Therefore the value of the oscillation probability is given by:

$$P(\nu_\mu \to \nu_\tau) = \frac{N_\tau^{obs}}{\mathrm{N}_{\nu_\tau}^{\max}} \tag{3.5}$$

To get rid of the systematic error in the determination of P_{osc} due to the knowledge of the ν_μ flux it is better to rewrite $\mathrm{N}_{\nu_\tau}^{\max}$ as a function of the observed value of ν_μ located events

$$N_{\nu_\mu}^{loc} = \iint \phi_{\nu_\mu}(E,L)(\sigma_\mu^{CC}(E)A_{CC}(E) + \sigma_\mu^{NC}(E)A_{NC}(E))\, dE\, dL \tag{3.6}$$

where

- σ_μ^{CC} and σ_μ^{NC} are the ν_μ cross section for respectively charged current and neutral current processes

- A_{CC} and A_{NC} are the "location" efficiency for ν_μ CC and NC events

Let's note that in equation 3.6 the contribution due to $\overline{\nu}_\mu$, ν_e and $\overline{\nu}_e$ interactions has been neglected. They amount to less than 2% of the located events.

Using $N_{\nu_\mu}^{loc}$, 3.5 can be rewritten as

$$P(\nu_\mu \to \nu_\tau) = \frac{N_\tau^{obs}}{N_{\nu_\mu}^{loc} \times \left[\dfrac{\sum_i \langle \sigma_\tau^{CC} \rangle \langle A_{\tau\to i} \rangle \langle \eta_{\tau\to i} \rangle BR(\tau \to i)}{\langle \sigma_\mu^{CC} \rangle \langle A_{CC} \rangle + \langle \sigma_\mu^{NC} \rangle \langle A_{NC} \rangle} \right]} \tag{3.7}$$

where $\langle\sigma\rangle$, $\langle A\rangle$, $\langle\eta\rangle$ are respectively the flux weighted cross sections, the flux and cross-section weighted location efficiency and the flux, cross-section and location efficiency weighted kink detection efficiency.

Concluding to evaluate the oscillation probability in CHORUS we need to know, besides the number of τ candidate events and the whole statistics of the located ones resulting from the scanning measurements, the location and kink efficiencies for the various channels. They will be estimated in the next chapter. We also need an estimation of the number of background events to combine with the number of observed kink events in order to extract the number of ν_τ events observed at a certain confidence level. This will be shown in chapter 5.

Chapter 4

Evaluation of the analysis efficiency

Computing the $\nu_\mu \to \nu_\tau$ oscillation probability using the CHORUS data requires the knowledge of the efficiencies of the whole scanning chain as shown at the end of the previous chapter. The estimation of these quantities has been achieved by a full simulation of all analysis steps: preselection, scanning and post scanning background reduction.

In this chapter the simulation and the results obtained will be described. Whenever it is possible the simulated events are compared with real data to check the reliability, the limit and the bias of Monte Carlo based estimations.

This chapter has been organized as follows

- sketch of events and detector Monte Carlo simulation
- description of the analysis simulation program
- results of the efficiency calculation
- comparison of the data and Monte Carlo electronic detector response with respect to the critical quantities used in the pre-scanning selection
- evaluation of corrections to the efficiencies in order to take into account the Monte Carlo - Data disagreement in the electronic detector response
- discussion of the reliability of the obtained results although the simplified emulsion simulation and evaluation of necessary correction factors

4.1 Events and detector Monte Carlo simulation

The analysis efficiency are calculated on Monte Carlo samples of ν_μ and ν_τ simulated interactions. The neutrino interactions are simulated employing the two different event generators available inside the CHORUS collaboration. The first one describes the neutrino quasi elastic interactions and produces also events with resonances in the final state with a mass central value up to 2 GeV [18]. The other generator, based on LEPTO-LUND [19], simulates the deep inelastic interactions with invariant hadronic final state mass greater than 2 GeV. Therefore adding the two generators allows to simulate all main neutrino interactions with a negligible double counting in the cross section.

The generated neutrino interactions are passed through a GEANT [20] based simulation of the CHORUS detector of both the electronic part and the emulsion volume. The simulation of the electronic detector, employed to evaluate the efficiency of the preselection part, is rather complete (for a semi-quantitative check see section 4.4). On the contrary the emulsion simulation is less accurate. In fact all the event related particles are followed along their path inside the emulsion volume: their hits at each plate crossing or at secondary interaction points are recorded. The main restraint of this simulation is the lack of the event uncorrelated background and the emulsion distortion. It means that pile-up of hits produced by particles of different events or by cosmic tracks or beam related muons has not been simulated due to technical reasons (CPU time and disk space). To have an idea to simulate the 16 views per 100 μm depths used by the track selector we need to record in the CHORUS emulsion a number of hits of the order of 10^{13}. Despite of the lack of this large background, the results of the simulation, integrated with corrections extracted from data, should equally permit to determine the CHORUS oscillation probability as will be discussed in the last section.

4.2 Analysis simulation program description

Let's now briefly describe how the analysis simulation program is working.

Preselection It uses as input the Monte Carlo events with the primary vertex generated in one of the four emulsion stacks. These events are passed through the CHORUS off-line reconstruction program, CHORAL, to select, using the same criteria as for real data, the events to send to the emulsion analysis. The selection rejects all events with no reconstructed vertices or with the reconstructed primary vertex outside the emulsion stacks. Further the events are divided in the two orthogonal sets 1μ or 0μ. The negative muon with momentum less than 30 GeV for 1μ or all the negative hadrons with momentum in the range 1 to 20 GeV for 0μ events are kept as possible scan-back tracks. They are further filtered retaining for the emulsion scanning only those with angles in both y and z direction less that 400 mrad. For each scan-back track the prediction in terms of slope and position on the first interface sheet (CS) are produced.

Track selector simulation The next step of the analysis simulation is the emulsion scanning. In the real scanning the track segment search is performed by the TRACK SELECTOR (TS) (see section 2.3). A complete simulation of its functioning is not imperative for the purpose of the efficiency calculation. In fact its response to the different inputs can easily be extracted and parameterized using the scanning data themselves. A measurement of TS efficiency has been done manually scanning a sample of localized events and it turns out to be very large, of the order of 98% for tracks spanning all the 100 μm emulsion depth used by the TS. The complementary 2% value automatically includes not only the TS proper inefficiency but also the loss of efficiency due to stains on the surface of the sheets. Moreover it has been measured that the TS efficiency depends very slowly on the track angle at least for all angles below 0.4 rad which is the maximum allowed value for the scan back track (fig 4.1). For tracks not spanning all upstream 100

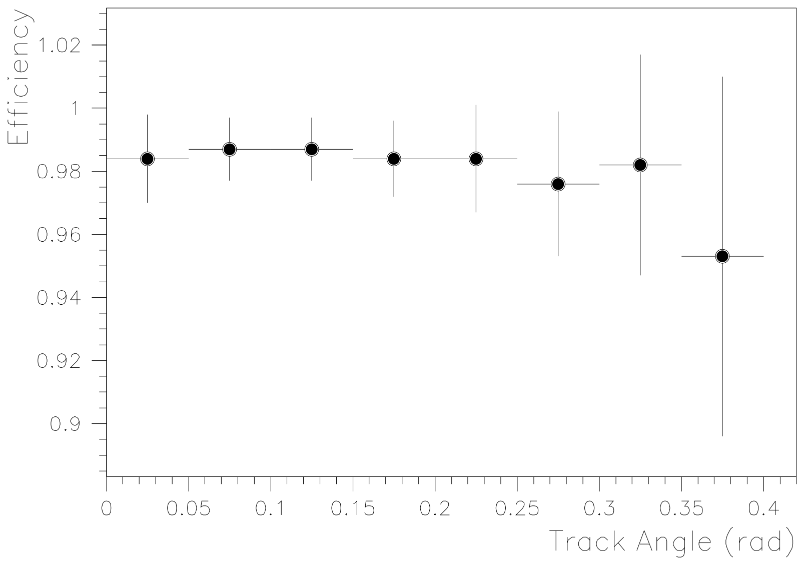

Figure 4.1: Track selector efficiency in plate by plate follow-up

μm depth of the emulsion the efficiency is lower. It has been estimated that for tracks not originating from a charged particle decay or re-interaction the minimum detectable path is about 70 μm. For the complementary set the minimum path is 80 μm[5] [21].

[5]The last value, due to different TS pulse height cut, is decreased to 60 μm for the scanning in the downstream side of a bulk plate

The TS angular and position resolutions folded in with the emulsion shrinkage and internal alignment can be derived from data distributions. The two interface sheets, since they are constructively identical, have the same resolution. Therefore the results of the SS scanning, which is driven by the CS measured slope and position, permits to estimate an angular resolution of 2.7 $mrad$ per projection (fig 4.2). In the same way the position resolution, unfolding the slope resolution, results to be $\simeq 2-3\ \mu m$ (fig 4.2)

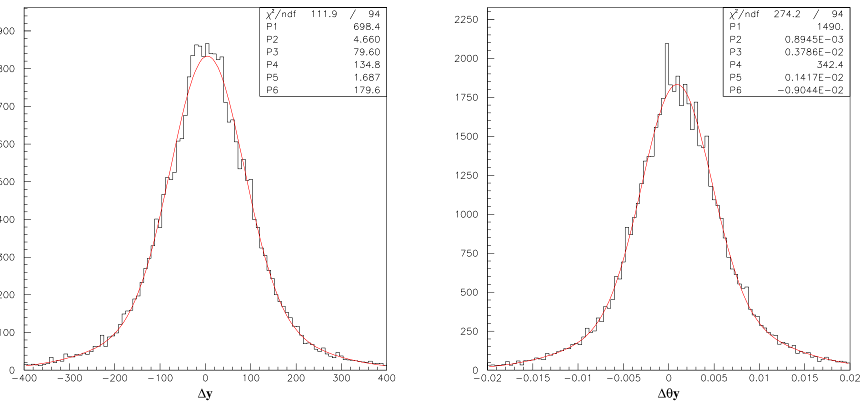

Figure 4.2: **Left panel:** position difference between prediction and candidate on SS. **Right panel:** angular difference in CS - SS matching

Analogously the resolution in the bulk plate can be estimated to be $\simeq 3-4\ \mu m$ and $\simeq 5\ mrad$ respectively for position and slope (fig 4.3).

Scanning simulation The TS, simulated according to the previous description, has been used to reproduce the scanning chain in the way explained below. All the scan-back tracks extrapolated at the CS plane are filtered. If their coordinates are inside the fiducial area they are searched in emulsion (every emulsion sheet is divided in eight modules of $0.71 \times 0.36 m^2$, one centimeter along the border is rejected due to mechanical problem, all the remaining area is considered fiducial area). A rectangular area of 1320 $\mu m \times$ 1020 μm centered around the predicted position is inspected. Every segment with an angular distance with respect to the predicted value less than 15 mrad in both projections is considered as a candidate. In case of multiple candidates a loose cut on the goodness ($\chi^2/ndof < 3.5$) of the match between prediction and candidate is applied to retain only the ones below the cut. For each candidate the CS slope and position measurements are

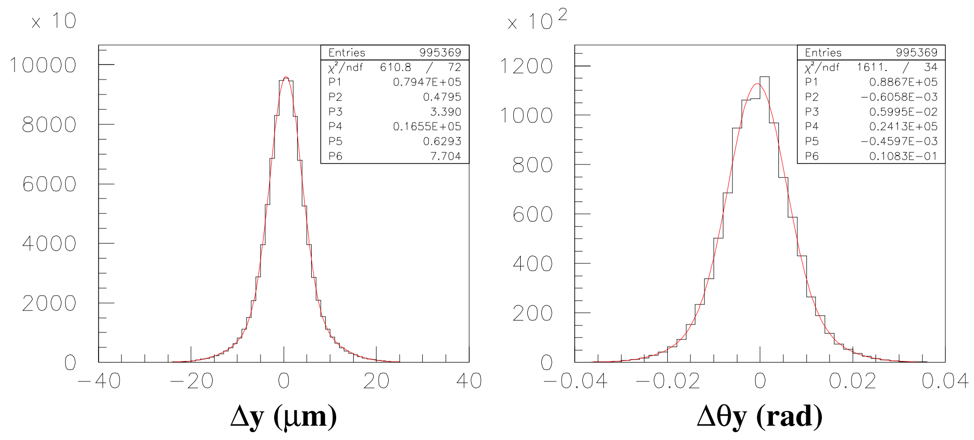

Figure 4.3: Track selector resolution in bulk scanning. **Left panel:** residual in position, **right panel:** residual in slope

used to obtain predictions at the SS surface. A candidate is confirmed on SS if a segment with an angular difference less than 15 mrad in each projection and a position difference less than 400 μm (350 μm) on Y (Z) coordinate with respect to the CS-based prediction is found. Also in the SS scanning, as in the CS, if multiple segments satisfy the matching condition, a rejection on the base of the χ^2 is applied. A track found on CS and SS is then followed-up in the bulk. In case of multiple surviving candidates on SS, all of them are searched for in bulk. The bulk scan consists in the track follow-up plate by plate using as prediction the slope measured in SS and the position measured in the previous plate (or in SS for scanning of plate 36)[6]. A track is confirmed in a plate if a segment that satisfies the following relations with respect to the predicted slope and position

$$\Delta\theta \leq (25 + 50 \cdot \Delta\theta_{X7})\ mrad \tag{4.1}$$

$$\Delta r \leq (15 + 50 \cdot \Delta\theta_{X7})\ \mu m \tag{4.2}$$

exists. $\Delta\theta_{X7}$ is the three dimensional angle between the track and the X7 direction (see last section). The $\Delta\theta_{X7}$ dependent cut has the aim to reduce the background due to the X7 beam. After the track disappears in two consecutive plates the follow-up stops and the vertex plate is defined (fig 3.6). In case the vertex plate

[6]The bulk plate are numbered so that the most upstream is number one and the most downstream is number 36

is one of the three most downstream (34-36) the event analysis is stopped and it is not considered as located. For vertex plate number smaller than 34 the event is considered as located and the kink search is performed using three different methods.

Parent Track Search (PTS): to detect long and large decays (LL).
Assume that the vertex plate is number n, than the 100 μm most upstream of plate n are analysed (see fig 3.8). The scanned region is the part of the plate surface intercepted by a cone having the vertex at the boundary between plate n and plate n+1, and opening angle 1/P around the scan back track direction. The scan back track distance with all segments found in this region is evaluated. Every segment for which the distance is less than 9 μm is further searched in plate n+1. Whenever its existence, using conditions 4.1 and 4.2, is not confirmed also in plate n+1, the event is further analyzed by a simulation of the manual scan.

If the kink is not found by the parent track search a sightly modified version is applied to search for kink where the primary vertex is on the upstream half and the decay on the downstream half of the same plate (Large Half plate Long: LHL). The difference of LHL with respect to LL is that the inspected region for the parent search is the most upstream part of the downstream side of the plate n. The maximum accepted distance between the scan back track and the segment found in the region is 6 μm. If a parent candidate is found the criteria to reproduce the manual scanning simulation are applied.

Short vertex scan back (SVSB): to detect short decays.
When also the last method fails to detect a kink, the SVSB method is applied. This method requires that the target tracker reconstruction algorithm has found at least other two tracks, except the scan back, coming out of the primary vertex. All these tracks are searched on the surface of plate n+1 with the angle predicted by the fiber tracker and position compatible with the assumption that they originate from a vertex lying inside the plate. If more than one track is confirmed in emulsion, the approximate vertex position is calculated minimizing the function

$$V^2 = \sum_i w_i \cdot ((X_0 - X_i)^2 + (Y_0 - Y_i)^2 + (Z_0 - Z_i)^2) \tag{4.3}$$

where the index runs over all the confirmed tracks including the scan back one, the weight w_i is defined as

$$w_i = \sum_{i \neq j} \frac{1}{d_{ij}^2} \tag{4.4}$$

and d_{ij} is the distance in space between track i and j, and X_i,Y_i Z_i are the coordinates of the track i at the surface of plate n. In case of ν_τ events, since all tracks, except the scan back one, exit from the primary vertex, they have a very small distance with each other, thus a large weight in 4.3. The τ decay instead has a non negligible impact parameter with respect to all the other tracks. Therefore it contributes little to the vertex determination function (4.3), assuring that the minimization gives a reasonable vertex point. Let's call dX the longitudinal position of the vertex with respect to the surface of the n+1 plate. If dX is smaller than the plate thickness, i.e. the vertex lies in plate n, for each track the impact parameter (I.P.) with respect to it is calculated. When the scan back track has I.P. $> (4 + 0.012 * dX)$ μm and all the other tracks have I.P. $< (3 + 0.009 * dX)$ μm the event is selected for manual scan.

Manual scan simulation

Whenever one of the previous kink search methods detect a possible kink signature, the event undergoes to a manual scanning simulation. It intends only to test whether the scan back track was really the τ decay daughter and whether the kink is detectable. In fact, although it is reasonable to assume that the manual scan efficiency to find a track is 100%, the kink detection efficiency is lower. It has been experimentally estimated that a kink with angle less that $0.1 \cdot \theta$, where θ is the scan back track angle, is not detectable. The manually measured value of the kink angle has been calculated assuming a gaussian resolution of 3 mrad for the track slope. Moreover the decay path must be longer than 20 μm to be revealed and the kink point cannot be closer than 20 μm to the surface of the plate.

The only post scanning background reduction criteria applied in the analysis simulation are the cut on the maximum allowed decay τ length (3 plates for 0μ and 5 for 1μ) and the $\mathrm{P_t}$ cut. The $\mathrm{P_t}$ is evaluated using the reconstructed momentum of the scan back track and the kink angle value determined in the manual scanning simulation.

4.3 Efficiency evaluation results

In the following tables detailed results of the efficiency evaluation are reported. For each sample of neutrino (ν_μ or ν_τ) interactions that contribute to the oscillation probability calculation, a separate table is produced. Moreover in case an interaction type can be classified both as 1μ or 0μ the corresponding efficiency are reported in two separated tables. This happens for instance for the ν_μ CC interactions that are mainly reconstructed as 1μ, but have a non negligible chance to be defined as 0μ. Every table shows separate efficiency values for deep inelastic reaction (DIS) and for quasi-elastic and resonance production denoted for simplicity as QE.

Let's now discuss briefly the results starting with the vertex finding efficiency. The CC ν_μ (tab 4.1 and 4.3) interactions have a quite larger vertex reconstruction efficiency and resolution with respect to the NC ν_μ (tab 4.2) mainly due to their higher charged track multiplicity. The slight difference between $\tau^- \rightarrow \mu^-\nu_\tau\bar{\nu}_\mu$ (tab 4.4) and $\tau^- \rightarrow \mathrm{h}^-(n\pi^0)\nu_\tau$ (tab 4.5) is due to the fact that in the first set there is an isolated track, the muon, that besides the primary vertex tracks, can be used to identify the vertex. Instead for $\tau^- \rightarrow \mathrm{h}^-(n\pi^0)\nu_\tau$ the π^0 shower sometimes hides the π^- track and always complicates the track finding in the scintillating fiber tracker.

The efficiency values of CC ν_μ events and $\tau^- \rightarrow \mu^-\nu_\tau\bar{\nu}_\mu$ events to be correctly identified as 1μ events are diverse due different momentum spectra. In fact the muons from τ are less energetic because of the three body decay, therefore they are less efficiently reconstructed in the calorimeter and the spectrometer.

The CS confirmation efficiency is larger for all 1μ events just as a consequence of the fact that the muon tagged track are more robust than the hadron flagged tracks. After the "cleaning" effect of the CS validity, both muon and hadron flagged tracks have the same efficiency to be found on SS.

Let's now examine the kink efficiency break-down. The different fractions of short and long kink reported in tables 4.4, 4.5, 4.6 and 4.7 are just an effect of the different flight length in terms of plates permitted for the 1μ and 0μ samples. The LL and LHL search efficiencies indicate the apparent method efficiency. They are the kink signature detection efficiency of each algorithms normalized to, respectively, the long and the short fractions of the events. They are roughly a factor two larger for τ decays falling into the 1μ set that for ones categorized as 0μ. This is just a consequence of the fact that the apparent efficiency is the product of the intrinsic method efficiency times the probability of the scan back track to be the τ decay daughter which is larger for 1μ than for 0μ. In fact a bulk confirmed, thus existing, track with an hadronic tag could be originated not only in the τ decay but also in the primary vertex. On the contrary the muon tagged track always points at the τ decay point.

The $\mathrm{P_t}$ distributions for $\tau^- \rightarrow \mu^-\nu_\tau\bar{\nu}_\mu$ and $\tau^- \rightarrow \mathrm{h}^-(n\pi^0)\nu_\tau$ decays are different. In particular the muonic decay has an higher average value for the $\mathrm{P_t}$.

It explains why the efficiency of the $\mathrm{P_t}$ cut is larger for $\tau^- \rightarrow \mu^- \nu_\tau \bar{\nu}_\mu$ than for $\tau^- \rightarrow \mathrm{h}^-(n\pi^0)\nu_\tau$.

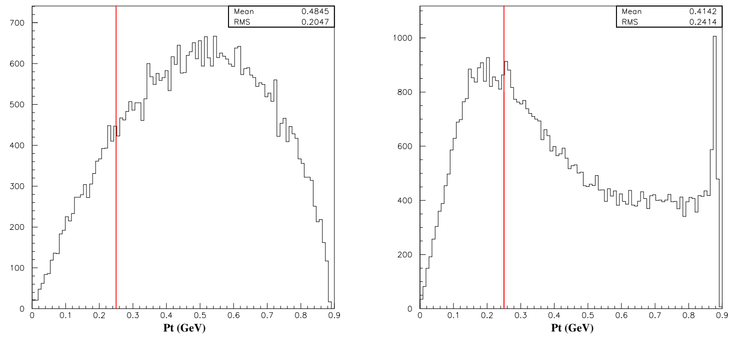

Figure 4.4: True $\mathrm{P_t}$ Monte Carlo distribution. The red line represents the 250 MeV value. **Left panel:** $\tau^- \rightarrow \mu^- \nu_\tau \bar{\nu}_\mu$ decays; **right panel:** $\tau^- \rightarrow \mathrm{h}^-(n\pi^0)\nu_\tau$ decays

		DIS	QE
Events generated inside emulsion		45152.	5363.
Triggered events	(%)	99.61± 0.03	99.53± 0.12
Vertex inside emulsion	(%)	96.09± 0.09	97.82± 0.20
Vertex in the right stack	(%)	99.68± 0.03	99.87± 0.05
1μ category	(%)	87.12± 0.16	97.19± 0.23
At least one scan back track	(%)	71.00± 0.23	82.21± 0.54
Found on CS	(%)	93.51± 0.15	97.61± 0.24
Found on SS	(%)	92.86± 0.16	93.42± 0.39
Found in bulk plates 4-36	(%)	91.32± 0.19	91.56± 0.45
$\mathbf{A_{CC}^{1\mu}}$	(%)	$\mathbf{46.80 \pm 0.34}$	$\mathbf{64.84 \pm 0.81}$

Table 4.1: Location efficiency for ν_μ CC events classified as 1μ

4.4 A check of Monte Carlo and data agreement

The largest part of the location efficiency depends on the reconstruction capability of the electronic detector. Therefore it is natural to test the reliability of its simulation. It has been studied comparing the real data with a Monte Carlo sample that includes ν_μ, $\overline{\nu}_\mu$ and ν_e simulated interactions. The different neutrino flavors are mixed according to the spectra and average energies (tab 4.8) obtained

		DIS	QE
Events generated inside emulsion		27689.	6719.
Triggered events	(%)	90.50± 0.18	21.30 ± 0.50
Vertex inside emulsion	(%)	73.72± 0.28	16.51 ± 0.98
Vertex in the right stack	(%)	95.44± 0.15	82.0 ± 2.5
0μ category	(%)	96.95± 0.13	98.68 ± 0.82
At least one scan back track	(%)	49.74± 0.38	8.8 ± 2.1
Found on CS	(%)	83.62± 0.40	86.1 ± 8.4
Found on SS	(%)	92.79± 0.31	88.2 ± 8.5
Found in bulk plates 4-36	(%)	89.17± 0.38	88.3 ± 8.9
$\mathbf{A_{NC}}$	(%)	$\mathbf{21.24 \pm 0.55}$	$\mathbf{0.18^{+0.06}_{-0.05}}$

Table 4.2: Location efficiency for ν_μ NC events

		DIS	QE
Events generated inside emulsion		45152.	5363.
Triggered events	(%)	99.61± 0.03	99.53± 0.12
Vertex inside emulsion	(%)	96.09± 0.09	97.82± 0.20
Vertex in the right stack	(%)	99.68± 0.03	99.87± 0.05
0μ category	(%)	10.70± 0.15	2.60± 0.22
At least one scan back track	(%)	54.18± 0.73	23.5± 3.6
Found on CS	(%)	83.77± 0.74	$100.^{+0.00}_{-3.1}$
Found on SS	(%)	93.29± 0.55	93.7± 4.3
Found in bulk plates 4-36	(%)	90.51± 0.66	96.7± 3.3
$\mathbf{A^{0\mu}_{CC}}$	(%)	$\mathbf{3.91 \pm 0.46}$	$\mathbf{0.54^{+1.1}_{-0.09}}$

Table 4.3: Location efficiency for ν_μ CC events classified as 0μ

		DIS	QE
Events generated inside emulsion		43640.	5502.
Triggered events	(%)	99.30± 0.04	92.50± 0.36
Vertex inside emulsion	(%)	95.30± 0.10	96.18± 0.27
Vertex in the right stack	(%)	99.47± 0.04	99.53± 0.10
1μ category	(%)	79.03± 0.20	85.48± 0.50
At least one scan back track	(%)	83.22± 0.21	89.94± 0.47
Found on CS	(%)	90.38± 0.18	97.11± 0.27
Found on SS	(%)	88.57± 0.20	90.13± 0.49
Found in bulk plates 4-36	(%)	91.38± 0.19	90.43± 0.51
$\mathbf{A^{1\mu}_{\tau^- \to \mu^- \nu_\tau \bar{\nu}_\mu}}$	(%)	$\mathbf{45.28 \pm 0.35}$	$\mathbf{53.88 \pm 0.91}$
Fraction of short kink	(%)	30.45± 0.48	37.6± 1.2
Fraction of long kink	(%)	63.49± 0.51	59.0± 1.2
Fraction of too long kink	(%)	6.06± 0.25	3.41± 0.44
LHL search efficiency	(%)	15.00± 0.68	19.1± 1.5
$\mathrm{P_t}$ cut efficiency for LHL found kinks	(%)	95.87± 0.98	96.4± 1.7
LL search efficiency	(%)	47.68± 0.66	61.7± 1.5
$\mathrm{P_t}$ cut efficiency for LL found kinks	(%)	95.98± 0.38	94.78± 0.89
Contribution of LL to η_{kink}	(%)	29.06± 0.48	34.5± 1.1
Contribution of LHL to η_{kink}	(%)	4.38± 0.22	6.92± 0.61
Contribution of SVSB to η_{kink}	(%)	3.94± 0.20	-
$\eta^{\mathbf{1\mu}}_{\tau^- \to \mu^- \nu_\tau \bar{\nu}_\mu}$	(%)	$\mathbf{37.38 \pm 0.51}$	$\mathbf{41.4 \pm 1.2}$

Table 4.4: Location efficiency for $\tau^- \to \mu^- \nu_\tau \bar{\nu}_\mu$ events classified as 1μ

		DIS	QE
Events generated inside emulsion		41738.	1329.
Triggered events	(%)	99.70± 0.03	95.70± 0.56
Vertex inside emulsion	(%)	89.98± 0.15	75.5± 1.2
Vertex in the right stack	(%)	97.75± 0.08	92.93± 0.83
0μ category	(%)	96.16± 0.10	98.07± 0.46
At least one scan back track	(%)	68.58± 0.25	56.0± 1.7
Found on CS	(%)	82.87± 0.24	89.6± 1.4
Found on SS	(%)	91.55± 0.20	88.0± 1.5
Found in bulk plates 4-36	(%)	89.12± 0.23	89.4± 1.6
$\mathbf{A}_{\tau^-\to\mathrm{h}^-(\mathbf{n}\pi^\mathbf{0})\nu_\tau}$	(%)	$\mathbf{39.10 \pm 0.38}$	$\mathbf{26.0 \pm 2.4}$
Fraction of short kink	(%)	30.16± 0.57	36.4± 5.0
Fraction of long kink	(%)	54.05± 0.62	54.1± 5.1
Fraction of too long kink	(%)	15.80± 0.46	9.5± 3.0
LHL search efficiency	(%)	8.59± 0.64	18.1± 6.6
$\mathrm{P_t}$ cut efficiency for LHL found kinks	(%)	83.3± 2.9	83±15
LL search efficiency	(%)	30.57± 0.78	59.8± 6.9
$\mathrm{P_t}$ cut efficiency for LL found kinks	(%)	80.8± 1.2	86.7± 6.2
Contribution of LL to η_{kink}	(%)	13.34± 0.43	28.1± 4.6
Contribution of LHL to η_{kink}	(%)	2.16± 0.18	5.4± 2.3
Contribution of SVSB to η_{kink}	(%)	2.87± 0.21	-
$\eta_{\tau^-\to\mathrm{h}^-(\mathbf{n}\pi^\mathbf{0})\nu_\tau}$	(%)	$\mathbf{18.37 \pm 0.48}$	$\mathbf{33.5 \pm 4.9}$

Table 4.5: Location efficiency for $\tau^- \to \mathrm{h}^-(n\pi^0)\nu_\tau$ events

		DIS	QE
Events generated inside emulsion		15223.	486.
Triggered events	(%)	99.50± 0.06	95.20± 0.06
Vertex inside emulsion	(%)	88.06± 0.26	71.4± 2.1
Vertex in the right stack	(%)	97.13± 0.14	89.3± 1.7
0μ category	(%)	97.75± 0.13	$100.00^{+0.00}_{-0.34}$
At least one scan back track	(%)	58.78± 0.44	40.3± 2.9
Found on CS	(%)	79.01± 0.47	77.6± 3.8
Found on SS	(%)	90.95± 0.37	88.7± 3.3
Found in bulk plates 4-36	(%)	88.60± 0.43	87.2± 3.7
$\mathbf{A}_{\tau^- \to \mathbf{e}^- \nu_\tau \bar{\nu}_\mathbf{e}}$	(%)	$\mathbf{31.13 \pm 0.67}$	$\mathbf{14.7 \pm 4.3}$
Fraction of short kink	(%)	29.5± 1.2	22±12
Fraction of long kink	(%)	53.5± 1.3	64±14
Fraction of too long kink	(%)	17.00± 0.98	14±11
LHL search efficiency	(%)	6.3± 1.2	33±30
$\mathrm{P_t}$ cut efficiency for LHL found kinks	(%)	57.3± 9.5	$0.^{+17}_{-0}$
LL search efficiency	(%)	21.1± 1.5	75±16
$\mathrm{P_t}$ cut efficiency for LL found kinks	(%)	50.0± 3.9	36±21
Contribution of LL to η_{kink}	(%)	5.64± 0.60	17±11
Contribution of LHL to η_{kink}	(%)	1.06± 0.27	$0.^{+17}_{-0}$
Contribution of SVSB to η_{kink}	(%)	0.90± 0.25	-
$\eta_{\tau^- \to \mathbf{e}^- \nu_\tau \bar{\nu}_\mathbf{e}}$	(%)	$\mathbf{7.60 \pm 0.69}$	$\mathbf{17 \pm 5}$

Table 4.6: Location efficiency for $\tau^- \to e^- \nu_\tau \bar{\nu}_e$ events

		DIS	QE
Events generated inside emulsion		43640.	5502.
Triggered events	(%)	99.30± 0.04	92.50± 0.36
Vertex inside emulsion	(%)	95.30± 0.10	96.18± 0.27
Vertex in the right stack	(%)	99.47± 0.04	99.53± 0.10
0μ category	(%)	17.90± 0.19	14.03± 0.50
At least one scan back track	(%)	57.02± 0.58	19.8± 1.5
Found on CS	(%)	83.49± 0.57	93.8± 2.1
Found on SS	(%)	92.65± 0.44	90.5± 2.6
Found in bulk plates 4-36	(%)	89.80± 0.53	87.1± 3.1
$\mathbf{A}^{\mathbf{0}\mu}_{\tau^- \to \mu^- \nu_\tau \bar{\nu}_\mu}$	(%)	$\mathbf{6.67 \pm 0.46}$	$\mathbf{1.8 \pm 1.4}$
Fraction of short kink	(%)	44.1± 3.6	47±35
Fraction of long kink	(%)	49.8± 3.6	51±35
Fraction of too long kink	(%)	6.1± 1.7	2.04 ± 1.0
LHL search efficiency	(%)	7.3± 2.8	22^{+7}_{-6}
$\mathrm{P_t}$ cut efficiency for LHL found kinks	(%)	84±15	80^{+9}_{-15}
LL search efficiency	(%)	31.7± 4.7	72±45
$\mathrm{P_t}$ cut efficiency for LL found kinks	(%)	74.8± 7.8	81±47
Contribution of LL to η_{kink}	(%)	11.8± 2.3	30 ± 5
Contribution of LHL to η_{kink}	(%)	2.7± 1.2	8 ± 3
Contribution of SVSB to η_{kink}	(%)	4.5± 1.5	-
$\eta^{\mathbf{0}\mu}_{\tau^- \to \mu^- \nu_\tau \bar{\nu}_\mu}$	(%)	$\mathbf{19.0 \pm 2.8}$	$\mathbf{38 \pm 5}$

Table 4.7: Location efficiency for $\tau^- \to \mu^- \nu_\tau \bar{\nu}_\mu$ events classified as 0μ

from a complete simulation of the beam line [22, 14]. The $\overline{\nu}_{\rm e}$ component has been neglected since it is very small, of the order of 0.2%.

Neutrino flavor	composition	average energy (GeV)
ν_μ	1	26.5
$\overline{\nu}_\mu$	0.058	21.5
ν_e	0.009	39.2

Table 4.8: Neutrino beam composition on CHORUS target

The generated neutrino interactions are passed through the GEANT [20] based simulation of the CHORUS detector and through the same reconstruction program used for real data. The different samples of simulated events obtained are merged with the proportions reported in table 4.9, which have been calculated using the energy dependent cross-section given by [23, 24, 1] plus the trigger efficiency.

Interaction type	$\langle\phi \times \sigma\rangle$	fraction in the sample
ν_μ(CC,DIS)	1.	1.
ν_μ(CC,RES)	0.085	0.085
ν_μ(NC,DIS)	0.311	0.282
ν_μ(NC,RES)	0.032	0.007
$\overline{\nu}_\mu$(CC,DIS)	0.023	0.023
$\overline{\nu}_\mu$(CC,RES)	0.005	0.004
$\overline{\nu}_\mu$(NC,DIS)	0.008	0.007
ν_e(CC,DIS)	0.013	0.012
ν_e(NC,DIS)	0.004	0.004

Table 4.9: Neutrino interaction composition in the MC sample

The mixed Monte Carlo sample consists of roughly 100,000 neutrino events. The data set used for the comparison amounts to more than 100,000 events of 1996 data taking, half of which are reconstructed inside the emulsion target.

Of all the possible tests of reliability of the electronic detector simulation, in the following, the attention will be focused on the main critical quantities upon which the preselection acts: vertex reconstruction, muon and hadron reconstruction efficiency and momentum distribution.

To test whether the behavior of the vertex reconstruction is similar on Monte Carlo and data the more powerful comparisons are the vertex position and the track multiplicity.

The fraction of events in which the neutrino vertex has been reconstructed to be inside an emulsion stack is 0.591 ± 0.004 for data and 0.627 ± 0.004 for Monte Carlo. The discrepancy is not very sizeable and it is largely due to the non complete simulation of all the material around the target region. In fact when we restrict ourselves to the vertex longitudinal position inside the emulsion we obtain a pretty good agreement (fig 4.5).

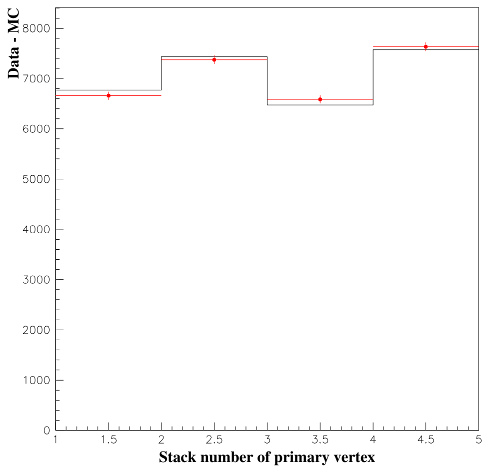

Figure 4.5: Reconstructed primary vertex stack distribution. The histogram depicts the Monte Carlo, the markers correspond to the data.

The track multiplicity from primary vertex (fig 4.6) shows a quite good agreement for the central part of the distribution (about 90% of the statistics) while both tails are larger on data sample. The discrepancy in the first bin (single track primary vertex) is largely due to the lack in the simulated sample of the associated beam muons and of the ν interactions in a capillary test target placed in front of the CHORUS detector. In fact both these neglected components are mostly reconstructed as one track vertices in the first stack. Restricting the analysis to the vertex placed in the last two stacks the discrepancy on the ratio Data/MC for single track vertices is reduced from 1.9 ± 0.3 to 1.5 ± 0.4. Also the scanning result confirms a largest fraction of *passing through*[7] in stack one (25%) with respect to the others stacks (15%). To avoid this bias in the following comparisons only the

[7]The passing through are tracks that, during the scanning, appear to be actually originated upstream of the stack they were supposed to start.

events in which the vertex is predicted in one of the stacks downstream of the first one, are retained. The disagreement on the high multiplicity tail is due to the larger event-correlated noise in real events with respect to the Monte Carlo.

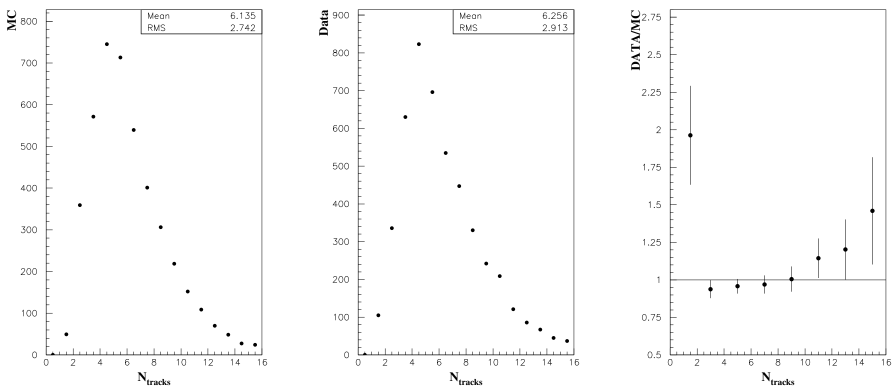

Figure 4.6: Primary vertex tracks multiplicity distribution. **Left:** Monte Carlo **Center:** data **Right:** data-Monte Carlo ratio.

The next variable inspected during the preselection chain is the number of muons outcoming from the primary vertex. A measurement of the agreement of the muon reconstruction efficiency in both samples, is the ratio of events with zero (0μ) or one (1μ) muon outcoming from the vertex:

$$\frac{0\mu}{1\mu}(Data) = 0.436 \pm 0.008 \tag{4.5}$$

$$\frac{0\mu}{1\mu}(MC) = 0.339 \pm 0.007 \tag{4.6}$$

The observed difference can be interpreted as an overestimation of muon reconstruction efficiency, ϵ_μ, in the Monte Carlo events. From the $0\mu/1\mu$ ratio it results

$$\frac{\epsilon_\mu^{DATA}}{\epsilon_\mu^{MC}} = 0.933 \pm 0.008\%. \tag{4.7}$$

An independent measurement of the same quantity is possible using the $2\mu/1\mu$ events ratio: it gives $(89.7 \pm 2.1)\%$ in agreement with the previous estimation.

The observed discrepancy in ϵ_μ between data and Monte Carlo forces us to apply a correction factor on the evaluated efficiency (section 4.3). From the $0\mu/1\mu$ ratio we can only extract an averaged correction factor, is it sufficient? Or is the

Monte Carlo overestimated muon reconstruction efficiency correlated with other variables that affect the A or η_{kink} calculation? Checking all the ingredients of the efficiency calculation, we can convince ourselves that an answer with a reasonable degree of approximation can be derived considering the correlation of ϵ_μ with two variables: momentum and angle of the muon. This correlation study is needed also to evaluate the "correction factor" to apply on ν_τ N $\rightarrow$ τ^- X followed by the muonic decay of the τ.

It is obvious that the muon momentum distribution strongly affects the efficiency calculation due to the upper cut at 30 GeV on the scanned muons. As depicted in figure 4.7 the agreement of the data and simulated events is quite satisfactory: thus ϵ_μ discrepancy results to not have strong correlation with the momentum value.

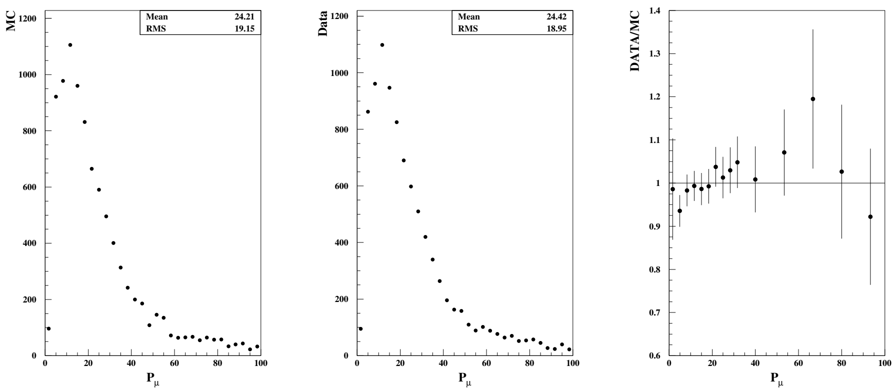

Figure 4.7: Negative muon momentum distribution. **Left:** Monte Carlo **Center:** data **Right:** data-Monte Carlo ratio.

The θ distribution, where θ is the angle of the muon with respect to the beam direction, influences the scanning contribution to the location efficiency due to the strong θ-dependence of the background tracks in emulsion, as it will be discussed in the last section. Unfortunately this distribution, contrarily to the spectra shows a disagreement of data and Monte Carlo: the MC sample exhibits an excess for small θ. Two different explanations can account for this effect: uncertainty in the event generator and a too clean detector simulation. The events for which the discrepancy is observed are characterized by low q^2, where q is the 4-momentum of the W in the neutrino interaction. The generator of DIS events at low q^2 has a sizeable uncertainty because it implies the extrapolation of the nucleon structure

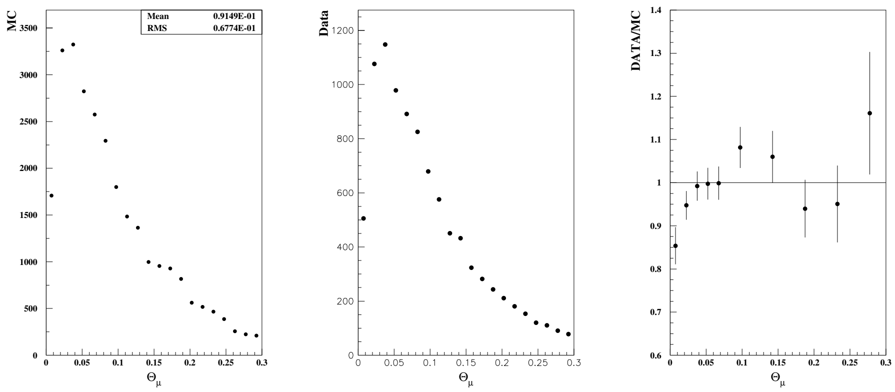

Figure 4.8: Angle distribution of μ^- with respect to the beam direction. **Left:** Monte Carlo. **Center:** data. **Right:** data-Monte Carlo ratio.

functions from high q^2 region, where they are measured, to low q^2 region. Luckily this uncertainty in the DIS generator is not critical for the oscillation analysis. In fact as shown in section 3.2.4 we are sensitive only to the ratio of the location efficiencies. The ratio of the efficiencies of ν_τ and ν_μ events evaluated using different sets of structure functions changes less than 5%.

The observed discrepancy in the θ distribution can be also partly due to a too clean simulation of the detector response. If this is the correct explanation it means that the Monte Carlo overestimates the muon reconstruction efficiency when the track is very close, or hidden, in the shower. It can be caused by the calorimeter pattern recognition, which works too well on Monte Carlo events. In fact selecting events with large electromagnetic and small hadronic calorimeter activity the discrepancy diminishes sizeable [25]. If there is a θ dependence of ϵ_μ discrepancy its impact on the oscillation analysis is very small. In fact the θ distribution of the muon in ν_μ CC events and ν_τ CC events is very similar as shown in figure 4.9.

The last point in the comparison is the agreement of the quantities used to preselect the events that possibly contain an hadronic tau decay daughter. Since to select we use the knowledge of the momentum given by the air-core spectrometer, it appears reasonable to compare the distribution of the number of tracks per event with a successful momentum fit and of the reconstructed value of the negative momentum. From figure 4.10 and 4.11 it is possible to check that data and Monte Carlo agree quite well on both the distributions.

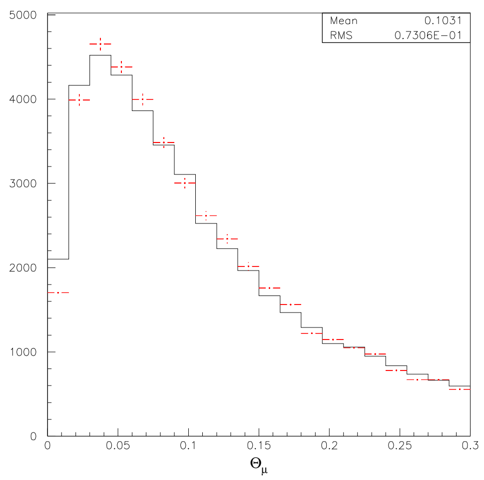

Figure 4.9: Angle distribution with respect to the beam direction of μ^- in CC (histogram) or $\tau^- \to \mu^- \nu_\tau \bar{\nu}_\mu$ (points) simulated events.

An estimation of data and Monte Carlo behavior with respect to the efficiency and resolution of the hexagonal tracker, can be obtained using, as a highly pure reference sample, the muon in neutrino events. The ratio of spectrometer reconstructed muon also fitted in the hexagonal magnet is 0.830 ± 0.013 for data and 0.820 ± 0.014 for Monte Carlo. Therefore the efficiency of the reconstruction and fitting of the hexagonal magnet algorithm seems the same in both samples. On the contrary the resolution ($\Delta p/p$ vs p) shows a clear disagreement (fig 4.12). In particular the fit for the Monte Carlo gives

$$\sigma\left(\frac{\Delta p}{p}\right) = 0.285 \oplus 0.025 \cdot p \tag{4.8}$$

while for real data the resolution is

$$\sigma\left(\frac{\Delta p}{p}\right) = 0.42 \oplus 0.04 \cdot p. \tag{4.9}$$

The data resolution is worse for the combination of two reasons. One is the larger noise in neutrino events with respect to the Monte Carlo, in fact the agreement of Monte Carlo and data on a sample of beam associated muon is pretty good [26]. The other is the alignment procedure of the detector. It is needed for data but not for Monte Carlo events which are simulated assuming a perfectly aligned detector. Therefore it is obvious that the data are “less” precisely aligned with respect to the simulated events.

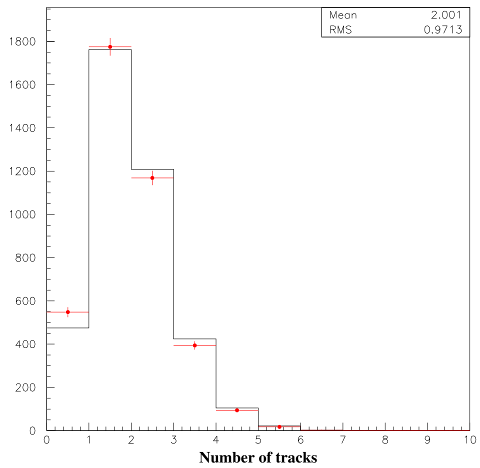

Figure 4.10: Number of tracks per event which have a momentum measured in the air-core magnet. The histogram depicts the Monte Carlo events, the markers correspond to the data.

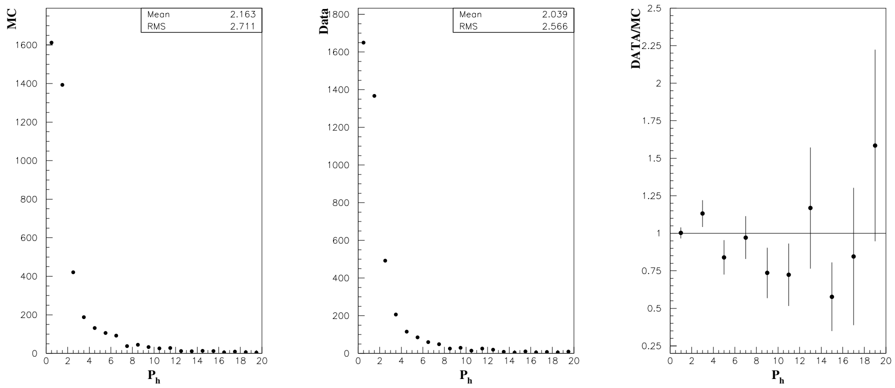

Figure 4.11: Negative hadron momentum distribution. **Left:** Monte Carlo **Center:** data **Right:** data-Monte Carlo ratio.

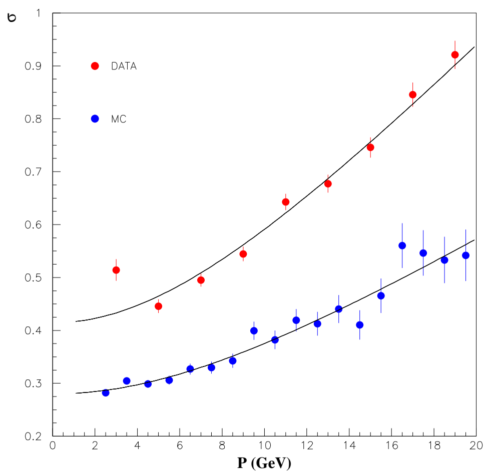

Figure 4.12: Hexagonal magnet resolution on data and simulated events

4.5 Correction factors to the efficiencies

Let's now discuss and evaluate the corrections that we have to apply to the "bare" Monte Carlo efficiencies estimations of section 4.3 in order to take into account the Monte Carlo-data disagreement and the lack, in the emulsion simulation, of the background tracks.

• **Electronic detector simulation corrections** According to the study shown in the previous section there are two corrections that we have to apply to the efficiencies calculations because of the imperfect electronic detector simulation:

A. decreasing of the muon reconstruction efficiency

B. worsening of the hadron momentum resolution

A. The decrease of ϵ_μ. Correcting the ϵ_μ Monte Carlo value means moving part of the 1μ events and adding them to the 0μ sample. We don't know the reason of the ϵ_μ discrepancy. There are two possibilities: the μ track wasn't reconstructed at all in the target region or the track is there but the link procedure with the muon identified by calorimeter and spectrometer failed. A visual scan of the events have assessed that about 50% of the disagreement in the efficiency is due only to linking problem. Analyzing the Monte Carlo $\tau^- \to \mu^- \nu_\tau \bar{\nu}_\mu$ events classified as 1μ or 0μ (tables 4.4, 4.7) we obtain the same explanation: in roughly half of the events the muon was reconstructed in the target region but not linked with the downstream detector. It can clearly be derived by the ratio of η_{kink} values obtained for the two samples. In fact as discussed early, η_{kink} measures also the purity of the sample, i.e. how many times the μ from the τ decay has been selected as one of the scan back track. Therefore it seems that the Monte Carlo, although it overestimates the ϵ_μ, reproduces correctly the reasons of the classification of muon events as muonless. It means that it is reasonable to assume that the overestimated fraction of Monte Carlo 1μ has the same efficiency of the 0μ. The multiplicative correction factors separated for each samples are reported in tab 4.10.

B. Hadron momentum resolution The correction due to the worse momentum resolution of the hadronic spectrometer fit in the data sample has been evaluated smearing track by track the Monte Carlo resolution. Prior to report the results let's note that, checking different data periods, it was discovered that the resolution is not constant in time. More precisely after the introduction of the honeycomb chamber the resolution moves from

$$\sigma\left(\frac{\Delta p}{p}\right) = 0.42 \oplus 0.04 \cdot p \tag{4.10}$$

to

$$\sigma\left(\frac{\Delta p}{p}\right) = 0.96 \oplus 0.11 \cdot p. \tag{4.11}$$

The reasons of this worsening is probably due to some inconsistent alignment procedure between the diamond tracker and the honeycomb chambers. We expect that after a consistent alignment procedure the resolution in the honeycomb period will even be better than the one in 4.10. Unfortunately this problem has not be fixed yet. Therefore we are forced to evaluate two different sets of corrections, one to be applied to the first three years of data and a second for the last year. The results for the two different periods are reported in tab 4.10.

- **Limits and corrections at the emulsion simulation**

As described at page 70 in the emulsion simulation the event uncorrelated background is missing. Its level is not negligible: for instance in bulk, which has been exposed two years at the neutrino beam, the density of background tracks is of the order of 10^2 tracks per mm^2. The background is largely due to two different components: muons from neutrino beam and particles from two SPS West Area beams. The first source is originated by CC interactions in the material upstream of the detector, it has the average direction of the neutrino beam which is upward oriented around 42 mrad. The latter is composed by two test beams, X7 and X9.

Efficiency type	ϵ_μ	DT(1)	DT(2)
$A^{1\mu}_{CC}$	0.933 ± 0.008	-	-
A_{NC}	-	0.954 ± 0.002	0.764 ± 0.019
$A^{0\mu}_{CC}$	1.54 ± 0.20	0.931 ± 0.003	0.743 ± 0.021
$A^{1\mu}_{\tau^- \to \mu^- \nu_\tau \bar{\nu}_\mu}$	0.938 ± 0.009	-	-
$\eta^{1\mu}_{\tau^- \to \mu^- \nu_\tau \bar{\nu}_\mu}$	-	-	-
$A_{\tau^- \to \mathrm{h}^- (n\pi^0)\nu_\tau}$	-	0.961 ± 0.002	0.807 ± 0.015
$\eta_{\tau^- \to \mathrm{h}^- (n\pi^0)\nu_\tau}$	-	0.885 ± 0.006	0.626 ± 0.030
$A_{\tau^- \to e^- \nu_\tau \bar{\nu}_e}$	-	0.978 ± 0.001	0.821 ± 0.014
$\eta_{\tau^- \to e^- \nu_\tau \bar{\nu}_e}$	-	0.871 ± 0.006	0.619 ± 0.031
$A^{0\mu}_{\tau^- \to \mu^- \nu_\tau \bar{\nu}_\mu}$	1.27 ± 0.17	0.958 ± 0.003	0.801 ± 0.016
$\eta^{0\mu}_{\tau^- \to \mu^- \nu_\tau \bar{\nu}_\mu}$	-	0.891 ± 0.006	0.632 ± 0.029

Table 4.10: Multiplicative correction factors on efficiencies. DT(1) and DT(2) indicate respectively the correction for period pre and post honeycomb chamber installation

Both are horizontally directed, they have an angle in the y direction of respectively -80 mrad and -120 mrad. A typical view of track slope distribution is depicted in figure 4.13 where the high directionality of the background is clearly visible.

The absence of the above mentioned background in the simulation compels us to check the reliability of the obtained efficiency values. The background presence enters in the emulsion scanning in all the chain, from interface sheets analysis to kink search.

Let's start describing the effect of the background in the vertex location procedure: it enters in two different ways.

1. It adds fake candidates during the CS and SS scanning, thus triggering the conditions for the χ^2 cut application. Thereby the background presence introduces the chance that the real track is rejected because a fake one is much closer to the target tracker prediction.

2. The background level in bulk is higher than in the interface sheet due to the longer exposure time. Therefore the probability to collect more than one candidate segment during the bulk follow-down is appreciable. To not loose much efficiency it was decided to not apply a criteria, as χ^2, to select only the segment with the best matching: all candidates are followed-back plate by plate. It means that sometimes for the same event more than one vertex

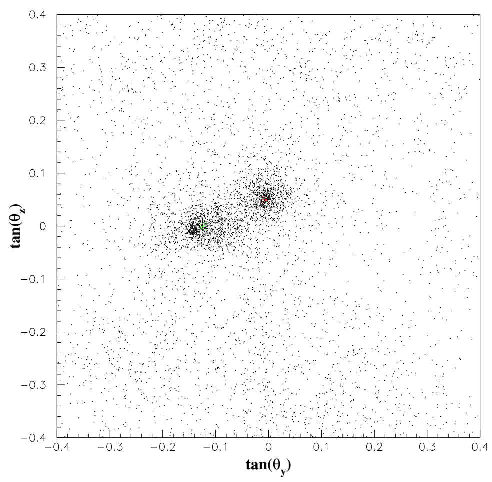

Figure 4.13: Bidimensional plot of background in an emulsion sheet

plate could be defined. The most important consequence of the background presence is the chance that following back the right track we miss the vertex plate because of an accidental presence of a background segment in one of the two plates immediately upstream the "right" vertex plate. Concluding due to the background presence we end up with a number of located vertices that include a fraction of "really" located, but also a fraction of only "apparently" located events.

The last effect of the background has been corrected using the data. A large sample of located events have been manually scanned, and the fraction of events where the vertex plate really contains the vertex has been calculated. A statistical reduction according to the experimentally determined value has been applied at the number of the located events. Note that this correction is quite large, about 20% of the located events are rejected.

The effect of the background not taken into account by the previous statistical correction is the modulation of the localization efficiency. As shown in figure 4.14 the "real" vertex localization efficiency, due to the background presence, is strongly dependent on the slope of the scan back track. A similar behavior is not reproduced by the simulation. Fortunately the introduction of a correction factor for the efficiency slope modulation is not needed. In fact, as displayed in figure 4.9, the scan back angular distribution is quite similar for signal and ν_μ interactions: thus the correction factor has about the same value. Since we are sensitive only to the ratio of location efficiencies for ν_τ and ν_μ interactions (see 3.5), the correction

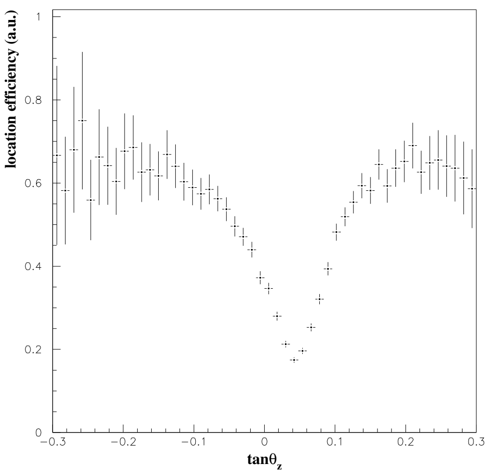

Figure 4.14: Location efficiency as a function of the slope of the track in the z direction (arbitrary units). The minimum efficiency is located in the zone of high background track density around the beam direction.

factor cancels out in the division. Notice that this argument allows us to disregard also the effect of the background described in 1).

The presence of the background modifies also the kink efficiency in two ways. **A** For each candidate stopped in bulk before applying the parent search a cut is applied. The cut consists in requiring that the stopped candidate fulfills the condition

$$\chi^2 = \left(\frac{\Delta\theta_y}{\sigma_{\Delta\theta_y}}\right)^2 + \left(\frac{\Delta\theta_z}{\sigma_{\Delta\theta_z}}\right)^2 + \left(\frac{\Delta y}{\sigma_{\Delta y}}\right)^2 + \left(\frac{\Delta z}{\sigma_{\Delta z}}\right)^2 < 16 \tag{4.12}$$

where $\Delta\theta_{y,z}$ is the difference in slope between the SS measurements and the value at the vertex plate +1. $\Delta y, z$ are the difference of position between the prediction made by the measurements in vertex plate +2 and the value found in vertex plate+1. The values of σ are

$$\sigma_{\Delta\theta_{y,z}} = 0.006 + 0.04 \cdot \tan\theta^2_{y,z} \tag{4.13}$$

$$\sigma_{\Delta y,z} = 4 + 11 \cdot \tan\theta^2_{y,z}\ (\mu m) \tag{4.14}$$

This cut aims to reject the fraction of "apparent" located events (see previous page), the fraction of which we take into account statistically decreasing the number of automated located events. Reducing the sample for which the parent search algorithm is applied is very appealing since it automatically diminishes the manual scanning load without loss of efficiency[8]. In fact the “apparent” localized events are unusable for kink detection since the plate containing the kink point has not been identified. The same χ^2 cut is not applied before the SVSB kink algorithm since this kink search method automatically rejects the incorrectly located events.

The χ^2 cut rejects a small fraction of “real” located events, thus it decreases the kink efficiency value. The correction to the kink efficiency has not been calculated on Monte Carlo ν_τ events because it is very influenced by the tail of the TS resolution which are difficult to determine and reproduce correctly. A more significant determination comes from the data themselves. We use a sample of events where the automated defined vertex plate contains really the interaction point. They are identified as those events in which other target tracks, apart the scan back, have been confirmed to exist in the vertex plate and they have small impact parameter with each other. The χ^2 distributions obtained for this sample is depicted in figure 4.15, it permits to evaluate that the kink efficiency, η_{LL} and η_{LHL}, must be decreased with a multiplicative factor, η_{χ^2}, equal to 0.937 ± 0.002.

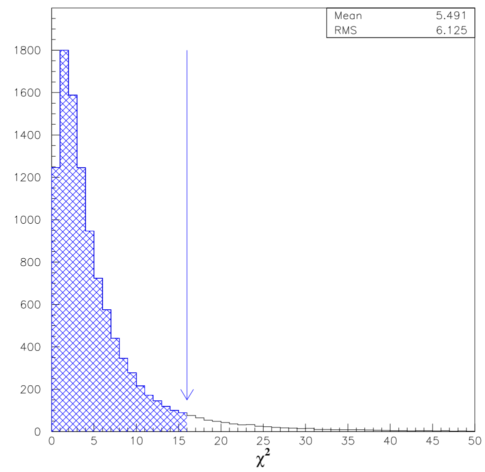

Figure 4.15: χ^2 distribution for localized vertices confirmed by small impact parameter measurements. The hatched region is the one retained by the cut.

B Besides the η_{χ^2} factor the background has another effect, called η_{bg} on kink efficiency of LL and LHL methods. It introduces the possibility that a true parent track is rejected if a background segment results to be accidentally associated

[8]As described at page 63 the largest fraction of event selected by the parent track search are picked for accidental reasons

with the parent candidate during the test to eliminate the fake parent candidates, i.e. during the check that the candidate is not present on the plate immediately downstream the vertex plate. It has been estimated that it may happen in about 2% of the cases [21] thus η_{bg} is equal 0.98.

Summarizing the effect of the background on the oscillation evaluation can be modeled by two correction factors at the kink efficiency:

$$\eta_{data} = \eta_{MC} \cdot \eta_{\chi^2} \cdot \eta_{bg} \tag{4.15}$$

where η_{MC} is the "bare" efficiency value reported in tables 4.4, 4.5, 4.6 and 4.7 and $\eta_{\chi^2} = 0.937$ and $\eta_{bg} = 0.98$.

Chapter 5

Estimation and reduction of the background

The background events to $\nu_\mu \to \nu_\tau$ oscillation search in CHORUS can be divided in two groups. One is the ν_τ prompt component of the beam, which is typical of every experiment of ν_τ appearance. The other is strongly related to the kink signature chosen in the CHORUS experiment to identify the τ, thus peculiar of CHORUS. Both these background sources will be estimated in this chapter.

As it will be shown below the ν_τ prompt gives a negligible background expectation. Instead the contribution given by the second source is at a considerable level, more than one order of magnitude larger than the ν_τ prompt contribution. A careful study trying to reduce it has been developed and will be described along this chapter.

The chapter is organized in the following way:

- estimation of the background due to prompt ν_τ beam component
- explanation of the CHORUS peculiar background source
- estimation of the 0μ sample background
- estimation of the 1μ sample background
- study of background reduction

5.1 Background due to the prompt ν_τ beam component

The number of ν_τ CC interactions per ν_μ CC interactions has been estimated to be $\simeq 3 - 4 \times 10^{-6}$ [27]. Since the total number of located ν_μ CC interactions in CHORUS is about 140.000, using the value of the location efficiencies reported in the previous chapter, we expect about 0.07-0.1 events of $\tau^- \to \mu^- \nu_\tau \bar{\nu}_\mu$ and

0.2-0.3 of $\tau^- \to h^-(n\pi^0)\nu_\tau$ to be located in emulsion[9]. Multiplying these number of events for the kink efficiencies we estimate that the number of ν_τ prompt detected in the 1μ channel is 0.03-0.04, whereas in the 0μ sample is 0.04-0.06. The prompt component yields ≤ 0.1 background events in the scanned statistics; thus its contribution is negligible.

5.2 Topological background

The τ detection in CHORUS is topological, i.e. it is based on the observation of a kink on a negative track from a neutrino vertex. No other criteria to distinguish ν_τ events from the rest are applied at the scanning level. Of course during the post-scanning analysis it is possible to employ some background reduction criteria, but they don't change the essence of the ν_τ identification. It remains based on the kink detection. Therefore all the events with a kink topology are possible sources of background.

There are essentially two classes of events, without a τ, that can exhibit a kink in emulsion, thus constituting a background.

- All negative charged particles that decay in 1-prong produce a kink signature that fakes a τ decay. Let's call it a "physical" background source for a kink-based τ detection.

- The other background source is more "instrumental". It is due to the limit of the detector, the emulsion, to identify the nucleus recoil or break-up in case of hadron-nucleus interactions with small transfered energy. What might happen is that a negative hadron interacts with the emulsion material, changes its direction but perturbs the nucleus so weakly that no signals of the interaction are detected. In this case we would see in emulsion a kink topology that doesn't correspond to a decay. The contamination from "apparent" kinks not due to decays but to interactions, introduces a large background in the τ hadronic decay search.

For the 0μ sample the following background sources will be considered

- ♦ single charm produced by ν_μ or $\overline{\nu}_\mu$ charged current interactions with subsequent hadronic 1-prong decay

[9] We are implicitly assuming that the ν_τ prompt energy spectra is not very different from the one used to evaluate the analysis efficiencies.

- ♦ associate charm produced in ν_μ charged and neutral current with subsequent hadronic 1-prong decay of one of the two charmed particles
- ♦ hadronic decays of negative kaons produced in ν_μ charged current interactions
- ♦ negative hadrons interactions in ν_μ neutral current processes

For the 1μ sample the following background sources will be considered

- ◇ single charm produced by ν_μ or $\overline{\nu}_\mu$ charged current interactions that decay in a muon
- ◇ associate charm produced in ν_μ charged and neutral current interactions with subsequent muonic decay of one of the two charmed particles
- ◇ muonic decay of negative kaons and pions produced in ν_μ charged current interactions
- ◇ single charm produced in ν_μ charged current interactions when the primary muon is wrongly associated to the prong from the charm decay
- ◇ negative hadrons interactions in ν_μ charged current processes when the primary muon is wrongly associated with the hadron that interacts

All the "physical" background will be estimated using the simulation of the analysis chain described in the previous chapter. The efficiencies that will be used are already corrected for the Monte Carlo-data disagreement identified in the previous chapter (see section 4.5). The "physical" background will be estimated as a rate with respect to the number of located events to get rid of part of the systematics in the neutrino flux knowledge and in the location efficiency. In particular the background to the 0μ (1μ) sample will be normalized to the 0μ (1μ) located events. With this choice of the normalization sample the detector that identifies and measures the scanback track is the same for the background events and for the normalization sample. This assures to reduce the systematic due to possible residual uncorrected disagreement of Monte Carlo and data with respect to the scan back selection, which is the most crucial point in the location efficiency simulation.

On the contrary, as it will be shown, the "instrumental" background will be normalized using the CHORUS data themselves.

Let's remark that all the background estimations that will be shown in the following assume that the post-scanning criteria are the standard ones, i.e. transverse momentum of the decay particle greater than 250 MeV and a maximum decay length of five plates for the $\tau^- \to \mu^- \nu_\tau \overline{\nu}_\mu$ search and three for $\tau^- \to \mathrm{h}^- (n\pi^0)\nu_\tau$.

5.3 Background to the 0μ sample

5.3.1 Single charm produced by $\overline{\nu}_\mu$ charged current interactions

Single charged charmed hadron produced in antineutrino charged current scattering constitutes a background by means of the production and decay chain

$$\begin{array}{lll} \overline{\nu}_\mu N \to & h_{\overline{c}} & \mu^+ X \\ & \downarrow & \\ & h^- & +neutrals \end{array} \tag{5.1}$$

if the primary muon is missed. $h_{\overline{c}}$ represents one of the charged charmed particles, D^-, D_s^- and Λ_c^-.

The background rate can be written as [10]

$$\frac{N^{0\mu}_{\overline{\nu}_\mu}}{N^{0\mu}_{loc}} = \frac{\phi_{\overline{\nu}_\mu} \sigma^{charm}_{\overline{\nu}_\mu} BR(charm \to h_{\overline{c}}) BR(h_{\overline{c}} \to 1\ prong) A^{0\mu}_{charm} \eta^{0\mu}_{charm}}{\phi_{\nu_\mu}(\sigma^{CC}_{\nu_\mu} A^{0\mu}_{CC} + \sigma^{NC}_{\nu_\mu} A_{NC})} \tag{5.2}$$

where $\phi_{\overline{\nu}_\mu}$ (ϕ_ν) is the antineutrino (neutrino) flux, $\sigma^{charm}_{\overline{\nu}_\mu}$ is the cross section for charm production in antineutrino interactions, $\sigma^{CC}_{\nu_\mu}$ ($\sigma^{NC}_{\nu_\mu}$) is the neutrino CC (NC) cross section. $BR(charm \to h_{\overline{c}})$ is the probability that a charm hadronizes in a $h_{\overline{c}}$; $BR(h_{\overline{c}} \to 1\ prong)$ is the branching ratio for the one-prong decay; $A^{0\mu}_{charm}$ and $\eta^{0\mu}_{charm}$ are the location and kink efficiencies for the background sample. $A^{0\mu}_{CC}$ and A_{NC} are the location efficiencies for ν_μ NC and CC interactions classified as 0μ evaluated in the previous chapter.

The ratio of neutrino and antineutrino fluxes is 5.8% (see tab 4.8). The ratio of cross sections can be evaluated by the relation

$$\frac{\sigma^{charm}_{\overline{\nu}_\mu}}{\sigma^{CC}_{\nu}} = \frac{\sigma^{charm}_{\overline{\nu}_\mu}}{\sigma^{CC}_{\overline{\nu}_\mu}} \frac{\sigma^{CC}_{\overline{\nu}_\mu}}{\sigma^{CC}_{\nu}} = 0.05 \cdot 0.44 = 0.022 \tag{5.3}$$

the value of $\sigma^{charm}_{\overline{\nu}_\mu}/\sigma^{CC}_{\overline{\nu}_\mu}$ has been measured by [23], whereas for the ratio of $\overline{\nu}_\mu$ and ν_μ CC cross section and the ratio of ν_μ CC and NC cross sections see tab 4.9.

[10] For sake of simplicity all the background estimation formulas are written without explicitly mention the integral over the ν energy. Anyhow the correct energy dependence has been used to evaluate the cross-section, fragmentation and efficiencies values inserted in the formulas.

The fragmentation function for the charm in a charged hadron and the one-prong branching ratio have been estimated by JETTA a Lund-based generator [19]. It results that $BR(charm \rightarrow h_{\overline{c}}) = 0.32$ and $BR(h_{\overline{c}} \rightarrow 1prong) = 0.36$. Both these values are in good agreement with the existing data [28, 5].

Using a simulated sample of 5200 one-prong charm decay it results $A^{0\mu}_{charm} = (3.0 \pm 0.4)\%$ and $\eta^{0\mu}_{charm} = (8.3 \pm 2.7)\%$.

Therefore the background rate is

$$\frac{N^{0\mu}_{\overline{\nu}_\mu}}{N^{0\mu}_{loc}} = 0.058 \cdot 0.022 \cdot 0.32 \cdot 0.36 \frac{0.0025}{0.103} = (3.6 \pm 1.2 \pm 0.9) \cdot 10^{-6} \tag{5.4}$$

where the two errors represent respectively the statistics and the systematic. The systematic error has been estimated assuming an error of 10% of the neutrino flux, 20% in the cross-sections, 10% in the charm fragmentation and 5% in the 1-prong branching ratio.

5.3.2 Single charm produced by ν_μ charged current interactions

Single charged charmed hadrons produced in neutrino charged current scattering constitute a background by means of the production and decay chain

$$\begin{array}{lll} \nu_\mu N \rightarrow & h_c & \mu^- X \\ & \downarrow & \\ & h^+ & +neutrals \end{array} \tag{5.5}$$

if the negative primary muon is missed and if the charge of the hadron originated in the charm decay is wrongly reconstructed as negative. h_c represents one of the charged charmed D^+, D^+_s and Λ^+_c.

The background rate can be written as

$$\frac{N^{0\mu}_{\nu}}{N^{0\mu}_{loc}} = \frac{\phi_\nu \sigma^{charm}_{\nu} BR(charm \rightarrow h_c) BR(h_c \rightarrow 1prong) A^{0\mu}_{charm} \eta^{0\mu}_{charm}}{\phi_\nu (\sigma^{CC}_{\nu} A^{0\mu}_{CC} + \sigma^{NC}_{\nu} A_{NC})} \tag{5.6}$$

where σ^{charm}_{ν} is the charm production cross section in neutrino charged current interactions.

The value of $\sigma^{charm}_{\nu}/\sigma^{CC}_{\nu}$ has been estimated using the CHORUS events generator. It results 0.05 in good agreement with other measurements [17]. From the generator also the charm fragmentation and decay branching ratio have been estimated. It results that 38% of the charm quark hadronizes in a charged particle. The one-prong branching ratio results equal to 0.35. Using a simulated sample of 63000 neutrino induced charm events the values $A^{0\mu}_{charm} = (4.4 \pm 0.1)\%$ and $\eta^{0\mu}_{charm} = (1.2 \pm 0.2)\%$ were obtained. Therefore the background rate is

$$\frac{N^{0\mu}_{\nu}}{N^{0\mu}_{loc}} = 0.05 \cdot 0.38 \cdot 0.35 \cdot \frac{0.044 \cdot 0.012}{0.103} = (3.4 \pm 0.6 \pm 0.8) \cdot 10^{-5} \tag{5.7}$$

The systematic error has been estimated assuming 20% error on the cross-section, 10% on the fragmentation and 5% on the branching ratio.

This background rate is about an order of magnitude larger than the one from antineutrino. This result is not surprising. The flux times cross section reduces the $\overline{\nu}_{\mu}$ background rate with respect to the ν_{μ} of a factor of about 40. On the contrary the location and kink efficiencies augments the $\overline{\nu}_{\mu}$ rate of about a factor four. There are two reasons that make the location times kink efficiencies only a factor four larger for $\overline{\nu}_{\mu}$ than for ν_{μ}. The first reason is the muon identification efficiency. As depicted in figure 5.1 the momentum of the primary muon is on average greater for $\overline{\nu}_{\mu}$ than for ν_{μ}. Therefore the muon missing probability is larger in ν_{μ} than in $\overline{\nu}_{\mu}$ events of about a factor 1.5.

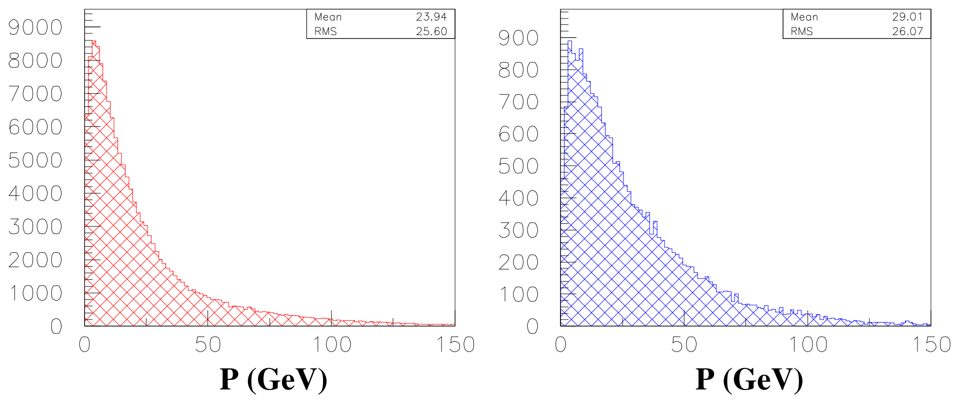

Figure 5.1: Momentum of muon from primary vertex. **Left panel:** neutrino charm production. **Right panel:** antineutrino charm production.

The second reason is the limited hadron momentum resolution. Using the resolution obtained from data and the spectrum of the charm decay product the charge mis-identification probability is $(15 \pm 1)\%$ (fig 5.2). Therefore the $\overline{\nu}_{\mu}/\nu_{\mu}$

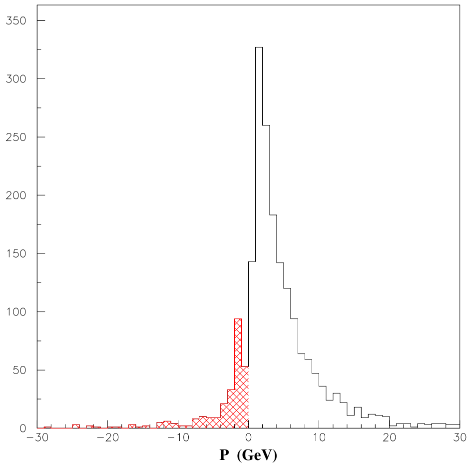

Figure 5.2: Reconstructed momentum for the positive hadron produced in charm decay. The hatched area corresponds to the events with wrong-sign charge reconstruction

efficiency ratio is under control:

$$\frac{A^{\overline{\nu}_\mu}_{charm} \cdot \eta^{\overline{\nu}_\mu}_{charm}}{A^{\nu_\mu}_{charm} \cdot \eta^{\nu_\mu}_{charm}} \simeq \frac{\epsilon^{\overline{\nu}_\mu}_{miss\mu}}{\epsilon^{\nu_\mu}_{miss\mu}} \cdot \frac{1 - P(wrong\ charge)}{P(wrong\ charge)} = \frac{1}{1.5} \cdot \frac{0.85}{0.15} \simeq 4 \tag{5.8}$$

5.3.3 Associated charm production in ν_μ charged and neutral interactions

The associated charm production can occur in charged current neutrino interactions by the gluon splitting, whereas in neutral current the dominant contribution comes from the gluon boson fusion diagram. This mechanism produces two charmed hadrons in the final state. Out of the four possible hadronization configurations of the $c\overline{c}$ pair, only the one with a negative hadron plus a neutral meson in the final state can constitute a background for the ν_τ search if the charged charm decay is detected and the neutral one is missed.

The most accurate measurement of the production cross section of $c\overline{c}$ in neutral current is $0.21^{+0.18}_{-0.15}$ fb [29] on a neutrino beam of average energy $\sim 150\ GeV$. This cross section is strongly dependent on the beam energy due to the threshold of the charm mass. Simulation of the process based on HERWIG generator [30] showed that at CHORUS energy it is reduced by more than a factor ten [31]. Therefore we expect at CHORUS energy

$$r = \frac{\sigma(\nu_\mu N \to \nu_\mu c\overline{c}X)}{\sigma(\nu_\mu N \to \nu_\mu X)} \sim 4 \cdot 10^{-4} \tag{5.9}$$

The background rate due to associated charm production in NC interactions can be written as[11]:

$$\begin{aligned}\frac{N^{NC}_{c\overline{c}}}{N^{NC}_{loc}} \sim \frac{\sigma(\nu_\mu N \to \nu_\mu c\overline{c}X)}{\sigma(\nu_\mu N \to \nu_\mu X)} \cdot BR(c \to D^0) \cdot BR(\overline{c} \to D^-) \cdot \\ BR(D^- \to h^- + neutrals) \cdot \eta_{kink}\end{aligned} \tag{5.10}$$

where the location efficiencies for NC events and $c\overline{c}$ events have been assumed the same then they cancel out. The simulation of the associated charm production gives for $BR(c \to D^0) \cdot BR(\overline{c} \to D^-)$ the value 0.12 [31]. For the $BR(D^- \to h^- + neutrals)$ the value 0.36 is used (see section 5.3.1). For η_{kink} we can reasonably assume the value calculated in the events of single charm produced by $\overline{\nu}_\mu$ CC interactions (see page 101). Therefore

$$\frac{N^{NC}_{c\overline{c}}}{N^{NC}_{loc}} \sim 4 \cdot 10^{-4} \cdot 0.12 \cdot 0.36 \cdot 0.1 \sim 2 \cdot 10^{-6} \tag{5.11}$$

The background rate from associated production in CC interactions can be written as

$$\begin{aligned}\frac{N^{CC}_{c\overline{c}}}{N^{NC}_{loc}} = & \frac{\sigma(\nu_\mu N \to \mu c\overline{c}X)}{\sigma(\nu_\mu N \to \nu_\mu X)} \cdot P(miss\ \mu) \cdot BR(c \to D^0) \cdot BR(\overline{c} \to D^-) \cdot \\ & BR(D^- \to h^- + neutrals) \cdot \eta_{kink}\end{aligned} \tag{5.12}$$

where $P(miss\ \mu)$ is the probability of missing the primary muon. The cross section for associated charm production in charged current interactions has not been measured yet. It exists an upper limit, $\sigma(\nu_\mu N \to \mu c\overline{c}X)/\sigma(\nu_\mu N \to \nu_\mu X) <$ 0.39% at 90 C.L. ([17]). The probability of missing muon estimated from Monte Carlo yields $\sim$ 10%. The background rate is then

$$\frac{N^{CC}_{c\overline{c}}}{N^{NC}_{loc}} < 0.39 \cdot 10^{-2} \cdot 0.10 \cdot 0.12 \cdot 0.36 \cdot 0.1 \sim 2 \cdot 10^{-6} \tag{5.13}$$

This background estimation is affected by big uncertainties coming from cross section measurements and from D^0 detection efficiency. Its rate, however, seems to be low enough to allow us to neglect its contribution to the total background rate.

[11] Here we make the pessimistic assumption that the D^0 can never be identified so that the event cannot be recognized as an associate charm production process

5.3.4 Negative kaons produced in ν_μ interactions

Although the kaon decay length is quite long compared to the depth of one emulsion stack they are produced so copiously that some of them decay inside the emulsion. The average number of K per NC neutrino interaction is ~ 0.1 with an average momentum of about 6 GeV. The probability that a kaon decays within three plates is $\sim 2 \cdot 10^{-4}$. Therefore the expected background rate with respect to the number of located events in the 0μ sample can conservatively be estimated as:

$$\frac{N_K^{bg}}{N_{loc}^{0\mu}} \simeq < N_k > \cdot P_{decay} \cdot \eta_{kink} \cdot \epsilon_{Pt} \cdot BR(K^- \to \pi^- + neutrals) \qquad (5.14)$$

where the location efficiencies for NC events and K decay events have been assumed to be equal. η_{kink} here indicates only the kink detection efficiency prior to the $\mathrm{P_t}$ cut. An estimation of η_{kink} can be derived by the result of the simulation of $\tau^- \to \mathrm{h}^-(n\pi^0)\nu_\tau$: $\eta_{LL} \sim 0.3$. Note that since the kink angle for kaon decay is smaller than for τ decay and the parent search is inefficient at small angle, the assumption on η_{kink} is a conservative one. The value of the $\mathrm{P_t}$ cut at 250 MeV on the kaon has been estimate by a toy Monte Carlo that takes into account the kaon spectra, the hadron momentum resolution and the angular resolution. It results to be ~ 0.15. Thus

$$\frac{N_K^{bg}}{N_{loc}^{0\mu}} \simeq 0.1 \cdot 2 \cdot 10^{-4} \cdot 0.3 \cdot 0.15 \cdot 0.3 = 3 \cdot 10^{-7} \qquad (5.15)$$

which is negligible compared to 5.4 and 5.7

5.3.5 Hadronic interactions

A interaction in emulsion of an hadron outcoming from the primary vertex can fake a $\tau^- \to \mathrm{h}^-(n\pi^0)\nu_\tau$ decay. It occurs when the interaction produces only one minimum ionising particle and no heavily ionising tracks or other signs of nuclear break-up as blobs or Auger electrons are present. These interactions are usually called WHITE STAR KINK (WSK).

The WSK background source is very difficult to be estimated. There are very few measurements in literature. Moreover to transport the measurement obtained in one experimental condition to another is not straightforward. This difficulty is connected to the strong dependence of the WSK cross-section from the emulsion composition and the scanning technique used.

The lack of experimental data to predict the WSK background has lead us to use the CHORUS data themselves to estimate it. This is possible since we can identify a sample of kink events which are for sure WSK. They are the kink events found during the τ search with a distance between the neutrino vertex and the kink point too large to be compatible with the τ or charm decay lengths [12]. Let's call it reference region. Using the events in this region we evaluate the WSK interaction length λ_{WSK} . Unfortunately knowing only λ_{WSK} the determination of the expected background is possible but not very robust. In fact the λ_{WSK} that we determine from data automatically includes the location and the kink efficiency averaged on the reference sample. But the efficiencies depend on the decay length, therefore a purely geometrical extrapolation of the expected WSK from the reference region to the τ signal region is not very accurate. To solve this problem and for further studies as background reduction, a simulation of the WSK has been developed.

White Star Kink simulation

The White Start Kink simulation is composed of two separate parts. The first is the generation of the hadron interactions in emulsion, the latter is the simulation of the emulsion response to the different particles passage.

The hadron-emulsion interactions have been simulated using FLUKA [32, 33]. FLUKA simulator has been chosen essentially for two reasons. The first is its accuracy in reproducing hadronic interactions [34]. The second, very important for our purposes, is its ability to describe the interaction on the single nucleus of a compound material and the subsequent evaporation or deexcitation of the residual nucleus [35].

Once we got a description of negative pions interactions on the emulsion material, we need to know how these interactions appear to the scanner, viz. kink events with or without signs of nuclear interactions or multi-prong event. To get this classification we need to define the emulsion sensitivity to the different particles. Prior to describe the procedure let's remind some information about the emulsion. *Silver halide emulsion consists in about equal part by volume of halide crystals and a matrix material which is chiefly gelatin. An ionizing particle on encountering a crystal may render it developable. After development, followed by fixing and washing to remove the undeveloped crystals, the gelatine is transparent. With a microscope the paths of the charged particles that penetrated the emulsion are visible as trails of minute silver grains* [36]. Thus our problem to define whether a particle is detectable or not translates in the problem of when a particle makes the crystals developable[13]. Although it is well known that what makes a silver

[12] The contamination from K hadron decay at this decay length is negligible, less than 0.2 events

[13] Lets note that a charged particle passage in emulsion can be detected directly if it makes

halide crystal developable is the absorption of energy from moving charged particles incident on it, no quantitative description of it exists. Thus we are forced to use some empirical criteria to reproduce the emulsion response.

It has been experimentally determined the following [36]:

- for minimum ionizing particle (β roughly greater than 0.7) only a part of the silver crystals encountered receive sufficient quantity of energy to become developable: about 30 grains per 100 μm. Anyhow due to the long path traversed by the particle it can be revealed with essentially unitary efficiency.
- for particles with intermediate velocity (β roughly greater than 0.25 and less than 0.7) the ionizing power increases with respect to the m.i.p. therefore their efficiency in making the crystal developable reaches almost 100%. Therefore these particles are "always" detected during the scanning also if their path is shorter than for a m.i.p.
- for slow moving particles (β roughly less than 0.25) the situation is more complicate. The emulsion sensibility depends on particle mass and charge.

Let's discuss the last case in some detail since it is crucial for our aim to define when signs of a nuclear interaction, usually very slow moving objects, are visible. In literature lots of measurements of range, defined as the path in pre-developed emulsion, as a function of kinetic energy of the particle, exist[36]. If we set the minimum range for a detectable particle at 1 μm [14] it translates in energy threshold:

- for electron and positron 1 KeV of kinetic energy
- for proton 0.1 MeV of kinetic energy
- for multiple charged ions usually produced in hadron-emulsion interactions the approximate values of kinetic energy threshold are about 0.4 MeV for α particles, 2 MeV for medium elements (carbon oxygen and nitrogen) and about 10 MeV for heavy elements (silver, iodine and bromine)[15]

developable a crystal but also indirectly if it extracts internal electron from atom (δ ray) without making developable the crystal to which the electron belonged. In fact these electrons usually have enough energy to make some other crystal developable.

[14]This is a very safe assumption since in 1 μm out of the interaction point there is on average one developable crystal grain, which is of course the minimum for a track to be detected.

[15]The kinetic threshold energy is calculated by the minimum β which is the solution of the equation $R(\mu m) = \frac{M}{z^2}\lambda(\beta) + Mz^{2/3}0.1\frac{\beta}{137 \cdot z} = 1$ where $\lambda(\beta)$ is the range of proton of velocity β.

With this description of the emulsion response to the particle passage it is possible to define which hadronic interactions appear as white kinks.

To test the reliability of the WSK simulation a comparison of the obtained results with the only available measurement has been done[16]. In a test beam at KEK the white kink events resulting from the 4 GeV negative pions interactions in emulsion has been studied [37]. The $\mathrm{P_t}$ distribution of the observed events is shown in figure 5.3. It has been fitted with the function $\exp^{-20Pt}$. The simulated events (the right part of the figure) reproduce quite well the observed distribution, in fact the fit results is $\exp^{-(23\pm3)\cdot Pt}$. Note that the tail at high $\mathrm{P_t}$ visible in the simulation corresponds to less than 1 event in the KEK statistics.

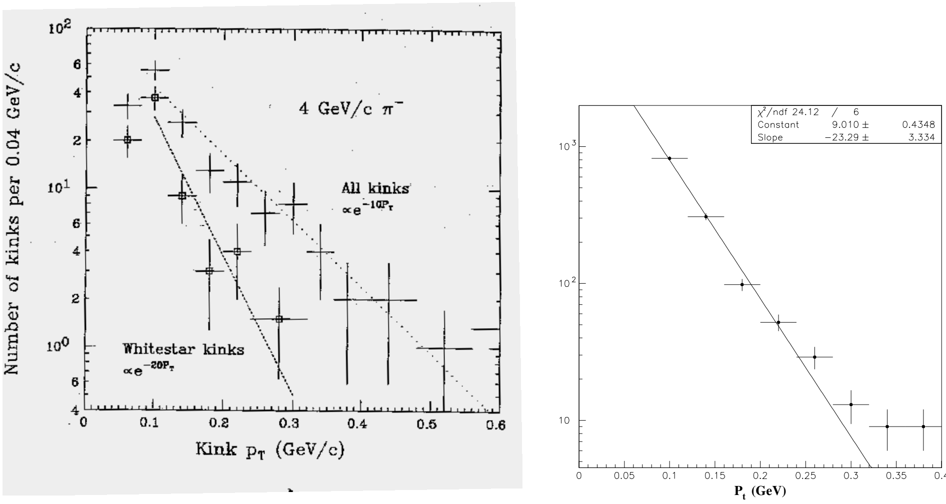

Figure 5.3: $\mathrm{P_t}$ distribution for WSK of negative pions of 4 GeV. **Left panel:** KEK measurement.**Right panel:** WKS simulation.

Background estimation

To estimate the expected background, a large sample of ν_μ NC interactions in which one of the hadrons undergoes to an interaction without visible recoil have been simulated including both the GEANT tracking and the analysis simulation. It permits a further check of the WSK simulation using the CHORUS data. The θ and $\mathrm{P_t}$ distribution of the kink events in the reference region are compared to the expected ones. As shown in figure 5.4 and 5.5 the agreement is good inside the limited statistics.

[16] Other tests have been done but the analysis of the data is still in progress

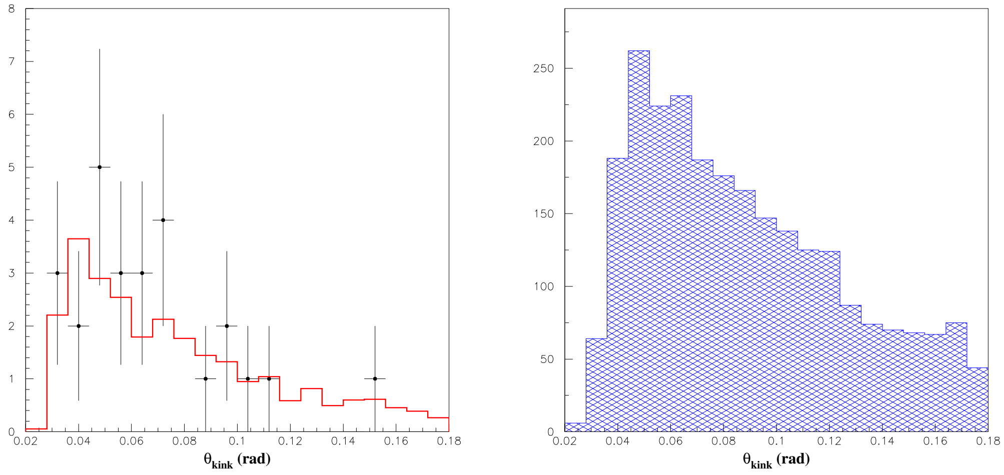

Figure 5.4: The θ_k distribution. **Left panel:** The histograms represents the WSK expected distribution. Superimposed points are the CHORUS data. **Right panel:** expected distribution for $\tau^- \to \mathrm{h}^-(n\pi^0)\nu_\tau$ events

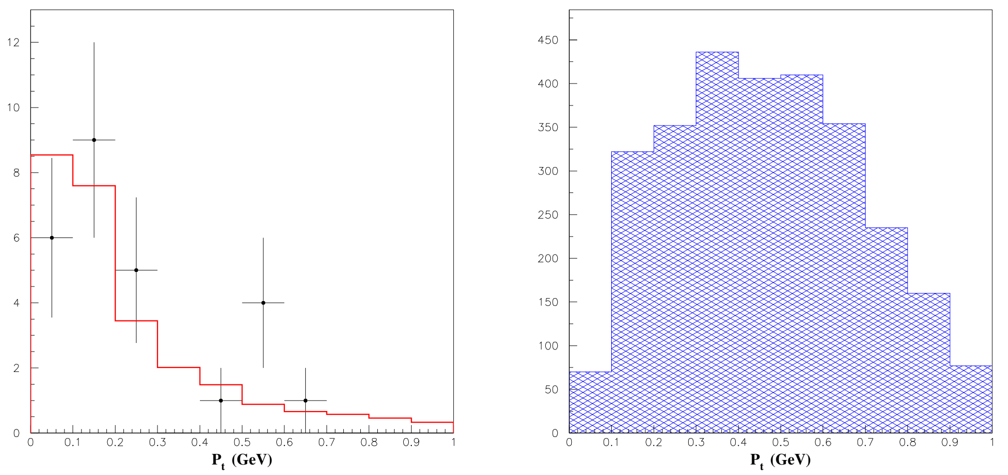

Figure 5.5: The $\mathrm{P_t}$ distribution. **Left panel:** The histograms represents the WSK expected distribution. Superimposed points are the CHORUS data. **Right panel:** expected distribution for $\tau^- \to \mathrm{h}^-(n\pi^0)\nu_\tau$ events

In the figures also the expected distribution for the signal is depicted to show that at least for the P_t variable the difference from the data is strong to permit to assess that the events in the reference region are not likely to contain signal.

Let's now estimate the expected background. The idea, as mentioned above, is to extrapolate the number of events observed in the reference region in the signal region. The reference region is defined as the one for which the kink point is farther than three plates from the neutrino vertex. The extrapolation of the observed events in the signal region has been done using the WSK full simulation. It permits to obtain the expected distribution of WSK as a function of the distance between the neutrino vertex and the hadron interaction point. The bare Monte Carlo distribution must be corrected to take into account the background in emulsion (see chapter 4). To evaluate the effect of the background on the distribution of the distance between the ν vertex and the kink point we studied the located vertex distributions for 0μ data and Monte Carlo (figure 5.6). Both distributions

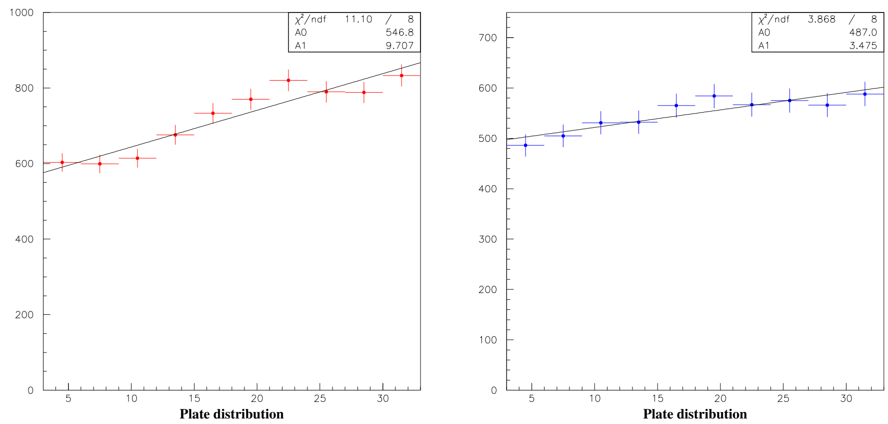

Figure 5.6: Located vertex plate distribution in 0μ events. **Left panel:** data. **right panel:** simulated events.

show that most upstream vertices are located less efficiently. In Monte Carlo this is due to several causes, multiple scattering, more probability for upstream interactions to develop an early shower, which complicates the electronic detector track reconstruction and thus the goodness of the prediction, and adds background in emulsion. In the data the presence in emulsion of event uncorrelated background increases the effect already present in Monte Carlo. Thus to correct for the lack of the emulsion background in the Monte Carlo the difference of the behavior of the plots in figure 5.6, proportional to $0.787 + 0.006 \cdot N_{plate}$ has been applied on the Monte Carlo location efficiency.

The obtained WSK distribution as a function of the distance between the neutrino vertex and the hadron interaction point is shown in figure 5.7. It permits

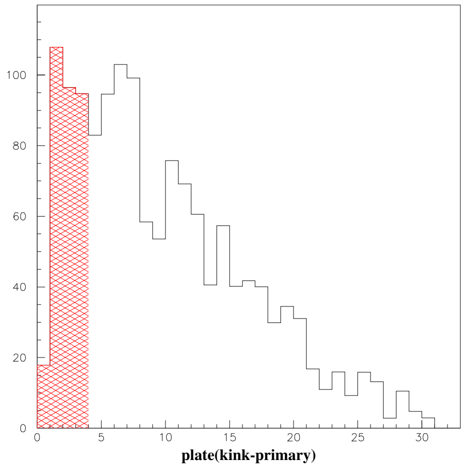

Figure 5.7: Expected distribution in the plate distance between the neutrino point and the kink point for WSK. The hatched (not-hatched) region corresponds to the event in the signal (reference) region.

to estimate that

$$\frac{N_{WSK}(in\ signal\ region)}{N_{WSK}(in\ reference\ region)} = 28.3 \pm 1.7\% \tag{5.16}$$

Since CHORUS observed 26 WSK events in the reference region out of which 8 have $\mathrm{P_t}$ larger than 250 MeV, we expect that the number of background events coming from hadron interaction is

$$N_{WSK}(in\ signal\ region) = 8 \cdot 0.283 = 2.3 \pm 0.8 \tag{5.17}$$

Since the total hadronic track length scanned in CHORUS is 243 m, the "effective" λ_{WKS} observed in CHORUS is $23.6 \pm 8.4\ m$.

The background estimation made now implicitly assumes that the kink point occurs in the emulsion layer. On the contrary if the kink is located in the plastic a different estimation must be done due to the impossibility to analyse during the scanning the kink point thus to distinguish white kinks from events with nuclear break-up signs. A conservative estimation of the background from interaction occurring in the plastic has be done in the following way [38]. During the τ search in CHORUS 17 events have been found in the reference region with $\mathrm{P_t} >$ 250 MeV with signs of nuclear interaction. Thus a total of 8+17=25 events have been found with secondary interaction point in emulsion. Scaling for the different interaction lengths and thicknesses of the plastic with respect of the emulsion, we get an estimation of about 1.6 hadronic interaction in plastic with $\mathrm{P_t} > 250$ MeV expected in the reference region. Extrapolating this number to the signal region we obtain 0.4 ± 0.1 background expected events. Therefore the total number of background events due to hadron interaction in the whole emulsion plate is 2.7 ± 0.8.

5.4 Background to the 1μ sample

5.4.1 Single charm produced in ν_μ or $\overline{\nu}_\mu$ CC interactions followed by the muonic charm decay

Single charged charmed hadron production in ν_μ or $\overline{\nu}_\mu$ charged current scattering constitutes background by means of the production and decay chain

$$\begin{array}{lll} \overline{\nu}_\mu\ (\nu_\mu)N \rightarrow & h_{\overline{c}}^-\ (h_c^+) & \mu^+\ (\mu^-)X \\ & \downarrow & \\ & \mu^-\ (\mu^+) & +neutrals \end{array} \tag{5.18}$$

if the primary muon is missed and, in case of ν_μ interactions, if the charge of the muon originated in the charm decay is wrongly reconstructed as negative. The background rate for the antineutrino is

$$\frac{N_{\overline{\nu}_\mu}^{1\mu}}{N_{loc}^{1\mu}} = \frac{\phi_{\overline{\nu}_\mu}\sigma_{\overline{\nu}_\mu}^{charm} BR(charm \rightarrow h_{\overline{c}}) BR(h_{\overline{c}} \rightarrow \mu^- + neutrals) A_{charm}^{1\mu}\eta_{charm}^{1\mu}}{\phi_\nu \cdot \sigma_\nu^{CC} \cdot A_{CC}^{1\mu}} \tag{5.19}$$

Using a sample of 1500 simulated background events it was obtained $A_{charm}^{1\mu} = 0.061 \pm 0.010$ and $\eta_{charm}^{1\mu} = 0.32 \pm 0.07$. From the generator it has been estimated that $BR(h_{\overline{c}} \rightarrow \mu^- + neutrals) = 0.081\%$. Therefore

$$\frac{N_{\overline{\nu}_\mu}^{1\mu}}{N_{loc}^{1\mu}} = \frac{0.058 \cdot 0.022 \cdot 0.32 \cdot 0.08 \cdot 0.062 \cdot 0.32}{0.45} = (14 \pm 2 \pm 3) \cdot 10^{-7} \tag{5.20}$$

where the systematic error accounts for the uncertainties of 10% in the flux, 20% in the cross-section, 10% in the fragmentation and 3% in the branching ratio.

The background rate for the neutrino can be written as

$$\frac{N_{\nu}^{1\mu}}{N_{loc}^{1\mu}} = \frac{\phi_{\nu}\sigma_{\nu}^{charm} BR(charm \to h_c) BR(h_c \to \mu^{+} + neutrals) A_{charm}^{1\mu}\eta_{charm}^{1\mu}}{\phi_{\nu}\cdot\sigma_{\nu}^{CC}\cdot A_{CC}^{1\mu}} \tag{5.21}$$

Using simulated samples of 30000 events of background events I obtained $A_{charm}^{1\mu} = 0.335 \pm 0.003$ and $\eta_{charm}^{1\mu} = 0.0011 \pm 0.0005$. Therefore

$$\frac{N_{\nu}^{1\mu}}{N_{loc}^{1\mu}} = \frac{0.05\cdot 0.38\cdot 0.08\cdot 0.335\cdot 0.0011}{0.45} = (1.2 \pm 0.5 \pm 0.3)\cdot 10^{-6} \tag{5.22}$$

where the systematic error accounts for the uncertainties of 20% in the cross-section, 10% in the fragmentation and 3% in the branching ratio.

Both background rates yield an expected number of events on the whole statistics, 140,000 located events, which is less than 0.4 events.

5.4.2 Associated charm production in ν_μ charged and neutral interactions

Slight modifications of the formulas of section 5.3.3 lead to the background rates of associated charm production in the 1μ channel. For associated production in neutral current

$$\begin{aligned}\frac{N_{c\bar{c}}^{CC}}{N_{loc}^{CC}} \sim &\frac{\sigma(\nu_\mu N \to \nu_\mu c\bar{c}X)}{\sigma(\nu_\mu N \to \nu_\mu X)}\frac{\sigma(\nu_\mu N \to \nu_\mu X)}{\sigma(\nu_\mu N \to \mu X)}\cdot BR(c \to D^0)\cdot \\ &BR(\bar{c} \to D^-)\cdot BR(D^- \to \mu^- + neutrals)\cdot \eta_{kink} \sim \\ &4\cdot 10^{-4}\cdot 0.31\cdot 0.12\cdot 0.08\cdot 0.32 \sim 3.8\cdot 10^{-7}\end{aligned} \tag{5.23}$$

where the location efficiency for background and ν_μ CC are assumed roughly equal. For η_{kink} it has been used the value evaluated in events of single charm produced by $\overline{\nu}_\mu$ CC interactions (page 112).

Similarly for associated production in charged current

$$\begin{aligned}\frac{N_{c\bar{c}}^{CC}}{N_{loc}^{CC}} = &\frac{\sigma(\nu_\mu N \to \mu c\bar{c}X)}{\sigma(\nu_\mu N \to \nu_\mu X)}\frac{\sigma(\nu_\mu N \to \nu_\mu X)}{\sigma(\nu_\mu N \to \mu X)}\cdot P(miss\ \mu)\cdot BR(c \to D^0)\cdot BR(\bar{c} \to D^-)\cdot \\ &BR(D^- \to \mu^- + neutrals)\cdot \eta_{kink} < \\ &0.39\cdot 10^{-2}\cdot 0.31\cdot 0.10\cdot 0.12\cdot 0.08\cdot 0.32 \sim 3.7\cdot 10^{-7}\end{aligned} \tag{5.24}$$

Both background rates add to less than $8\cdot 10^{-7}$, yielding less than 0.11 expected events, thus their contribution will be neglected.

5.4.3 Negative kaons and pions produced by ν_μ interactions

A pion or kaon produced in neutral current ν_μ interactions that decay in muon might fake a $\tau^- \to \mu^- \nu_\tau \bar{\nu}_\mu$ decay.

Pions Due to the small mass difference between the π and the muon the $\mathrm{P_t}$ in the decay is about 30 MeV. This $\mathrm{P_t}$ transforms in a kink angle in the laboratory frame $\lesssim 0.03/P(GeV)$ where P if the momentum of the muon. The muon identification, due to the calorimeter presence, is negligible below 1 GeV. Therefore the kink angle in the selected pion decay events is rarely larger than 25 mrad, which is the minimum angle detectable. With the help of a toy Monte Carlo that takes into account the muon identification efficiency, the pion spectra and the cut on the decay length and the smearing in the measurements of the kink angle and of the muon momentum, I have estimated that the fraction of detectable pion decays is less than $1 \cdot 10^{-7}$. This efficiency plus the knowledge of the average number of π^- per NC event (about 1.5) allows to estimate that less than 0.01 events can be detected. This small background will be neglected.

Kaons The kaons decay due to the large mass difference between kaon and muon has a large $\mathrm{P_t}$, about 230 MeV. Therefore the kink angle in the laboratory can be quite large. Using a toy Monte Carlo that takes into account the kaon spectra, the muon identification efficiency as a function of the muon momenta, the muon momentum resolution, the kink angle resolution and the cut on the maximum decay length, it results that the kink angle distribution for the selected events is quite often above the minimum detectable kink angle (see 5.8). Thus on the contrary of the π decay we cannot exclude without further checks some contribution of the K decay at the background. Let's estimate it.

The background rate can be written as

$$\frac{N_K^{CC}}{N_{loc}^{CC}} = \frac{(\sigma(\nu_\mu N \to \nu_\mu X) + \sigma(\nu_\mu N \to \mu X) \cdot P(miss\ \mu))}{\sigma(\nu_\mu N \to \mu X)} \frac{A^{kaon}}{A_{CC}^{1\mu}} \cdot \langle n_k \rangle \cdot BR(K \to \mu) \cdot \eta_{kink}^{kaon} \tag{5.25}$$

where $\langle n_k \rangle$ is the average number of negative kaons per ν_μ events, and A^{kaon} is the location efficiency for the background events. A conservative estimation for $A^{kaon} \cdot \eta_{kink}$ that neglects the inefficiency due to the vertex finding, tracks reconstruction and emulsion follow-down obtained by the toy Monte Carlo gives $\sim 5 \cdot 10^{-7}$. The JETTA event generator gives an average number of negative kaons

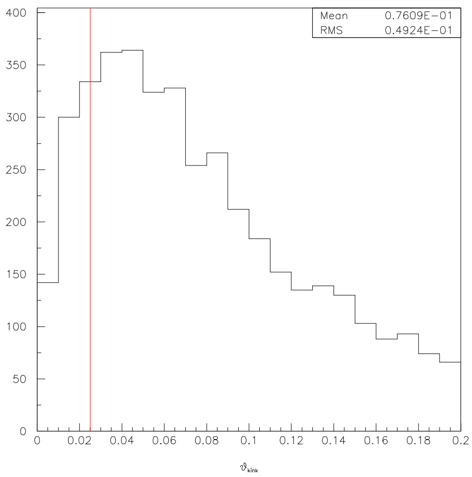

Figure 5.8: Kink angle distribution of $k \to \mu$ decay when the muon is identified and after the decay length cut is applied. The vertical line indicates the minimum value of kink detectable.

per NC event slightly less than 0.1. Therefore the background rate is

$$\frac{N_K^{CC}}{N_{loc}^{CC}} \simeq (0.31 + 1 \cdot 0.2)\frac{5 \cdot 10^{-7}}{0.44} \cdot 0.1 \cdot 0.63 = 4 \cdot 10^{-8} \tag{5.26}$$

which is completely negligible. Let's note that the $\mathrm{P_t}$ cut is very efficient in reducing this background, for instance relaxing the cut from 250 MeV to 100 MeV the kink efficiency increases of about a factor 30: in this case we would have an expected number of background events slightly larger than 0.1.

5.4.4 Wrongly associated primary muon to the hadron track from a charm decay

Let's assume to have a charged charm produced in neutrino charged current interactions that decays in one single charged hadron. This category of events may contribute to the background of the 1μ sample if the primary muon is identified in the calorimeter and/or spectrometer but incorrectly linked, in the target region, to the hadron track produced in the charm decay. Of course this occurrence is rare, but not negligible. In fact due to the large multiple scattering in the calorimeter, the angle and position resolution of the muon track reconstructed in the downstream part of the detector (calorimeter+spectrometer) is not very good. For instance the angular resolution of the calorimeter per projection is shown in figure 5.9. This has forced to set very "tolerant" linking criteria of the

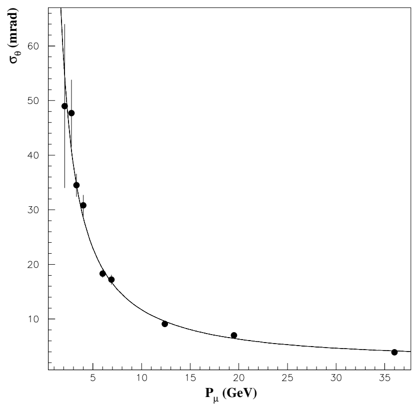

Figure 5.9: Angular resolution per projection of the muon reconstructed in the calorimeter

μ reconstructed in the spectrometer+calorimeter with the tracks reconstructed in the target region. Therefore if the charm hadronic daughter angle is close to the muon (roughly less than 50 mrad) it is possible that, whenever the muon is not reconstructed or simply for resolution effect, the spectrometer+calorimeter muon is linked to the "wrong" target tracker track (see figure 5.10).

The background rate can be written as

$$\frac{N_{\nu}^{1\mu}}{N_{loc}^{1\mu}} = \frac{\phi_{\nu}\sigma_{\nu}^{charm} BR(charm \to h_c) BR(h_c \to h^{+} + neutrals) \cdot A_{charm}^{1\mu} \eta_{charm}^{1\mu}}{\phi_{\nu} \cdot \sigma_{\nu}^{CC} \cdot A_{CC}^{1\mu}} \tag{5.27}$$

Using simulated samples of 60000 CC single charm background events $A_{charm}^{1\mu} = 0.407 \pm 0.002$ and $\eta_{charm}^{1\mu} = (5.2 \pm 1.7) \cdot 10^{-4}$ were obtained. Therefore

$$\frac{N_{\nu}^{1\mu}}{N_{loc}^{1\mu}} = \frac{0.05 \cdot 0.38 \cdot 0.36 \cdot 0.407 \cdot 0.00052}{0.44} = (3.3 \pm 1.1 \pm 0.8) \cdot 10^{-6} \tag{5.28}$$

where the systematic error has been evaluated taking into account 20% of uncertainty in the cross-section, 10% in the charm fragmentation and 5% in the 1-prong branching ratio. Notice that this background rate is quite large if compared with all the previous ones in the 1μ sample.

As a cross check we have tried to estimate the same number in a different way. This will be also useful for the estimate of the background in the next section. We assume that the location efficiency on these charmed events is essentially the same

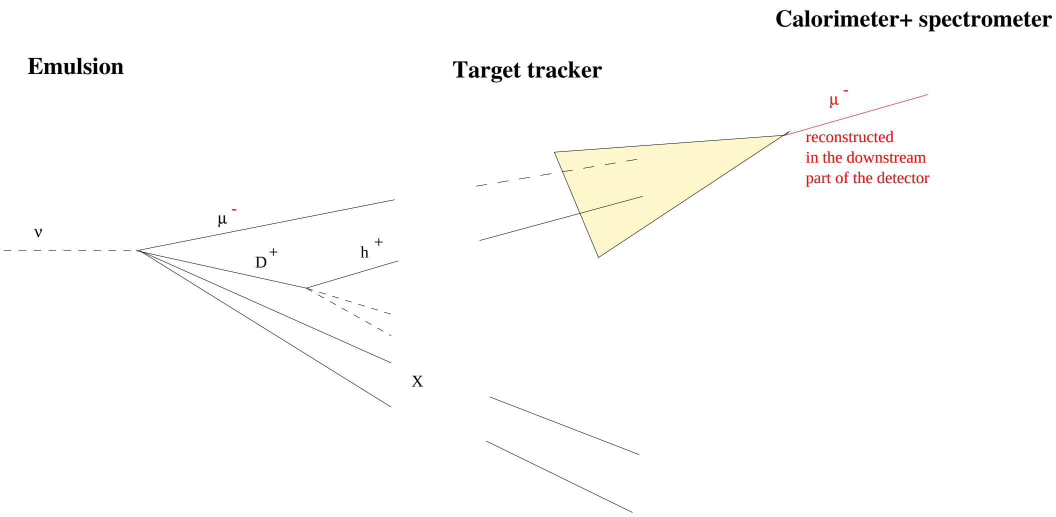

Figure 5.10: A single charm event can contribute to the background of the 1μ if the muon is wrongly associated in the target tracker with the track from the charm decay. The yellow hatched region corresponds to the tolerance in the match of the muon reconstructed in the spectrometer and/or calorimeter with the tracks in the target region. It is visible that both, muon and charm decay tracks, are inside the tolerance. Thus, when the muon track is missed in the target tracker or the charm decay track results, due to resolution, closer than the muon track to the downstream muon extrapolation, it is possible that the charm decay track is incorrectly identified as a muon.

as for CC events, which is reasonable since they are just CC slightly more energetic. $\eta^{1\mu}_{charm}$ can be estimated using the following arguments. Let's assume that at the first order the wrong-match between the muon and an hadron track is almost random, i.e. not strongly correlated with the muon momentum or the charm decay product momentum (see figures 5.11 and 5.12). Under this hypothesis

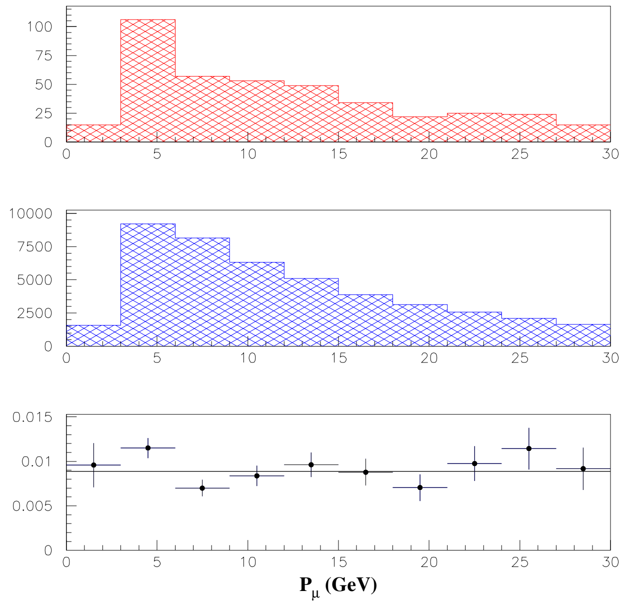

Figure 5.11: **Up panel:** muon momentum for events in which the wrong-match occurs.**Central panel:** muon momentum for events in which the wrong-match doesn't occur. **Bottom panel:** ratio of the muon momentum distribution for events with and without wrong-match.

the wrong-match probability can be equally well evaluated using CC events. It results $(9.2 \pm 0.5) \cdot 10^{-3}$ per event. The average number of target tracker tracks in charm events is about 4. Thus the probability to wrongly match the muon with the charm decay product is about $2.2 \cdot 10^{-3}$.

The efficiency of the kink search method, once we have selected as the scan back track the track produced in the decay, can be assumed to be very similar to $\eta^{1\mu}_{\tau\to\mu}$. Unfortunately the kink efficiency does not contain only the method efficiency, but it must be corrected for the fact that the kink search automatically includes a P_t selection[17]. Therefore the value of the momentum assigned to the scan back

[17] The P_t is limited below by 250 MeV, and above by the 1/P opening angle of the PTS. It

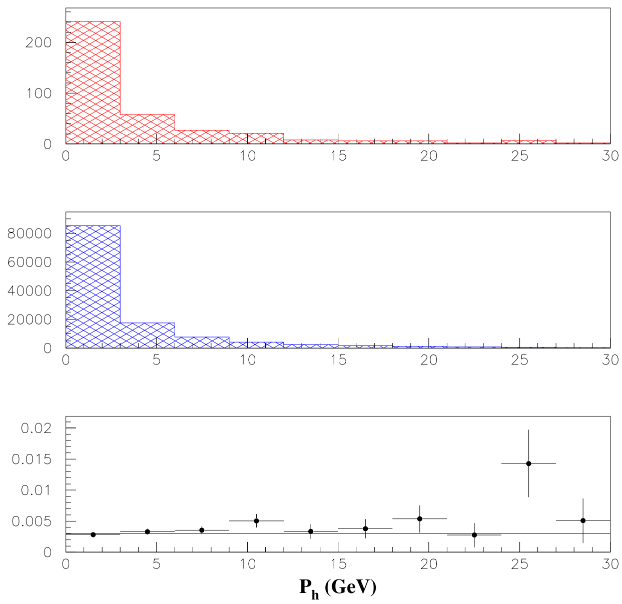

Figure 5.12: **Up panel:** momentum of the hadron track wrong-matched with the muon. **Central panel:** momentum of the hadron tracks when no wrong-match occurs **Bottom panel:** ratio of the hadron momentum distribution for tracks wrong-matched or not with the muon.

track affects the η_{kink}. The correction factor, ϵ_{Pt}, can be estimated comparing the efficiency of the P_t cut for wrongly matched charm events and not wrongly matched ν_τ ones. It can be calculated as the ratio of the fraction of hatched over total areas of the two histograms in figure 5.13. The calculation provides $\epsilon_{Pt} = 0.6$. Therefore the kink efficiency for wrong-matched events can be approximated by

$$\eta = \eta^{1\mu}_{\tau^- \to \mu^- \nu_\tau \bar{\nu}_\mu} \cdot \frac{P(wrong - match)}{\langle N_{tracks} \rangle} \cdot \epsilon_{Pt} = 0.35 \cdot \frac{0.0092}{4} \cdot 0.6 = 4.8 \cdot 10^{-4} \tag{5.29}$$

in good agreement with the results obtained by the full simulation and reconstruction on single charm events, i.e., $(5.2 \pm 1.7) \cdot 10^{-4}$.

translates in a maximum mean P_t detectable of about 2.5 GeV

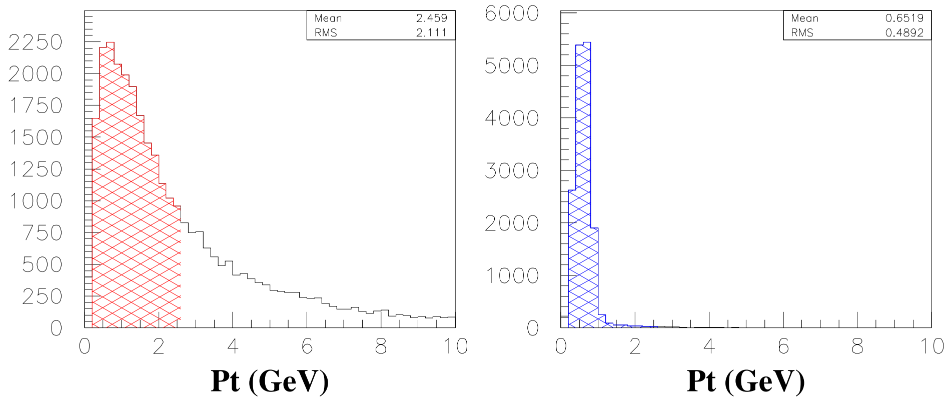

Figure 5.13: **Left panel:** reconstructed P_t of the charm decay in events with a wrong-match. **Right panel:** reconstructed P_t of the $\tau^- \to \mu^- \nu_\tau \bar{\nu}_\mu$ decay. The hatched region correspond to the P_t detectable by the Parent Track Method

5.4.5 Wrongly associated primary muon to a interacting hadron track

Similarly to what described in the previous paragraph a wrongly matched primary muon in CC interactions with an hadron track can constitute background if the hadron undergoes to the interaction without visible recoil in emulsion. A complete simulation of the background has not been possible for technical reasons: about 1 million of CC interaction should have been produced to obtain a significant signal. Fortunately an estimation is possible following the same arguments used at the end of the previous section to test the charm results.

The number of expected background events can be written as

$$\frac{N^{1\mu}_{wsk}}{N^{1\mu}_{loc}} = N_{plate} \cdot L_{plate} \cdot \epsilon_{wrong-match} \cdot \epsilon_{Pt} \cdot \frac{1}{\lambda_{WSK}} \tag{5.30}$$

where N_{plate} is the average number of plates where the kink is searched for in 1μ events. L_{plate} is the plate thickness. ϵ_{Pt} is the correction to be applied to correct for the dependence of the kink efficiency on the reconstructed momentum (see previous paragraph). λ_{WSK} is the interaction length of WSK estimated from data thus automatically including the CHORUS scanning efficiencies. Let's evaluate the rate. The average number of scanned plates if 5.5, the plate thickness is 780 μm. The wrong-match probability as evaluated in the previous paragraph is

$(9.2\pm0.5)\cdot10^{-3}$. The Monte Carlo of WSK described in paragraph 5.3.5 has been used to evaluate ϵ_{Pt}. It results $\epsilon_{Pt} = 5.8 \pm 1.1$ where the error is the systematic due to strong dependence of ϵ_{Pt} on θ_{kink}[18]. The value of λ_{WK} is 23.6 ± 8.4 (see page 111). With all these numbers the background rate results

$$\frac{N^{1\mu}_{wk}}{N^{1\mu}_{loc}} = 5.5 \cdot 0.78 \cdot 10^{-3} \cdot 9.2 \cdot 10^{-3} \cdot 5.8 \cdot \frac{1}{23.6} = 1 \cdot 10^{-5} \pm 0.4 \tag{5.31}$$

The error includes the systematic error of ϵ_{Pt} and the statistical error of λ_{WSK}. Let's note that this background rate is the largest in the 1μ sample. The expected number of events due to it on the whole scanned statistics is 1.4 ± 0.5.

5.5 Background reduction study

All the background rates and the corresponding expected events in the present analysed statistics are reported in tables 5.1 and 5.2.

Source	$N_{bg}/N^{0\mu}_{loc}$	Expected bg events number
Charm in $\overline{\nu}_\mu$ CC	$(3.6 \pm 1.2 \pm 0.9) \cdot 10^{-6}$	$0.073 \pm 0.024 \pm 0.018$
Charm in ν_μ CC	$(3.4 \pm 0.6 \pm 0.8) \cdot 10^{-5}$	$0.69 \pm 0.12 \pm 0.16$
Assoc. charm prod.	$< 3 \cdot 10^{-6}$	neglected
Kaons decay	$\sim 3 \cdot 10^{-7}$	neglected
WSK		2.7 ± 0.8

Table 5.1: Summary of expected background rates and events in the 0μ sample

Source	$N_{bg}/N^{1\mu}_{loc}$	Expected bg events number
Charm in $\overline{\nu}_\mu$ CC	$(14 \pm 2 \pm 3) \cdot 10^{-7}$	$0.20 \pm 0.04 \pm 0.03$
Charm in ν_μ CC	$(1.2 \pm 0.5 \pm 0.3) \cdot 10^{-6}$	$0.16 \pm 0.07 \pm 0.04$
Assoc. charm prod.	$< 8 \cdot 10^{-7}$	neglected
Pions decay	$< 1 \cdot 10^{-7}$	neglected
Kaons decay	$\sim 4 \cdot 10^{-8}$	neglected
Wrongly-ass. charm	$(3.3 \pm 1.1 \pm 0.8) \cdot 10^{-6}$	$0.46 \pm 0.16 \pm 0.11$
Wrongly-ass. WSK	$(1.0 \pm 0.4) \cdot 10^{-5}$	1.4 ± 0.5

Table 5.2: Summary of expected background rates and events in the 1μ sample

[18] It has been estimated augmenting or reducing of a factor two the high θ_{kink} tail.

It is clear that both analysis samples, 0μ and 1μ, are affected by large background if compared to the small number of signal events we are searching for[19]. Therefore it is quite natural to study the possibility to reduce this background without affecting too much the efficiency for the signal, thus to maximize the sensitivity. Since the background sources are quite different for 0μ and 1μ sample, the study has been developed separately.

5.5.1 0μ sample

The largest background source for the τ search in the 0μ sample comes from the WSK events.

The reduction study has been developed exploiting its different kinematic properties with respect to the signal. Two different cuts have been studied. The first consists in a modulation of the maximum allowed flight path for signal as a function of the scan back track momentum. The latter uses the angle in the transverse plane between the τ candidate and the hadronic shower axis.

- **Modulation of the maximum allowed flight path for signal as a function of the hadron momentum.**

In the CHORUS analysis published so far there is a cut on the maximum allowed flight path for τ candidate fixed at 3 emulsion plates for the hadronic decay search [39]. Let's have a look at the plots in figure 5.14. Both plots represent the distance between the primary vertex and the kink point as a function of the momentum of the hadron track that exits from the secondary vertex: one is for WSK events, the other for τ events. Several cuts for each plot are superimposed: the cut at three plates and the three momentum dependent cuts retaining a fixed fraction, 90%, 80% and 70%, of the τ signal. It seems that, using the momentum dependent cuts, there is an increase of the signal/background ratio as can be seen, for instance, by comparing the cut at three plates and the cut at 90% which have a similar efficiency on the signal. This fact is explained by the concomitant of two reasons. The first is that the WSK flight path distribution is almost flat per momentum bin contrarily to the signal events decay length. The second reason is that the WSK events are more concentrated than the τ events in the lower momentum bins.

Five different cuts have been studied correponding to an efficiency on signal of 50%, 60%, 70%, 80% and 90%. The flight path cut values as a function of the

[19] If we assume for the oscillation probability the upper limit of $1 \cdot 10^{-3}$, which is the CHORUS last published result, we expect less than 10 signal events

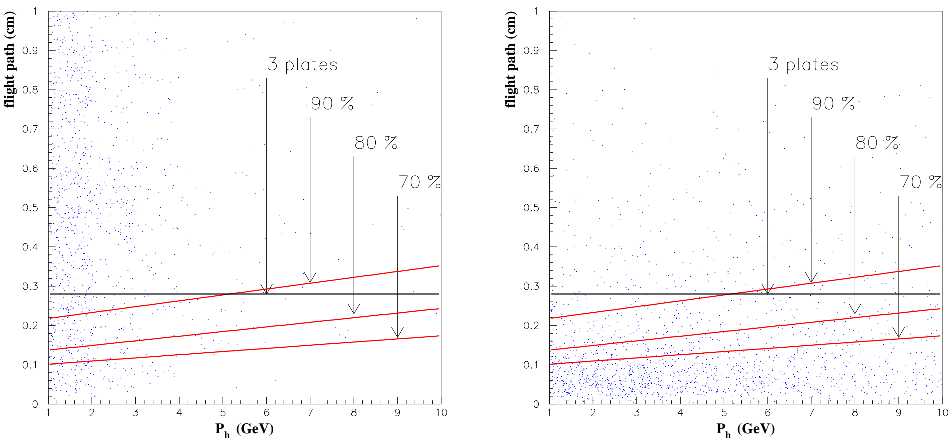

Figure 5.14: Bidimensional plot of the distance between the primary vertex and the kink point as a function of the momentum of the track outgoing from the secondary vertex. The horizontal line represents the three plates cut, the other lines represent cuts that retain a fixed fraction (90%, 80%, 70%) of the signal in each momentum bin. **Left panel:** WSK events. **Right panel:** τ events.

momentum are reported in figure 5.15 where the result of the fit with a straight line is also shown. The efficiency of the cuts on the different background sources are reported in tables 5.3 and 5.4. The decision of which cut to adopt will be discussed in the last chapter.

Events sample	efficiency (%)		
τ in 0μ sample	87.0 ± 0.5	50.0 ± 0.4	60.0 ± 0.4
WSK	22 ± 3	5.2 ± 1.5	7.2 ± 1.5
charm from ν	90^{+10}_{-15}	30 ± 9	50 ± 11
charm from $\overline{\nu}_\mu$	55 ± 25	11 ± 8	11 ± 8

Table 5.3: Efficiency of the flight lenght vs momentum cut.

- **Angle between the τ candidate and the the hadronic shower axis.**

Another variable that can be used to separate background from signal is the angle in the plane orthogonal to the neutrino incoming direction between the τ candidate track momentum and the hadronic shower axis. In fact for signal events, the τ is emitted back to back to the hadronic shower, compatibly with the Fermi motion,

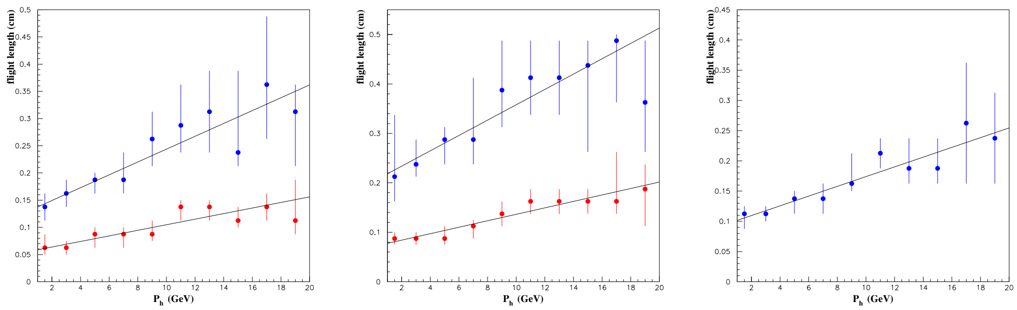

Figure 5.15: Flight path versus momentum cut for different efficiency values on signal. **Left panel:** 80% and 50%. **Central panel:** 90% and 60%. **Right panel:** 70%.

Events sample	efficiency (%)		
τ in 0μ sample	70.0 ± 0.4	80.0 ± 0.5	90.0 ± 0.5
WSK	7.2 ± 1.5	15 ± 3	20 ± 3
charm from ν	60 ± 16	60 ± 16	85 ± 15
charm from $\overline{\nu}_\mu$	33 ± 19	55 ± 25	80^{+12}_{-30}

Table 5.4: Efficiency of the flight lenght vs momentum cut.

and we expect the ϕ angle to be close to 180°. On the contrary for background events, WSK or charm decays, the particle with the kink is part of the hadronic shower, thus a ϕ angle closer to 0° is expected (see figure 5.16).

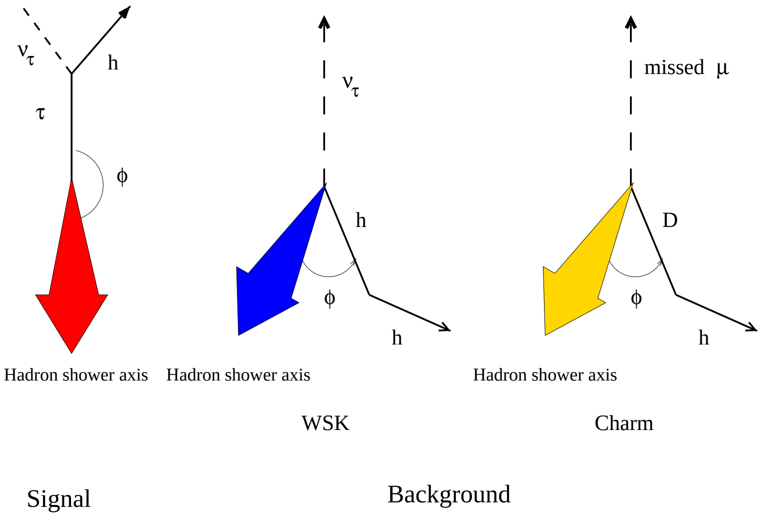

Figure 5.16: ϕ angle for signal and background events.

In figure 5.17 are reported the reconstructed ϕ angle distributions for signal and WSK background events. The distribution for signal is visibly peaked at 180°, while the background distribution is flatter. The main contribution at the smearing of this distribution comes from the uncertainty in the hadronic shower direction determination due largely to the limited geometrical acceptance of the calorimeter.

The studied cut consists in rejecting all the events with a ϕ angle smaller than 90°. The efficiency of this cut on the various samples evaluated from Monte Carlo are reported in table 5.5

Events sample	efficiency (%)
τ events in the 0μ sample	80.9 ± 0.8
WSK	46.5 ± 4.2
charm from ν	40 ± 10
charm from $\overline{\nu}_\mu$	44 ± 13

Table 5.5: Efficiency of the ϕ cut.

Let's note that the ϕ distribution expected for WSK events well matches the

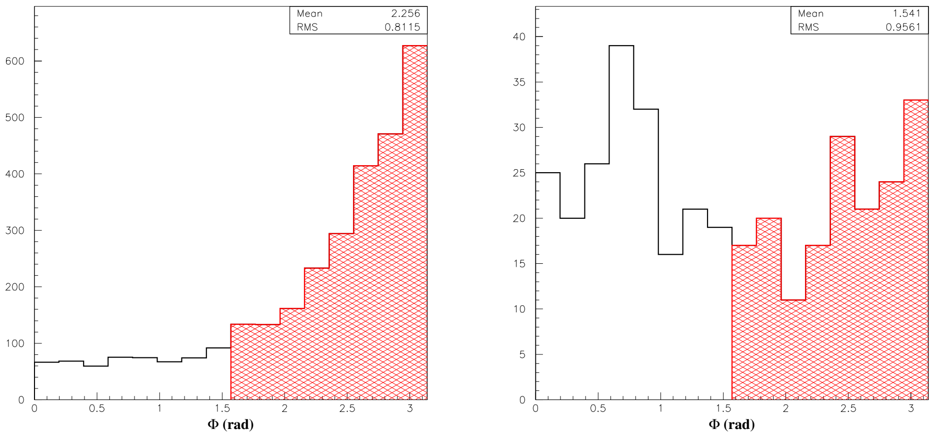

Figure 5.17: Distribution of the reconstructed value of ϕ angle. The hatched region corresponds to the events that survive to cut appliance. **Left panel:** τ decays events reconstructed in the 0μ sample. **Right panel:** WSK events.

distribution obtained for the kink events found in the reference region, giving a further test of the reliability of the WSK Monte Carlo simulation (fig 5.18). The application of this cut, as the previous one, will be decided in the next chapter.

5.5.2 1μ sample

The largest background source to the search of the τ decays classified as 1μ comes from ν_μ CC events where the primary muon is wrongly associated to an hadron track either produced in a charm decay or that undergoes to a WSK interaction. Since the wrong association occurs because the muon and the hadron track are close in space it is natural to search for a reduction criteria based on the nearness of the emulsion tracks with the muon identified in the electronic detector (see figure 5.10).

The algorithm studied is the following. After the event has been scanned and a kink has been detected on the muon track, the neutrino vertex is analysed and all the emulsion tracks outcoming from it are stored. Then for each emulsion track, except the one with the kink, the angular distance with the muon is evaluated. The distribution of the angular distance of the closest track for background and $\tau^- \to \mu^-\nu_\tau\bar{\nu}_\mu$ signal events is depicted in figure 5.19. The two distributions are so different that a simple cut that rejects all the events with an angular distance

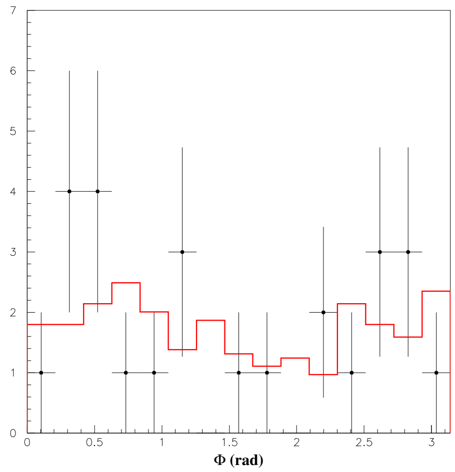

Figure 5.18: ϕ angle distribution for kink events found in the reference region (points) and the expected one from WSK simulation

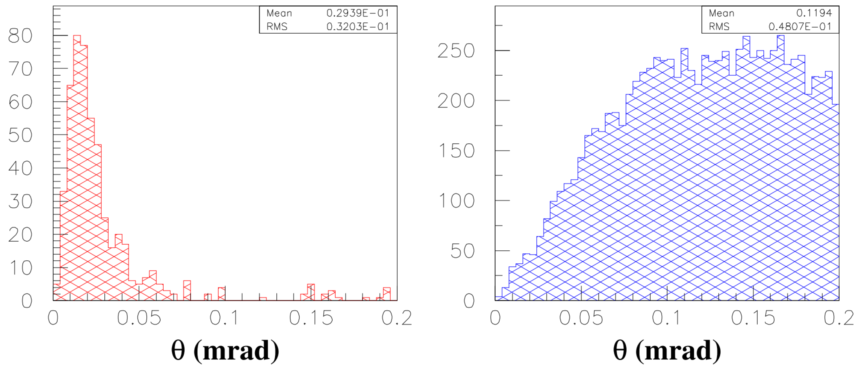

Figure 5.19: Distribution of the angular distance between the muon reconstructed in the electronic detector and the primary vertex track closest to it (except the one with the kink). **Right panel:** Background events. **Left panel:** signal events

less than a fixed value is very efficient in increasing the signal to noise ratio. In figure 5.20 the cut rejection power on the background and the inefficiency introduced on the signal are reported. This cut is so powerful in increasing the signal to noise ratio that it was applied without further studies on alternative cuts. The cut has been fixed maximizing the quantity signal/$\sqrt{\text{signal} + \text{noise}}$ for an oscillation probability of $1 \cdot 10^{-3}$ [39]. The minimum has been found for the cut value of 46 mrad. With the choosen cut results that the fraction of wrong-matched events

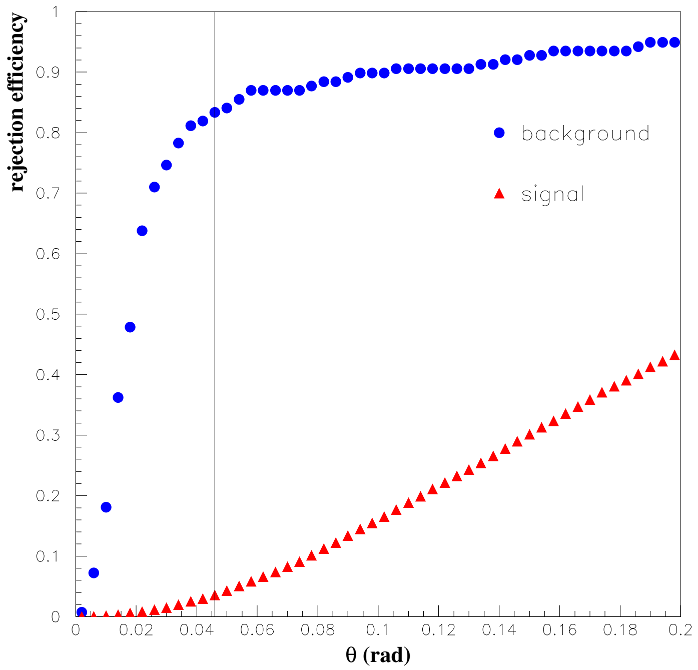

Figure 5.20: Rejection power on the background and inefficiency introduced on the signal as a function of the cut value. The line represents the choosen cut value.

rejected is

$$\epsilon^{bg}_{\text{cut } 1\mu} = 83.3 \pm 7.7\% \tag{5.32}$$

while for signal we loose only

$$\epsilon^{\tau}_{\text{cut } 1\mu} = 3.6 \pm 1.3\%. \tag{5.33}$$

Chapter 6

Results of the $\nu_\mu \rightarrow \nu_\tau$ oscillation search

In this chapter the numbers evaluated in the previous chapters, efficiencies and background expectations, will be combined with the information coming from the scanning laboratories, analysed statistics and found candidates, to determine the result of the CHORUS oscillation search.

At the end of chapter 3 it was shown that to obtain a determination of the oscillation probability we could use the formula

$$P(\nu_\mu \rightarrow \nu_\tau) = \frac{N_\tau^{obs}}{\mathrm{N}_{\nu_\tau}^{\max}} \tag{6.1}$$

where N_τ^{obs} is the number of observed τ candidates and $\mathrm{N}_{\nu_\tau}^{\max}$ is the number of ν_τ events that we would observe if all the incident ν_μ had converted in ν_τ. Therefore to evaluate the CHORUS result of $\nu_\mu \rightarrow \nu_\tau$ oscillation search we proceed in the following way:

- first we evaluate the normalization sample, i.e. $\mathrm{N}_{\nu_\tau}^{\max}$
- then using the information of $\mathrm{N}_{\nu_\tau}^{\max}$ and its uncertainty we define the background reduction strategy for the 0μ selected events, i.e. we have to search the combination of cuts studied in the previous chapter that maximizes the CHORUS sensitivity
- at this point we are ready to "open the box" and look if, at the end of the analysis, there are some ν_τ candidates. This information, combined with $\mathrm{N}_{\nu_\tau}^{\max}$, will lead us directly to the evaluation of the oscillation probability.

6.1 Evaluation of the normalization factor

$\mathrm{N}^{\mathrm{max}}_{\nu_\tau}$, the quantity we need as normalization factor in the probability evaluation, can be calculated using the formula

$$\mathrm{N}^{\mathrm{max}}_{\nu_\tau} = \mathrm{N}^{\mathrm{max}}_{\nu_\tau}(1\mu) + \mathrm{N}^{\mathrm{max}}_{\nu_\tau}(0\mu) \tag{6.2}$$

where $\mathrm{N}^{\mathrm{max}}_{\nu_\tau}(1\mu)$ and $\mathrm{N}^{\mathrm{max}}_{\nu_\tau}(0\mu)$ correspond to the ν_τ events that we would observe in the 1μ and 0μ sample respectively. They can be written as

$$\mathrm{N}^{\mathrm{max}}_{\nu_\tau}(1\mu) = \mathrm{N}^{\mathrm{loc}}_{\nu_\mu}(1\mu) \times \left[\frac{\langle \sigma^{CC}_\tau \rangle \left\langle A^{1\mu}_{\tau^- \rightarrow \mu^- \nu_\tau \bar{\nu}_\mu} \right\rangle \left\langle \eta^{1\mu}_{\tau^- \rightarrow \mu^- \nu_\tau \bar{\nu}_\mu} \right\rangle BR(\tau^- \rightarrow \mu^- \nu_\tau \bar{\nu}_\mu)}{\langle \sigma^{CC}_\mu \rangle \left\langle A^{1\mu}_{CC} \right\rangle} \right] \tag{6.3}$$

and

$$\begin{aligned} \mathrm{N}^{\mathrm{max}}_{\nu_\tau}(0\mu) = {} & \mathrm{N}^{\mathrm{loc}}_{\nu_\mu}(0\mu) \times \frac{1}{\langle \sigma^{CC}_\mu \rangle \left\langle A^{0\mu}_{CC} \right\rangle + \langle \sigma^{NC}_\mu \rangle \langle A_{NC} \rangle} \cdot \\ & \langle \sigma^{CC}_\tau \rangle \Big[\left\langle A^{0\mu}_{\tau^- \rightarrow \mu^- \nu_\tau \bar{\nu}_\mu} \right\rangle \left\langle \eta^{0\mu}_{\tau^- \rightarrow \mu^- \nu_\tau \bar{\nu}_\mu} \right\rangle BR(\tau^- \rightarrow \mu^- \nu_\tau \bar{\nu}_\mu) + \\ & \left\langle A_{\tau^- \rightarrow \mathrm{h}^- (n\pi^0) \nu_\tau} \right\rangle \left\langle \eta_{\tau^- \rightarrow \mathrm{h}^- (n\pi^0) \nu_\tau} \right\rangle BR(\tau^- \rightarrow \mathrm{h}^- (n\pi^0) \nu_\tau) + \\ & \langle A_{\tau^- \rightarrow e^- \nu_\tau \bar{\nu}_e} \rangle \langle \eta_{\tau^- \rightarrow e^- \nu_\tau \bar{\nu}_e} \rangle BR(\tau^- \rightarrow e^- \nu_\tau \bar{\nu}_e) \Big] \end{aligned} \tag{6.4}$$

where $\mathrm{N}^{\mathrm{loc}}_{\nu_\mu}(1\mu)$ and $\mathrm{N}^{\mathrm{loc}}_{\nu_\mu}(0\mu)$ are the number of ν_μ located events in 1μ and 0μ samples. This way of writing the $\mathrm{N}^{\mathrm{max}}_{\nu_\tau}$ has the advantage to reduce the systematic error on the Monte Carlo efficiency evaluation connected to the scan back selection. In fact the scan back track is identified by the same detector (hexagonal magnet or muon spectrometer) for both simulated sample of events that appear in the ratio.

To evaluate $\mathrm{N}^{\mathrm{max}}_{\nu_\tau}(1\mu)$ and $\mathrm{N}^{\mathrm{max}}_{\nu_\tau}(0\mu)$ we need:

- the number of located events
- the average cross-sections
- the efficiencies

Number of located events

All the CHORUS analysis flow is reported in table 6.1. Unfortunately to evaluate the number of located events we cannot just add the corresponding entries of each year.

	1994	1995	1996	1997	Total
Protons on target/10^{19}	0.81	1.20	1.38	1.67	5.06
Emulsiontriggers/10^3	422	547	617	719	2305
0μ sample					
events reconstructed and vertex predicted in emulsion	56111	77443	95751	106093	335398
events with at least 1 selected negative track	19846	29350	37143	36073	122412
events scanned so far	13047	17859	29773	24532	85211
vertex located (in the 33 most upstream plates)	3024	4424	8704	7054	23206
1μ sample					
events reconstructed and vertex predicted in emulsion	96995	168668	209136	238552	713351
events with at least 1 negative muon	66309	112943	139077	159296	477625
events scanned so far	50025	62568	114923	127879	355395
vertex located in the 33 most upstream plates	20400	21610	44867	56865	143742

Table 6.1: Analysis statistics flow, from proton on target to located event.

In fact during the processing of 95 data and about 86% of 96 data a mistake was done. It affects the momentum reconstruction of the hadron tracks and one of its consequences is that a part of the 0μ tracks was erroneously selected for the scan back. To correct for this mistake we have to decrease the number of 95 and 96 0μ located events. A more detailed explanation of the effect of the mistake and of its consequences can be found in the appendix. In the appendix there is also the evaluation of the correction factor to be applied on located events. The number of 0μ located events, after the correction, is reported in table 6.2. In the same table also the 1μ located events are reported.

	1994	1995	1996	1997
0-μ: loc. ev.	3024	2588	7659	7054
1-μ: loc. ev.	3394+16545^a+461^b	21610	44450+417^b	54992+1873^b

Table 6.2: Corrected located events number. The events with superscript have been scanned with different techniques from the one for which, in this thesis, the efficiencies have been evaluated.

Cross-sections

The events generators used by the CHORUS collaboration gives for ν_τ and ν_μ the energy dependent CC cross section reported in figure 6.1. Folding the cross-section on the neutrino flux it results that:

$$\frac{\langle \sigma_\tau^{CC} \rangle}{\langle \sigma_\mu^{CC} \rangle} = 0.53 \tag{6.5}$$

Note that using the same distributions we can evaluate

$$\frac{\langle \sigma_\tau^{QE} \rangle}{\langle \sigma_\tau^{DIS} \rangle} = 0.135 \tag{6.6}$$

and

$$\frac{\langle \sigma_\mu^{QE} \rangle}{\langle \sigma_\mu^{DIS} \rangle} = 0.085 \tag{6.7}$$

whereas from literature the ratio of NC over CC DIS cross section results [40, 41, 42]

$$\frac{\langle \sigma_\mu^{NC} \rangle}{\langle \sigma_\mu^{CC} \rangle} = 0.31 \tag{6.8}$$

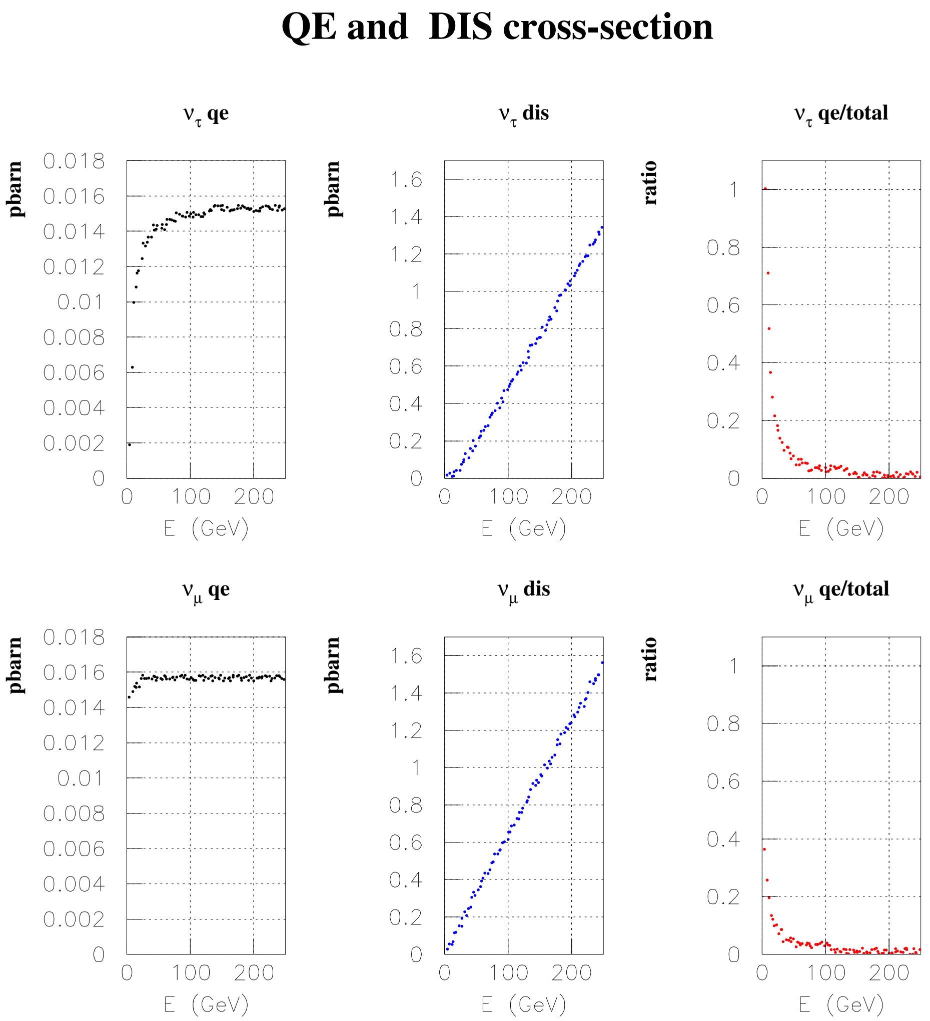

Figure 6.1: Cross-section for charged current interactions of ν_τ (top plots) and ν_μ (bottom plots). The left plots are the cross-sections for QE and resonance production. The central plots correspond to the DIS events production cross-section and the right represent the fraction of QE+resonance on the total cross-section.

all these ratios will be useful in the following.

Efficiencies

The efficiencies are reported in table 6.3. They are evaluated combining

- the efficiencies values reported separately for QE and DIS in tables 4.1, 4.2, 4.3, 4.4, 4.5, 4.6 and 4.7
- the QE/DIS ratios reported above
- the correction due to Monte Carlo-data disagreement reported in table 4.10
- the η_{kink} correction factors in formula 4.15
- the correction reported in appendix due to 95-96 processing error
- the fraction of events to which the SVSB kink search method is applied

		1994	1995	1996	1997
$A^{1\mu}_{CC}$	(%)	45.0 ± 0.5	45.0 ± 0.5	45.0 ± 0.5	45.0 ± 0.5
A_{NC}	(%)	20.3 ± 0.5	11.9 ± 0.3	17.8 ± 0.5	16.2 ± 0.5
$A^{0\mu}_{CC}$	(%)	5.2 ± 0.9	2.4 ± 0.4	5.1 ± 0.8	4.2 ± 0.7
$A^{1\mu}_{\tau^- \to \mu^- \nu_\tau \bar{\nu}_\mu}$	(%)	43.5 ± 0.5	43.5 ± 0.5	43.5 ± 0.5	43.5 ± 0.5
$A^{0\mu}_{\tau^- \to \mu^- \nu_\tau \bar{\nu}_\mu}$	(%)	7.4 ± 1.0	3.2 ± 0.5	6.4 ± 0.9	6.2 ± 0.9
$A_{\tau^- \to e^- \nu_\tau \bar{\nu}_e}$	(%)	28.5 ± 0.7	12.3 ± 0.3	24.1 ± 0.6	24.0 ± 0.6
$A_{\tau^- \to \mathrm{h}^- (n\pi^0) \nu_\tau}$	(%)	36.1 ± 0.4	16.3 ± 0.2	30.7 ± 0.3	30.3 ± 0.5
$\eta^{1\mu}_{\tau^- \to \mu^- \nu_\tau \bar{\nu}_\mu}$	(%)	31.7 ± 0.5	34.1 ± 0.5	34.4 ± 0.5	34.3 ± 0.5
$\eta^{0\mu}_{\tau^- \to \mu^- \nu_\tau \bar{\nu}_\mu}$	(%)	12.5 ± 2.2	8.8 ± 1.5	14.3 ± 2.5	10.9 ± 2.0
$\eta_{\tau^- \to \mathrm{h}^- (n\pi^0) \nu_\tau}$	(%)	13.8 ± 0.4	12.1 ± 0.4	14.6 ± 0.4	11.0 ± 0.6
$\eta_{\tau^- \to e^- \nu_\tau \bar{\nu}_e}$	(%)	5.9 ± 0.6	5.0 ± 0.5	6.3 ± 0.6	4.6 ± 0.5

Table 6.3: Efficiencies averaged over DIS and QE cross-section, corrected for Monte Carlo and data disagreement and for the mistake in the 95-96 data processing.

Combining the efficiencies with the number of located events, the cross-sections and the τ branching ratios the number of $\mathrm{N}^{\mathrm{max}}_{\nu_\tau}(0\mu)$ and $\mathrm{N}^{\mathrm{max}}_{\nu_\tau}(1\mu)$ are obtained. Let's note that part of the 1μ sample has been scanned with different techniques from the ones whose efficiencies have been evaluated within this thesis. The 1μ located events with superscript 'a' have been scanned using the technique described at page 62 [43]. The events with superscript "b" have been scanned with

	1994	1995	1996	1997	Total
$\mathrm{N}_{\nu_\tau}^{\max}(1\mu)$	96	656	1363	1679	3794
$\mathrm{N}_{\nu_\tau}^{\max}(0\mu)$ from $\tau^- \to \mathrm{h}^-(n\pi^0)\nu_\tau$	358	230	887	697	2172
$\mathrm{N}_{\nu_\tau}^{\max}(0\mu)$ from $\tau^- \to e^-\nu_\tau\bar{\nu}_e$	43	25	107	83	258
$\mathrm{N}_{\nu_\tau}^{\max}(0\mu)$ from $\tau^- \to \mu^-\nu_\tau\bar{\nu}_\mu$	24	12	63	50	149

Table 6.4: $\mathrm{N}_{\nu_\tau}^{\max}(1\mu)$ and $\mathrm{N}_{\nu_\tau}^{\max}(0\mu)$ corresponding to the events scanned with the technique for which the efficiencies have been calculated in this thesis.

a completely different technique from the one described in chapter 3 [44]. The contribution of these events at $\mathrm{N}_{\nu_\tau}^{\max}(1\mu)$, not evaluated in this thesis, is reported in table 6.5 [38].

	1994	1995	1996	1997	Total
$\mathrm{N}_{\nu_\tau}^{\max}(1\mu)$	883 +21	0	19	85	1008

Table 6.5: $\mathrm{N}_{\nu_\tau}^{\max}(1\mu)$ corresponding to the events scanned using different techniques from the one for which the efficiencies have been calculated (see table 6.2)

The errors included in the efficiencies are only statistical. They are quite small. Instead the systematic errors on $\mathrm{N}_{\nu_\tau}^{\max}(1\mu)$ and $\mathrm{N}_{\nu_\tau}^{\max}(0\mu)$ is estimated to be larger. It amounts to about 15% for $\mathrm{N}_{\nu_\tau}^{\max}(1\mu)$ and 20% for $\mathrm{N}_{\nu_\tau}^{\max}(0\mu)$. This evaluation of the systematic uncertainties assumes as possible sources of systematic errors the event generator and the kink efficiency. The error due to the generator has been assumed to be about 6% which is the spread of the results obtained using two different sets of structure functions. The error on η_{kink} is derived by an experimental check. A partial test of the η_{kink} value has been carried out by studying multi-prong hadron interaction detected during the τ search. A Monte Carlo simulation predicts 84 events, while 80 events were detected. This gives an error of about 11%. Since the τ decay and hadron multi-prong interaction topologies have some differences and moreover the test is sensitive only to the geometrical part of η_{kink} and not to the $\mathrm{P_t}$ dependent part, the error has been conservatively increased. A total systematic of 15% for $\mathrm{N}_{\nu_\tau}^{\max}(1\mu)$ has been assumed. The error on $\mathrm{N}_{\nu_\tau}^{\max}(0\mu)$ has been conservatively enlarged to 20% to take into account the possible error in the hadron momentum reconstruction[20].

[20]Let's remind that the hexagonal magnet momentum resolution has been tested using muon

6.2 0μ background rejection optimization

As discussed in the previous chapter the background rate in the 0μ sample is not negligible, about three events are expected. Two possible reduction cuts have been studied but the decision to apply them or not was postponed. In fact, although the cuts reduce sizeable the background, their impact on the signal is not quite negligible. We have followed the criteria to define the optimum cut as the one that maximize the sensitivity and now we have all the elements to do that. In our case the sensitivity is defined as the average upper limit that we would obtain repeating infinite times the experiment in case of no expected signal. To compute the upper limit the method proposed by Junk is used [45]. It allows the combination of different independent searches of the same signal, 1μ and 0μ in our case, moreover it incorporates also the effect of the uncertainty in the signal and background model.

From all the possible background reduction strategy the one that maximizes the sensitivity results to be the combination of the ϕ cut plus the flight length versus momentum cut that retain the 80% of the signal.

6.3 Oscillation probability evaluation

Now that all the analysis strategy is defined it is time to look if ν_τ candidates have been found. The results are reported in table 6.6. With the chosen analysis no ν_τ candidates survived at the end.

Further test of the the lack of any evidence of ν_τ interactions comes from table 6.7 where the expected background and found events are reported as a function of the different cuts. In each case the number of found candidates agrees well with the expected background.

Since no ν_τ candidates have been found an upper limit on $\nu_\mu \to \nu_\tau$ oscillation probability can be evaluated. According to the statistical treatment followed to optimize the cuts, the upper limit on the number of τ decays at 90% of C.L. is

on ν_μ CC events. No measurements for hadrons are available. We expect that possible differences between hadron and muon might arise principally from patter recognition error due to the different isolation of the muon and hadron track. Since the hadron track in τ decay has an isolation similar to the μ in ν_μ CC events no large discrepancies are expected, but anyhow to be conservative an enlargement of the error has been applied. Moreover all the corrections due to mistake in 95 and 96 processing introduces other error source.

1μ sample		
Cut	expected	found
3 plates + $P_t > 250$ MeV + $\theta > 0.046 rad$	0.65 ± 0.11	0
0μ sample		
80% + ϕ+ $P_t > 250$ MeV	1.1 ± 0.3	0

Table 6.6: The expected background events and the observed number of candidates at the end of the post-scanning analysis.

1μ sample		
Cut	expected	found
3 plates + $P_t > 250$ MeV	2.2 ± 0.6	2
3 plates + $P_t > 250$ MeV + $\theta > 0.046 rad$	0.65 ± 0.11	0
0μ sample		
3plates + $P_t > 250$ MeV	3.5 ± 0.8	4
3plates +ϕ + $P_t > 250$ MeV	1.6 ± 0.4	2
80% + $P_t > 250$ MeV	2.4 ± 0.6	1
80% + ϕ+ $P_t > 250$ MeV	1.1 ± 0.3	0
90% + $P_t > 250$ MeV	3.2 ± 0.8	6
90% + ϕ+ $P_t > 250$ MeV	1.4 ± 0.4	2
70% + $P_t > 250$ MeV	1.4 ± 0.3	1
70% + ϕ+ $P_t > 250$ MeV	0.6 ± 0.1	0

Table 6.7: The expected background events are compared with the observed number of candidates for different cuts.

2.34. $\mathrm{N}_{\nu_\tau}^{\max}$ after the application of the cuts is

$$\begin{aligned}\mathrm{N}_{\nu_\tau}^{\max} &= \mathrm{N}_{\nu_\tau}^{\max}(1\mu)\cdot(1-\epsilon_{\text{cut }1\mu}^{\tau}) + \mathrm{N}_{\nu_\tau}^{\max}(0\mu)\cdot\epsilon_\phi\cdot\epsilon_{flight\ length} = \\ &= 4802\cdot 0.964 + 2579\cdot 0.809\cdot 0.92 = \\ &= 6547\end{aligned} \tag{6.9}$$

Thus from formula 6.1 we derive that the upper limit at 90% of C.L. on the probability is

$$\mathrm{P}(\nu_\mu \to \nu_\tau) \leq 3.6\cdot 10^{-4}. \tag{6.10}$$

If we assume the two-generations oscillation scheme, the oscillation probability can be written as

$$\mathrm{P}(\nu_\mu \to \nu_\tau) = \sin^2 2\theta_{\mu\tau}\cdot\sin^2(\frac{1.267\Delta m^2 L}{E}) \tag{6.11}$$

which, for large Δm^2, simplifies to

$$\mathrm{P}(\nu_\mu \to \nu_\tau) = \sin^2 2\theta_{\mu\tau}\cdot\frac{1}{2}. \tag{6.12}$$

Thus the upper limit on probability corresponds to an upper limit on the mixing angle

$$\sin^2 2\theta_{\mu\tau} \leq 7.2\cdot 10^{-4}. \tag{6.13}$$

The full analysis chain efficiencies for 1μ and 0μ as a function of the neutrino energy are reported in figure 6.2. Both show a decrease of efficiency at high value of neutrino energy. This is mainly due to the momentum cut applied on the scan back selection and to the scanning method that rejects too small kink angle. Folding these efficiencies with the energy dependent cross-section and neutrino flux the exclusion plot in the $(\sin^2 2\theta_{\mu\tau}, \Delta m^2)$ parameter space has been derived (fig 6.3).

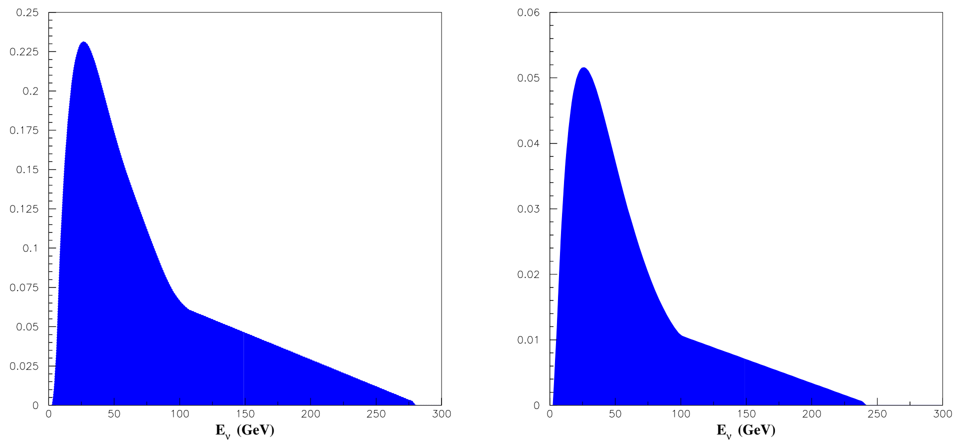

Figure 6.2: The full analysis chain efficiencies as a function of the neutrino energy. **Left panel:** for the ν_τ search in 1μ sample. **Right panel:** for the ν_τ search in 0μ sample.

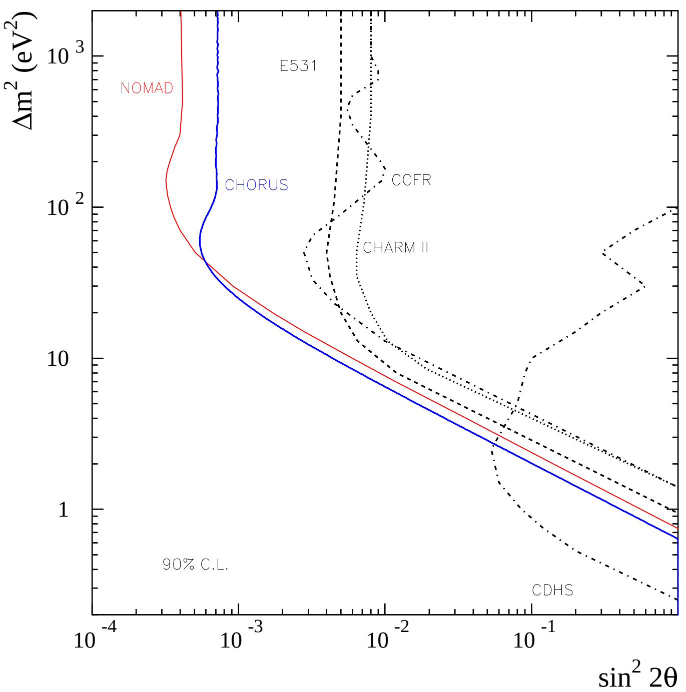

Figure 6.3: The CHORUS exclusion plot corresponding to $P(\nu_\mu \to \nu_\tau) \leq 3.6 \cdot 10^{-4}$ at 90% of C.L.

Appendix A

Corrections due to mistakes in the off-line processing

During the processing of part of CHORUS data (95&96 data) two bugs were inserted in the hadron momentum reconstruction program. Time after the completion of the processing the error was discovered. Unfortunately at that time a large part of the automated scanning was already finished. Moreover the complete reprocessing would have taken so long time that in the meantime all the predicted events would have been scanned. This fact, together with the observation that, despite of the bug, part of the "old" predictions were usable, has led to the decision to not stop the scanning and to use the old (bugged) predictions for the analysis. For a subsample of events predictions have been produced with a "corrected" version of the off-line reconstruction program and employed to compute factors to be applied statistically to the scanned data as it will be explained in the following.

Prior to decide how to use the "corrupted" data let's give some brief information on the bugs to understand their effects. The bugs that affected the 95 and 96 data productions were different. In the processing of 95 data an obsolete set of the diamond tracker geometry alignment constants were used. In the processing of the affected fraction of 96 data (about 86%) the problem was due to a wrong setting of a parameter. It is used to decide in the momentum tracker fit when a hit of the diamond tracker planes belongs or not to a track. It was set to a value much smaller than the right value. This has the effect to disconnect hits that really belong to the track. In the case where not enough reliable hits in the tracker planes were assigned to the track, the recovery procedure in the fit tries to use the hits of the streamer tubes in front of the calorimeter to get a momentum estimation. The problem in using the streamer tube hits, which in bug-free version are used essentially to validate the track and not for the momentum fit, is their resolution. Indeed the tube width is 1cm which is large compared to the deviation induced by the magnet field: a track with 1GeV momentum deviates in the bending plane of 1cm.

Summarizing both bugs, although different, affected the momentum fit evaluated using the hexagonal trackers. Since this momentum fit is used to select inside the 0μ sample the negative hadron tracks to be scanned, the effect of the bug was essentially to modify the prediction tracks set. Schematically what happened is depicted in figure A.1. C is the sample of tracks that both predictions versions (bugged and corrected) reconstruct as negative with momentum in the range 1-20 GeV. B is the set of tracks that resulted with negative momentum between 1 and 20 GeV with the bugged program, but they are either positive or not fitted at all by the new version. Vice versa A is the set of tracks that now result negative with momentum less than 20 and greater than 1 GeV, but they resulted positive or not fitted by means of the bugged program. Concluding, since the sample of tracks scanned is B+C, but the correct sample is A+C, we have scanned only a part of the right predictions, C, but we scanned also uselessly the set B.

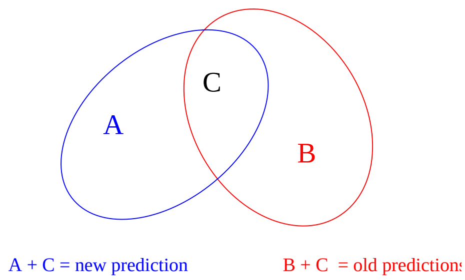

Figure A.1: The scanned predictions set corresponds to B+C, while the sample we should have scanned if the no bug wasn't there is A+C.

Unfortunately it isn't easy to evaluate the effect of the bugs using the montecarlo. The montecarlo simulation of the detector doesn't include the misalignment problem, every subdetector is assumed to be perfectly aligned with all the rest. It was decided to evaluate the effect using the data themselves. Moreover, since as seen in chapter 3.2.4 the montecarlo doesn't reproduce perfectly the fit resolution, it is quite doubtful that it would reproduce correctly the effect of the bugs on the fit resolution.

The first step is to evaluate the number of located events which were scanned in vain because all their scanback tracks fall in category B. Then we need to evaluate the new location and kink efficiency for event with at least a track in the sample C. In fact, although the location procedure is independent of the momentum of the track after it has been selected, the kink efficiency is not. In fact during the kink search the momentum value is used (see page 63).

Crossing event by event all the tracks and assuming that a track in old prediction and in new prediction are the same if their angular difference is less than 15 mrad (the angular criteria used in CS scanning), we can easily evaluated ϵ_{red}, the fraction of the bugged predicted events scanned in vain. In the same way it is possible to evaluate $\epsilon_{old/new}(p)$, defined as the probability that a track having the negative momentum in the range 1-20 GeV according to the new predictions, it had the momentum in the same range also for the old prediction. Moreover it is possible in bin of "new" momentum to observe the distribution of the "old" momentum. The plots of $\epsilon_{old/new}(p)$ for the two years are reported in figure A.2.

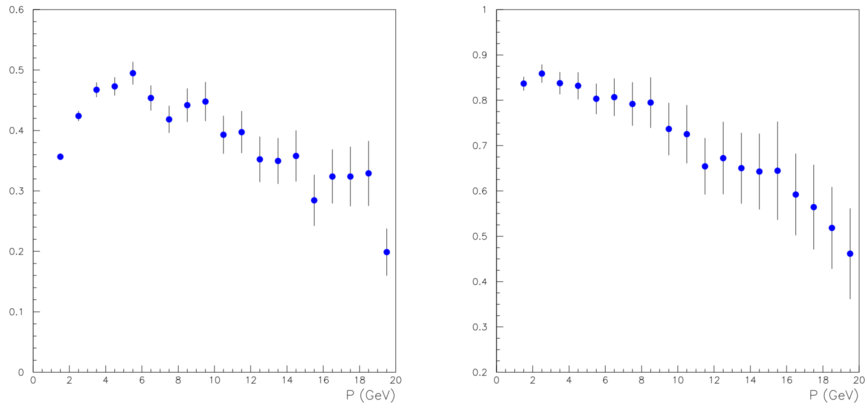

Figure A.2: Probability as a function of momentum that a track selected as scan back by means of the corrected version was selected also by the bugged version. Left: 95 data. Right: 96 data.

Using all these information and the montecarlo it was possible to evaluate the correction of the location and kink efficiency in the following way. Event by event each track with reconstructed negative momentum between 1 and 20 GeV was assumed to be reconstructed also by the bugged program in the same momentum range with a probability equals to $\epsilon_{old/new}(p)$. A "bugged" momentum is assigned to the track according to the distributions $P_{old} vs. P_{new}$ (for two examples of these distributions see fig A.3 and A.4). Then all the scanning was simulated using the "bugged" momentum value. At the end to evaluate the Pt cut the montecarlo reconstructed momentum, and not the bugged one, has been used. This correspond to the fact that in real data on each found candidate the momentum given by the new prediction ha been employed to calculate the Pt. The results obtained by means of this procedure are reported in table A.1

In conclusion the bugs consequences were

1. To reduce the number of usable located events according to

$$N_{loc}^{corrected} = N_{loc} \cdot \epsilon_{red} \tag{A.1}$$

2. To decrease the scanning efficiency

$$A_a^{0\mu} = A_a^{0\mu} \cdot \epsilon(A_a^{0\mu}) \tag{A.2}$$

$$\eta_a^{0\mu} = \eta_a^{0\mu} \cdot \epsilon(\eta_a^{0\mu}) \tag{A.3}$$

	95	96
ϵ_{red}	0.585 ± 0.004	0.861 ± 0.002
$\epsilon(A_{NC})$	0.589 ± 0.006	0.857 ± 0.004
$\epsilon(A_{CC}^{0\mu})$	0.465 ± 0.011	0.968 ± 0.004
$\epsilon(A_{\tau^- \to \mathrm{h}^-(n\pi^0)\nu_\tau})$	0.451 ± 0.004	0.828 ± 0.003
$\epsilon(\eta_{\tau^- \to \mathrm{h}^-(n\pi^0)\nu_\tau})$	0.883 ± 0.004	0.901 ± 0.003
$\epsilon(A_{\tau^- \to e^- \nu_\tau \bar{\nu}_e})$	0.430 ± 0.007	0.821 ± 0.005
$\epsilon(\eta_{\tau^- \to e^- \nu_\tau \bar{\nu}_e})$	0.846 ± 0.006	0.960 ± 0.005
$\epsilon(A^{0\mu}_{\tau^- \to \mu^- \nu_\tau \bar{\nu}_\mu})$	0.434 ± 0.009	0.835 ± 0.007
$\epsilon(\eta^{0\mu}_{\tau^- \to \mu^- \nu_\tau \bar{\nu}_\mu})$	0.660 ± 0.009	0.893 ± 0.009

Table A.1: Correction factors for the 95 and 96 bug in the predictions

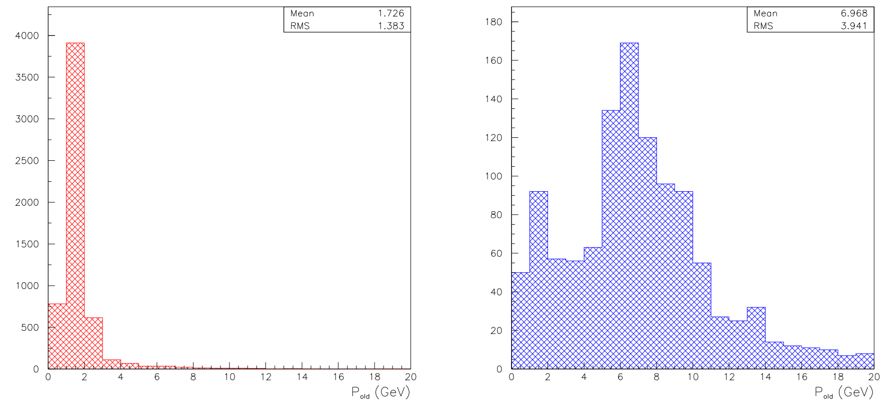

Figure A.3: "95 bugged" momentum distribution for new momentum in the bin of 1-2 GeV and 8-10 GeV

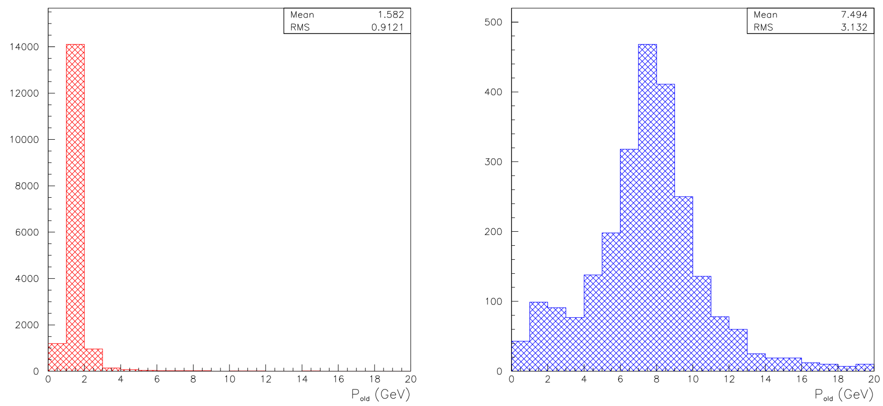

Figure A.4: "96 bugged" momentum distribution for new momentum in the bin of 1-2 GeV and 8-10 GeV

Conclusion

After many year from the Pontecorvo hypothesis of neutrino oscillations and after more than 30 years from the first experimental hints in favour of it, the question "do neutrinos oscillate" is still open. Therefore the search for evidence of neutrino oscillation is still a challenging subject of study for particle physicists.

One of the experiments nowadays searching for neutrino oscillation evidence is CHORUS. It searches for $\nu_\mu \to \nu_\tau$ oscillation in the appearance mode with the aim to reach high sensitivity in the mixing angle for large values of the neutrino mass difference. The CHORUS data taking is finished and the analysis of its data has been the subject of this thesis.

In particular I dealt with the evaluation of the analysis efficiencies developing a Monte Carlo simulation of all the analysis steps. As much as possible the main sources of systematic error introduced in the efficiencies evaluation by disagreement between simulation and real data have been checked and corrected for.

I estimated all the main background sources. This work includes also a simulation of the emulsion sensitivity in order to evaluate the contribution of the main background for the oscillation search using the τ hadronic decay mode.

Since it turns out that the background level was not negligible compared to the very small signal we were searching for, a study of its reduction has been carried on in order to optimize the sensitivity of the oscillation search. As a result of this study the background level in the 1μ data sample, the main set for the oscillation search, has been reduced by about a factor four with a negligible loss of the signal. Also the background rate in the other sample, the 0μ sample, has been reduced by about a factor three with an increase of the signal to noise ratio.

The conclusion of the analysis is that, since no oscillation candidate events have been found, an upper limit on the $\nu_\mu \to \nu_\tau$ oscillation probability has been derived. It results that $\mathrm{P}(\nu_\mu \to \nu_\tau) \leq 3.6 \cdot 10^{-4}$ at 90% of confidence level

Bibliography

[1] Pevsner and Kim, *Neutrino in physics and astrophysics*, Harwood academic publishers, 1993.

[2] R. Mohapatra and P. B. Pal, *Massive neutrinos in physics and astrophysics*, World Scientific, 1991.

[3] E. K. Akhmedov, Neutrino physics, hep-ph/0001264, 2000.

[4] C. G. S. M. Bilenky and W. Grimus, Progress in Partcicle and Nuclear Physics **43**, 1 (1999).

[5] Particle Data Group, D. E. Groom et al., The European Physical Journal C **15**, 1 (2000).

[6] DONUT Collaboraton, talk given at ICHEP2000, 2000.

[7] M. S. Turner and J. A. Tyson, Review Modern Physics **71**, 145 (1999).

[8] D. O. Caldwell, Neutrino dark matter, hep-ph/9902219, 1999.

[9] J. Bahcall, 2000, http://www.sns.ias.edu/ jnb/.

[10] K2K Collaboraton, talk given at Neutrino2000, 2000.

[11] A. Smirnov, Reconstructing neutrino mass spectrum, hep-ph/9901208, 1998.

[12] H. Harari, Physics Letters B **216**, 413 (1989).

[13] CHORUS Collaboration, Nuclear Instruments and Methods in Physics Research A **401**, 4 (1997).

[14] R. Oldeman, *Measurement of the differential cross-sections and structures funztions in neutrino and anti-neutrino on lead*, PhD thesis, University of Amsterdam, 2000.

[15] M. de Jong et al., CERN-PPE/93-131, 1993.

[16] S. Aoki et al., Nuclear Instruments and Methods in Physics Research B **51**, 446 (1990).

[17] E531 Collaboration, Physics Letters B **266**, 375 (1988).

[18] S. Ricciardi, *Ricerca delle interazioni quasi-elastiche di ν_τ nell'esperimento CHORUS*, PhD thesis, University of Ferrara, 1996.

[19] G. Ingelman et al., Lepto 6.5, DESY 96-057, 1996.

[20] Application Software Group, Geant detector description and tools, CERN program library long writeups Q123, versione 3.21, 1993.

[21] O. Sato, Private commuinication.

[22] S. Sorrentino, Gbeam the neutrino beam similator, 1998, CHOURS internal note 98005.

[23] J. M. Conrad et al., Review Modern Physics **70**, 1341 (1999).

[24] S. Ricciardi, Event generator for quasi-elastics and production of resonances, 1997, CHOURS internal note 97001.

[25] P. Righini, *Decadimento $\tau^- \to 3\pi\nu_\tau$ per la ricerca delle oscillazioni $\nu_\mu \to \nu_\tau$ in CHORUS*, PhD thesis, Universitá degli studi di Cagliari, 1999.

[26] M. V. Donckt, *Contribution to the $\nu_\mu \to \nu_\tau$ oscillation search in the CHORUS experiment*, PhD thesis, Université Libre de Bruxelles, 1999.

[27] B. V. de Vyver and P. Zucchelli, Cern Internal note CERN-PPE/96-113, 1996.

[28] E. T. Bolton, NEVIS R1501, 1994.

[29] A. Alton et al., Observation of neutral current chram production in ν_μ fe scattering at the tevatron, hep-ex/0009007, 2000.

[30] G. Marchesini et al., Computer Phys. Commun **67**, 465 (1992).

[31] P. Migliozzi et al., A search for z' in muon neutrino associated charm production, CERN-EP/2000-117, 2000.

[32] J. R. A. Fassò, A. Ferrari and P. Sala, New developments in fluka modelling of hadronic and em interactions, in *Proc. 3rd Workshop on Simulating Accelerator Radiation Environments (SARE 3)*, Ed. H. Hirayama, 1997.

[33] J. R. A. Fassò, A. Ferrari and P. Sala, Fluka applications in high energy problems: from lhc to icarus and atmospheric showers, in *Proc. 3rd Workshop on Simulating Accelerator Radiation Environments (SARE 3)*, Ed. H. Hirayama, 1997.

[34] J. R. A. Fassò, A. Ferrari and P. Sala, An update about fluka, in *Proc. 2nd Workshop on Simulating Accelerator Radiation Environments (SARE 2)*, Ed. G.R.Stevenson, 1997.

[35] J. R. A. Ferrari, P.R. Sala and S. Roesler, Zeitschrift für Physik C **70**, 413 (1996).

[36] W. H. Barkas, *Nuclear research emulsions*, Accademic Press, 1963.

[37] Fermilab p803 proposal, 1993.

[38] R. Santacesaria, Private commuinication.

[39] E. Eskut et al., Physics Letters B **434**, 205 (1998).

[40] CHARM coll., J.V. Allaby et al., Zeitschrift für Physik C **36**, 661 (1987).

[41] CDHS coll., A. Blondel et al., Zeitschrift für Physik C **45**, 361 (1990).

[42] CCFR coll., G.C. Arroyo et al., Physical Review Letters **72**, 3452 (1994).

[43] E. Eskut et al., Physics Letters B **424**, 202 (1998).

[44] G.Rosa et al., Nuclear Instruments and Methods in Physics Research A **401**, 7 (1997).

[45] T. Junk, Nuclear Instruments and Methods in Physics Research A **434**, 435 (1999).

Acknowledgements

Many people supported me during my PhD thesis work. In particular I am very grateful to my two advisors, Professor Ubaldo Dore and Doctor Roberta Santacesaria for many useful discussions and advices about all the problems that I have encountered during my job.

Many thanks are also for all the CHORUS collaboration. In particular I would especially thank Lucio Ludovici and Piero Zucchelli for their suggestions and help about some problems I came across during my analysis. I would thank also Doctor Osamu Sato for his patience in explaining me many details of the emulsion scanning.

I am also grateful to Doctor Alfredo Ferrari who gave me the Fluka code and some suggestions about how to use it.

Of course many thanks go also to my family and friends who tolerated the very few attentions and time I have dedicated to them during this period.